POLITECNICO
MILANO 1863

SCUOLA DI INGEGNERIA INDUSTRIALE
E DELL'INFORMAZIONE

Functional properties of $K_{0.5}Na_{0.5}NbO_3$ based devices fabricated by Pulsed Laser Deposition and Rapid Thermal Processing

Tesi di Laurea Magistrale in
Physics Engineering - Ingegneria Fisica

Author: **Andrea Rovelli**

Student ID: 942370
Advisor: Prof. Riccardo Bertacco
Co-advisors: Miguel Ángel Badillo Ávila, Chiara Groppi
Academic Year: 2021-22

Abstract

This thesis work was carried out at PoliFAB, the micro and nanotechnology center of the Politecnico di Milano with the help and support of STMicroelectronics. This joint research project was aimed at the study and improvement at the functional properties of potassium sodium niobate ($K_{0.5}Na_{0.5}NbO_3$), which is a lead-free piezolectric material that is promising, in terms of performances, to substitute the more popular lead-based functional materials used today, as lead titanate zirconate (PZT). The European Community is aiming to eliminate toxic elements, such as lead, from electronic devices by the end of 2025; the research and the study of those lead-free materials is thus crucial. The development of a stable and repeatable process to use those materials is mandatory to be able to meet the next safety standards. In addition, as the absence of harmful elements for the human body make them interesting for bio-applications. However, one major issue of KNN films with respect to PZT is its tendency to not be able to exploit the piezoelectric effect effectively due to a non-negligible current leakage which is promoted by the loss of alkaline elements during the deposition process and by oxygen vacancies in the film. In this work, KNN thin films were grown by the Pulsed Laser Deposition (PLD) technique on Pt(111)/TiO_2/SiO_2/Si substrates. The crystal orientation, morphology, stoichiometry, and other properties of the films were characterized. In addition, to test for the piezoelectric performance of the KNN films, a cantilever design was modelled and simulated using a finite element analysis software (FEA). This cantilever structure was at the end realized and characterized but due to the leakage issues the piezoelectric performances were poor. A particular attention was also directed to the electrical conduction mechanism in the obtained Metal-Insulator-Metal (MIM) stacks; in detail the impact on the current leakage of different metals used as top contacts was evaluated and the found rectifying behavior was associated with oxygen vacancies at the metal-KNN interface. This Schottky diode was in the end demonstrated. Finally, with the aim of reducing alkaline and oxygen vacancies to decrease leakage currents, Rapid Thermal Processing (RTA) of KNN was studied with overall good results on stoichiometry conservation.

Keywords: $K_{0.5}Na_{0.5}NbO_3$, lead free piezoelectric, leakage mechanisms, piezoelectric films, rapid thermal crystallization

Abstract in lingua italiana

Questo lavoro di tesi è stato svolto presso PoliFAB, il centro di micro e nanotecnologie del Politecnico di Milano con l'aiuto e il supporto di STMicroelectronics. Questo progetto di ricerca è stato finalizzato allo studio e al miglioramento delle proprietà funzionali del niobato di potassio e sodio ($K_{0.5}Na_{0.5}NbO_3$), che è un materiale piezoelettrico senza piombo che potrebbe sostituire in termini di prestazioni, i più diffusi materiali piezoelettrici a base di piombo oggi utilizzati, come per esempio il titanato di piombo zirconato (PZT). La Comunità Europea punta a eliminare gli elementi tossici, come il piombo, dai dispositivi elettronici entro la fine del 2025; la ricerca e lo studio di questi materiali "lead-free" è quindi cruciale. Lo sviluppo di un processo stabile e ripetibile per utilizzare questi materiali è obbligatorio per poter soddisfare i prossimi standard di sicurezza. Inoltre, l'assenza di elementi nocivi per l'organismo umano li rende interessanti per le bioapplicazioni. Tuttavia, uno dei principali problemi del KNN rispetto al PZT è la sua tendenza a non essere in grado di sfruttare efficacemente l'effetto piezoelettrico a causa di una dispersione di corrente non trascurabile che è promossa dalla perdita di elementi alcalini durante il processo di deposizione e dalle vacanze di ossigeno nel film. In questo lavoro, film sottili di KNN sono stati cresciuti mediante la tecnica Pulsed Laser Deposition (PLD) su substrati $Pt(111)/TiO_2/SiO_2/Si$. Sono stati caratterizzati l'orientamento cristallino, la morfologia, la stechiometria e altre proprietà dei film ottenuti. Inoltre, tramite un software simulativo a elementi finiti è stato modellato un "cantilever" per testare le prestazioni piezoelettriche dei film KNN. Questa struttura è stata infine realizzata e caratterizzata ma a causa dei problemi di dispersione di corrente le prestazioni piezoelettriche sono risultate scarse. Una particolare attenzione è stata poi rivolta anche al meccanismo di conduzione elettrica negli stack Metallo-Isolante-Metallo (MIM) ottenuti; in dettaglio è stato valutato l'impatto sulla dispersione di corrente di diversi metalli utilizzati come contatti elettrici superiori e il comportamento rettificante trovato è stato associato alle vacanze di ossigeno all'interfaccia metallo-KNN. Questo comportamento è stato collegato con la presenta di un diodo di tipo Schottky. Infine, con l'obiettivo di ridurre le vacanze alcaline e di ossigeno, per ridurre le perdite di corrente, è stato utilizzato un diverso tipo di trattamento termico; in particolare un Rapid Thermal Processing (RTA). Questo processo ha portato

a buoni risultati sulla conservazione della stechiometria ideale del film.

Parole chiave: $K_{0.5}Na_{0.5}NbO_3$, piezoelettrici senza piombo, film piezoelettrici, dispersione di corrente, annealing termico rapido

Contents

Abstract **i**

Abstract in lingua italiana **iii**

Contents **v**

1 Introduction **1**
1.1 Piezoelectric materials . . . 1
1.2 Applications . . . 2
1.3 State of the art and materials . . . 3
1.3.1 Lead free piezoelectric materials . . . 4
1.4 Choice of the experimental setup . . . 5

2 Experimental Techniques **7**
2.1 Pulsed Laser Deposition - PLD . . . 7
2.1.1 Nominal condition process in detail . . . 11
2.2 Rapid Thermal Annealing - RTA . . . 11
2.2.1 RTA process in detail and main differences between the classic deposition . . . 11
2.3 Morphological characterization . . . 12
2.3.1 Scanning Electron Microscope (SEM) . . . 12
2.3.2 Energy-Dispersive X-ray Spectroscopy (EDX) . . . 13
2.3.3 X-Ray Diffraction (XRD) . . . 16
2.4 Leakage characterization . . . 17
2.4.1 Pad deposition . . . 17
2.4.2 Two-points probing . . . 22
2.4.3 Conductive Atomic Force Microscopy (C-AFM) . . . 22
2.5 Optical lithography . . . 25

3 Piezoelectric cantilevers at PoliFab 27
3.1 Process layout . . . 28
3.1.1 Cantilever fabrication process . . . 29
3.2 Results . . . 31
3.2.1 Morphology . . . 31
3.2.2 Current leakage . . . 31
3.2.3 Simulations . . . 36
3.2.4 Measurements from STM . . . 38
3.2.5 Conclusion and future directions . . . 40

4 Asymmetric leakage in KNN capacitors grown by PLD 43
4.1 Overview of characteristics of films . . . 43
4.1.1 Crystallographic orientation . . . 43
4.1.2 Morphology . . . 44
4.1.3 Film stoichiometry . . . 46
4.2 Measurements variability . . . 47
4.2.1 Influence of top-electrodes on leaking current . . . 50
4.2.2 Potential barrier at the bottom pad . . . 51
4.3 Conclusions and suggestions for improvement . . . 63

5 Rapid Thermal Annealing 65
5.1 Preliminary results . . . 66
5.1.1 Crystallographic orientation . . . 66
5.1.2 Morphology . . . 70
5.1.3 Film stoichiometry . . . 71
5.1.4 Electrical characterization . . . 72
5.1.5 Preliminary conclusions . . . 73
5.2 Effect of annealing temperature . . . 74
5.2.1 Crystallographic orientation . . . 75
5.2.2 Morphology . . . 76
5.2.3 Film stoichiometry . . . 79
5.2.4 Electrical characterization . . . 80
5.2.5 Suggestions for the future . . . 82
5.3 Conclusions and future direction . . . 84

6 Overall conclusions 87

Bibliography **89**

List of Figures **103**

List of Tables **107**

1 | Introduction

1.1. Piezoelectric materials

Piezoelectric materials are a fundamental class of materials in the electronic field as their properties are able to exploit the energy conversion mechanism; in particular mechanical to electrical. In fact when subjected to mechanical vibrations or applied stress, induces the displaced ions in the material and results in a net electric charge due to the dipole moment of the unit cell. In detail the piezoelectric effect results from the linear electromechanical interaction between the mechanical and electrical states in crystalline materials that exhibit a non-inversion symmetry. When no pressure is applied on a crystal the centre of negative and positive charges coincide. The molecule is thus electrically neutral. But when a stress is present the molecule is distorted, displacing the charge centres, and this results in a small dipole inside the molecule. In order to be polarized by a stress the crystal structure must lack of inversion symmetry; if a crystal instead has a symmetry inversion the position of the charge center remains unaltered as every charge movement will be mirrored by an equal charge (fig. 1.1). The piezoelectric effect is a reversible process:

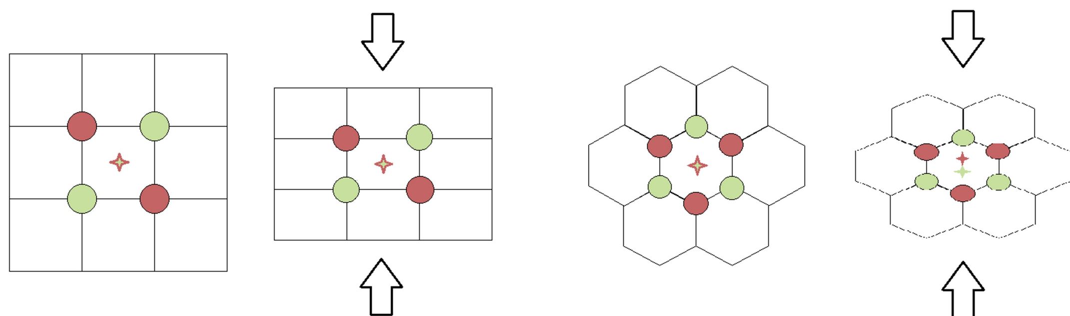

(a) A structure with inversion symmetry. With this symmetry property piezoelectricity cannot be exploited.

(b) A crystal structure that lacks of inversion symmetry. Under pressure a net polarization can be found.

Figure 1.1: Schematic representation of inversion-symmetric and non inversion-symmetric crystals (from [1]).

materials exhibiting the piezoelectric effect also exhibit the reverse piezoelectric effect, the internal generation of a mechanical strain resulting from an applied electrical field [2]. Piezoelectricy is often associated with ferroelectricy as in fact this is the property of a material to be able to show a piezoelectric effect even in abscence of an applied field (such as ferromagnetic materials have a net magnetic moment with no magnetic field applied). This can be seen in figure 1.2 where the pervoskite structure of a piezoelectric material in shown. However this property is lost when the Curie temperature (T_c) is reached and a phase transition between a ferroelectric state and a non polarized state is found. It is possible to take advantage of this phenomenon since the electric potential across the material can be collected. Piezoelectric materials are in fact often used as transductors in many different fields. Due to this key characteristics those type of materials have found interest in the engineering and industrial application fields.

1.2. Applications

Piezoelectric ceramics are found in a variety of products such as motors, sensors, actuators and transducers spanning from daily objects to the aerospace industry [4]. For example, the automobile industry is one of the mainly user of piezoelectric materials. Those are in fact employed in various aspects of products such as automotive-like tire pressure and monitoring systems, engine management system, vehicle stability/passenger safety system (seatbelts, airbag sensors), and more [5]. One example where a material

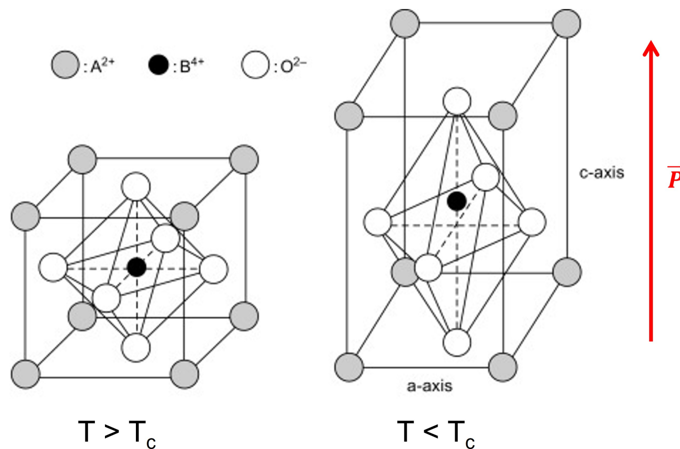

Figure 1.2: Perovskite structure of a ferroelectric material. If the temperature is below its critical value T_c the crystal is orthorombic and net polarization is present due to the slightly displacement of the atom in the middle of the structure. PZT and KNN also adopt this structure (from [3]).

with those characteristic is crucial is the diesel engine, where the precise control of a high pressure fluid can only be possible with a piezoelectric actuator [6]. Piezoelectric materials are also considered to be one valid approach to collect energy in a new sustainable way. The piezoelectric property can be used to harvest renewable energies such as ambient vibrations or acoustic waves [7]. In fact piezoelectric generators are able to convert mechanical energy given by the environment into useful electrical energy. In particular, vibration-based energy with frequencies in kHz range can reach an energy density up to milliwatts per cubic centimeter. Using this kind of ceramics to harvest energy can potentially transform the way we power/recharge electronic devices as no external power is required to do so. In particular, all the cited applications are not dependant on the size of the device, allowing for miniaturization if necessary and this can be the case for the so called Micro Electronical Mechanical Systems (MEMS) where the microscale is fundamental for the implementation in many integrated circuits. By downsizing the scale, is in fact possible to create complicate devices of micrometric size usually with moving parts, such as gyroscopes, energy harvesters, accelerometers, etc.. Piezoelectric materials are thus adaptable to be used in different designs, from fully suspended membranes to cantilevers, this allowing for a wide range of applications.

1.3. State of the art and materials

One of the most important advances in piezoelectric materials, from the point of view of their possible applications, is the acknowledgment of materials, that display a strong piezoelectric properties. This is the case of lead zirconate titanate (also known as PZT ($Pb(Zr_xTi_{1-x})O_3$)) solid solutions ceramics that back in 1954 were firstly characterized [8]. Since that moment, lead zircon titanate compounds were taken as a reference for further understanding and improvement of piezoelectric properties [9]. One way to characterize such materials is to study the so called longitudinal piezoelectric coefficient (d_{33}). This parameter represents the induced polarization in the same direction of an applied stress; the higher, the strongest the piezoelectric response. Due to its high piezoelectric coefficient value PZT has been leading the market of industrial applications and resources for decades. The applicability of lead zirconate titanate compound is also supported by its high critical temperature. Such temperature (also known as Curie temperature) is a specific temperature (particular for each material) over which the ferroelectric (and thus also the piezoelectric) properties of that material disappear [10]. The highest reported d_{33} value for PZT is 870 pC/N, with a critical temperature of 160°C [11]. Due to the superior properties of PZT no other materials have emerged in the past 20 years that are able to compete against it, considering not only its performances, but also in all the

industrial aspects such as stability of the processing and cost. PZT is in fact the most used piezoelectric material in the world. However, it has a major trade off; it is considered to be dangerous to human health and environment due to the high concentration of lead in the compound. This has created some concerns around it and extensive research has started to be carried out in order to find other piezoelectric materials capable to be comparable with PZT. This research has also been pushed by the European Union via different directives as explained in the next section.

1.3.1. Lead free piezoelectric materials

When the European Parliament imposed the RoHS (Restriction of Hazardous Substances) directive in 2002 (known as lead-free directive [12]), lead was included as a substance of which use had to be restricted. Due to this, research in the piezoelectric field has particularly grown interest on lead-free substitutes. Even though legislative restrictions by the European Union are aiming to eliminate toxic elements in electronic devices by 2025, research by companies still represent less than 1% of sales revenue of piezoelectrics; the main research in this field is mainly carried out by universities [13]. In our case a joint research partially sponsored and supported by STMicroelectronics [14] has been carried out. Although lead-free alternatives do exist, it is not easy to replace old and commonly used lead solutions with newer materials, especially if those lead-free materials are not able to provide better performances.

In the field of lead-free piezoelectric ceramics, potassium sodium niobate (KNN - $K_{0.5}Na_{0.5}NbO_3$) has emerged as a promising candidate to replace lead zirconate titanate. As PZT, KNN has the crystalline structure of perovskite that shows a orthorhombic phase at room temperature [15]. Many different studies have been performed on this material and one of the most outstanding d_{33} piezoelectric coefficients was found in 2004: $d_{33} > 400$ pm/V [16]. Thanks to such good results, KNN could be in principle a suitable material able to expand in the piezoceramic industry. Also, its Curie temperature (also known as critical temperature T_c) allow KNN to be used in many different fields (T_c can vary from 150°C to 400°C if suitable doped [17]). However, despite the remarkable progress made in the fabrication of KNN bulk ceramics over the past few decades, applications of KNN in thin film form are still in their early stages and currently represent a hot research topic. Several aspects of fabricating KNN films still need to be optimized, such as the precise control of stoichiometry, doping with appropriate elements and the formation of ternary compounds with other metal oxides. In addition, a full understanding of the conduction and loss mechanisms and the electrical response at different frequencies is still lacking.

Nevertheless, KNN is suitable for enabling applications in the field of green and biocompatible micro- and nano-electromechanical systems (MEMS and NEMS [18]). KNN and some other lead-free ferroelectrics and piezoelectrics show promise for small sensors, actuators, lab-on-a-chip electronics, and memory devices with high energy efficiency. If thin film deposition and device fabrication processes are made cost-effective and affordable for the industrial sector, KNN could be deployed on a large scale and partially replace lead zirconate titanate (PZT). Moreover KNN has better resistance to fatigue with respect to PZT [19]. Regarding full device fabrication, however, also other ancillary materials needed for efficient operation of KNN-based electronics are as important as the piezoelectric itself. In particular, the choice of suitable electrode materials is crucial as the bottom electrode material deeply influences the film texturation and morphology, while both top and bottom electrodes determine the leakage and linearity of the piezo-response [20].

1.4. Choice of the experimental setup

Pulsed Laser Deposition (PLD) was the chosen experimental techinque for this work to grow KNN ceramic films. However, different and comparable methods are already available and many different processes are suitable to be optimized and tuned. One example is the sputtering deposition which has a higher deposition rate for fundamental research. Using PLD it is possible to fine-tune the process to achieve demanded material properties. This is in fact has been done in previous works where small KNN samples were grown and characterized following an optimized process which was a result of wide studies of process' parameters and adjustments [20], [21]. However, even though the grown KNN samples show good crystallographic and stoichiometric properties, they tend to suffer from leakage. Leakage in KNN devices will be discussed in detail later in the present thesis. For KNN leakage has been related to two defects: the loss of alkali elements and the creation of oxygen vacancies. The first one is related to the high temperature reached during the various phases of the process while the latter has been associated to the creation of detrimental oxides between the KNN layers and the metals used for top and bottom electrodes. While the first can be in principle fixed by changing the deposition or the annealing temperature, the latter depends on more stages of processing. We have in fact chosen to perform a Rapid Thermal Annealing (RTA) only after the deposition in order to enhance the crystallization of the material and the loss of the alkali atoms as they are directly proportional to the process deposition and annealing temperature.

2 | Experimental Techniques

In this chapter the main experimental procedures and instrumentation are explained. KNN films were deposited onto Pt(111)(100 nm)/TiO_2/SiO_2(700 nm)/Si substrates by Pulsed Laser Deposition (PLD) technique. Substrates were provided by STMicroelectronics and they have also been used for previous process optimization [21], [20]. Different growth conditions have been able to produce different thicknesses, from the classic deposition for which the thickness is around 300nm to the RTA processed films where the thickness is circa 200nm. The work is mainly performed in an ISO-08 class cleanroom where many characterization procedures are performed ex-situ with the sample exposed to the controlled atmosphere of the cleanroom. The films' surface morphology and composition are examined using a Scanning Electron Microscope (SEM) and Energy-Dispersive X-ray spectroscopy (EDX), respectively. Then an electrical characterization of the sample is performed; contacts are deposited on the sample by an e-Beam evaporator or using sputtering, and two-point probe measurements are made.

2.1. Pulsed Laser Deposition - PLD

The Physical Vapour Deposition technology family (PVD) includes Pulsed Laser Deposition (PLD), which is conceptually and empirically very straightforward. This method uses a high-energy pulsed laser beam that is focused on a target of the material to be deposited in controlled environment (such as a vacuum chamber with the possibility to flow inside other gasses such as oxygen or nitrogen). A plasma plume made up of a mixture of electrons, ions, atoms, molecules, and other particles is created when the laser beam vaporizes a portion of the target material. The sample substrate is also placed in the chamber and is typically oriented parallel to the target. The plume rapidly grows in the chamber and deposits onto it. Target rotation and movement cause different areas on the target surface to be struck by the laser, which results in uniform target ablation (some setups use optical components to move the laser onto the target rather than moving the target and keeping the laser spot fixed). A picture of the uniform ablated target, the working principle and the plume created when the laser hits the target can be seen in

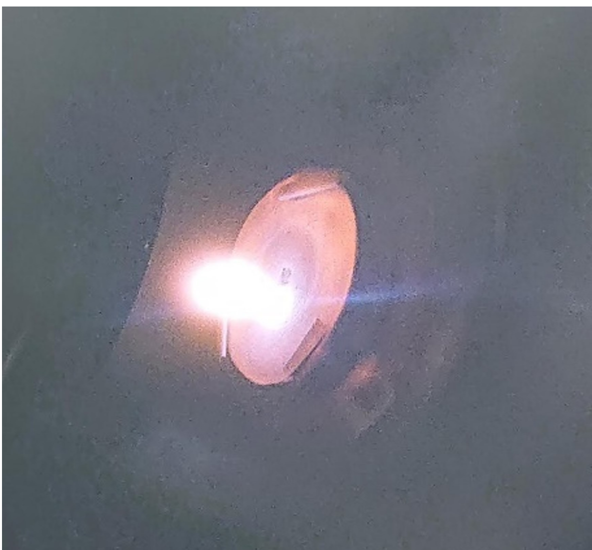

(a) Laser hitting the target and formation of the plume.

(b) Target after ablation.

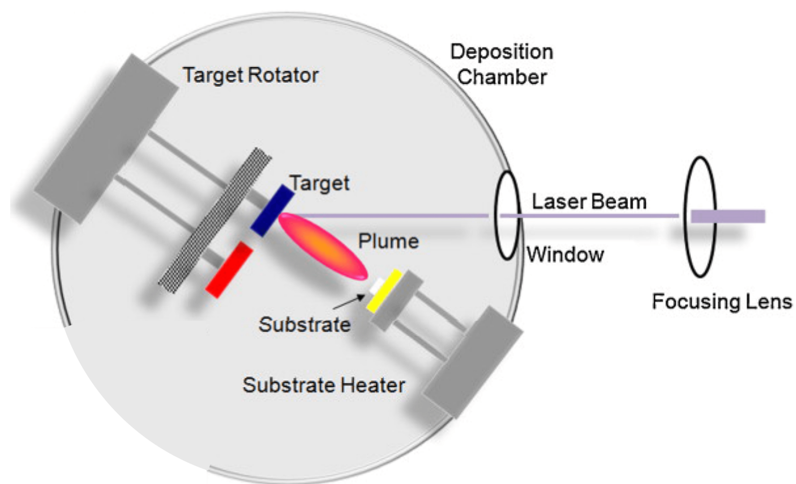

(c) Sputtering deposition schematic [22].

Figure 2.1: Target photos during the process and after the ablation and scheme of the working principle.

figure 2.1. To improve crystallization and deposition homogeneity, the sample can be heated (using a 400 W infrared lamp in an Al coated reflector placed in the back of the sample holder in our setup which can be temperature tunable increasing the current flow manually) and rotated continuously throughout the process. Additionally, the chamber can be filled with a background gas to enhance the composition of the deposited material. Both of the procedure are usually done in the process of deposition of KNN. Despite the conceptual simplicity of PLD, the laser-target interaction is quite complex and depends on numerous laser, environmental, and target material parameters. Material atomization is actually caused by a sum of thermal, chemical and mechanical energy contributions. The sputtering process itself is a mixture of collisional, thermal, electronic, exfoliation and hydrodynamic sputtering [23], [24]. Aside from its simplicity, PLD is also one of the most flexible deposition techniques, since with a proper setup almost any material can be grown by PLD. Everyday the list of materials that are able to be deposited using this technique is increasing. PLD also has some disadvantages, including the occurrence of the deposition of some particles and the specific careful tuning of the growth parameters for each material and situation that has arisen from the PLD versatility itself, which requires a long optimization of the process parameters for each specific material. The stoichiometry of the deposited film is fundamental to obtain suitable electrical performances of the ferroelectric. This problem is strongly related to ferroelectric materials since difficulties arise when the composition contains volatile elements such as Pb, Li or K. These elements may not adhere to the substrate or could re-evaporate from the film, resulting in a lack of volatile elements in the deposited film. The role of the laser in volatiles incorporation is secondary to the chamber gas environment, particularly the oxidizing background gas pressure. Substrate temperature plays an important role in crystallization orientation and can affect film composition in the presence of volatile elements. One strategy that can be used to achieve the desired stoichiometry is to add an excess of volatile elements to the target. This approach, although empirical, since the interaction of the ablated material and the gaseous environment is not yet understood, can easily lead to large compositional improvements [25]. The scheme of the whole The LASSE (Layered Artificial Structures for Spin Electronics) where the PLD deposition technique is included can be seen in figure 2.2. The exciting source employed for PLD is a Continuum Powerlite Precision II 8000 quadrupled Q-Switched Nd:YAG class-4 laser with fourth-harmonic-generated wavelength of 266 nm [26]. The used target for the deposition of both classic PLD growth and RTA processed films is a stoichiometric $K_{0.5}Na_{0.5}NbO_3$ ceramic target. The temperature of the sample could been read anytime using a pyrometer tuned to the emittivity of the platinum (≈ 0.30 [27]).

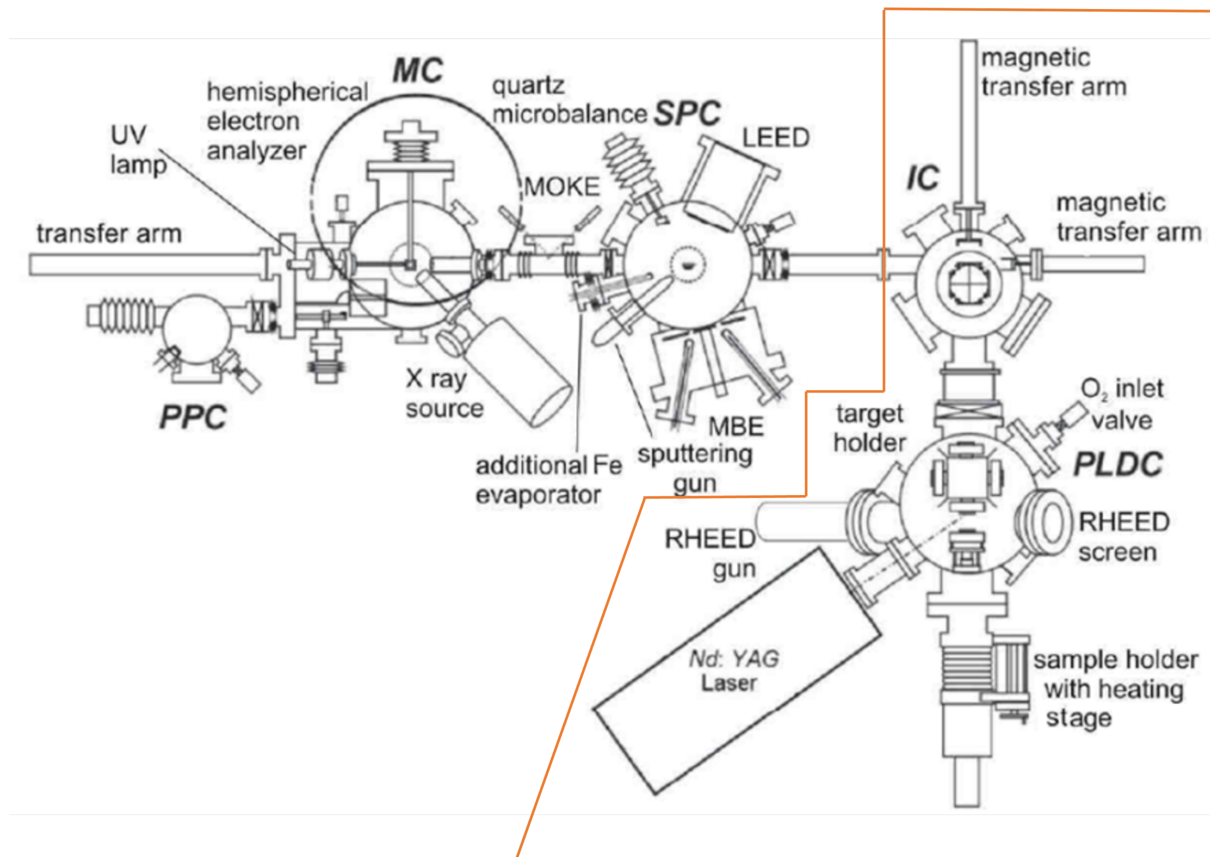

Figure 2.2: LASSE scheme. The red perimeter highlight the PLD experimental apparatus used to deposit KNN.

2.1.1. Nominal condition process in detail

To remove possible organic residuals of the coating protective layer of the wafer, an ex situ plasma cleaning for 10 min in oxygen plasma is performed before the process to the substrates. Then the substrate is placed inside the PLDC (fig. 2.2) and in order to promote Platinum surface reconstruction and to remove particles deposited onto the surface, a in situ vacuum annealing is performed at a temperature of 650 °C circa for 90 minutes with a final pressure of 5×10^{-7} mbar. The fine tuning of the classic PLD deposition has been researched in past works [21], [20] and so the optimal parameters to have a KNN deposition with the right stoichiometry and a preferential crystalline orientation have been found to be a laser fluence of $\sim$ 100 mJ/cm^2 with a frequency of the laser pulse settled to 10 Hz. The target substrate distance is fixed at 35mm and the deposition temperature of the substrate is held at 615°C with a constant oxygen pressure of 220 mTorr. The deposition takes 110 minutes to grow a $\sim$ 300nm KNN film. Right after the deposition the sample was annealed in-situ at a temperature of 500 °C for 30 minutes with a 0.5 atm oxygen constant pressure to promote the crystallization of the films and reducing the possible oxygen vacancy; those vacancies seem to be responsible to strongly altering the electrical properties of the piezoelectric film [28]. After the oxygen annealing the sample is cooled till room temperature [20].

2.2. Rapid Thermal Annealing - RTA

To apply the Rapid Thermal Annealing procedure a UniTemp RTP-150-HV (fig. 2.3) furnace for rapid annealing processes [29] has been employed. The furnace can work both in high vacuum conditions (up to 10^{-6} mbar) and using various standard process gases (such as nitrogen and oxygen). Nitrogen is also used for cooling the substrate. The heating is made by 24 infrared lamps, for a total power of 21 kW. All the programs parameters such as pressure, final temperature, process duration, cooling time can be manually programmed.

2.2.1. RTA process in detail and main differences between the classic deposition

In this section are highlighted the main differences of the process studied in order to improve KNN films characteristics. In fact the main difference with respect to the classic PLD deposition is given by the fact that first all the KNN deposition is made at 400°C and secondly the oxygen annealing after the deposition is not performed at all. So after

Figure 2.3: UniTemp RTP-150-HV [30].

the KNN has been deposited, the sample is let cool down till room temperature, after that it is moved to the RTA furnace and here a rapid thermal annealing is performed in normal atmosphere condition. Usually a ramp of 20°C/s is used to reach the annealing temperature and then the temperature is held for an arbitrary amount of time. At the time being it was not possible to anneal in pure oxygen atmosphere as the line of the oxygen was not yet present.

2.3. Morphological characterization

After the KNN deposition, the first measurements performed are a qualitative morphological analysis of the sample surface and the crystalline orientation with SEM (Scanning Electron Microscope). This gives us an immediate, albeit qualitative, idea of the influence of the growth parameters (such as temperature or oxygen pressure) and on the resulting film. Stoichiometric properties are then mostly observed by a subsequent EDX measurement. From this we can get the approximate dependence of the composition on growth parameters, a crucial element to consider in order to understand the best growth conditions.

2.3.1. Scanning Electron Microscope (SEM)

Scanning electron microscopy is one of the fastest and easiest ways to image the morphology of materials. Because crystalline features can be on the order of tens of nanometers, optical microscopes are not suitable for these observations: at the diffraction limit, details

smaller than the probe wavelength cannot be observed. However, changing the probe from photons to electrons allows for higher resolution detection. In SEM, a beam of electrons is emitted from a field emission gun and then scanned across the entire characterization area, scanning the sample surface. Several different interactions of the material with the beam then take place, one or the other of which could be examined depending on the application. We used a Raith LEO 1525, a high-resolution field emission scanning electron microscope (FE-SEM). Using a GEMINI field emission column, the microscope can be operated at voltages from 0.5 kV to 20 kV with a spatial resolution of 1.5 nm at 20 kV and 3.5 nm at 1 kV. Measures are taken in a vacuum chamber at pressures of $1.5 \cdot 10^{-5}$ mbar to avoid any gas affecting the electron beam. In the electron gun, a tungsten filament is heated to 1800 °C, and then electrons are emitted thanks to an extractor at a potential of +75 kV. Electrons are accelerated through the gun through a modifiable aperture (default is 30 μm) by a potential difference of 10 kV. A cross-section of the SEM is showed in figure 2.4. Backscattered electrons (BSE) are collected at the in-lens detector and can be analyzed to obtain a black and white image of the scanned surface. Because BSEs usually have fairly high energies, stemming from elastic collisions with the sample atoms, it is easy for these electrons to reach the detector. Therefore, by increasing the voltage of the electron beam, different depths of the sample can be analyzed. An Everhardt-Thornley detector measures secondary electrons (SE) for simultaneous topographic imaging with subnanometric resolution. However, SE usually have lower energies, making it more difficult to reach the detector; they therefore provide surface-sensitive measurements. In this work, backscattered electrons are the main source of morphological characterization with SEM.

2.3.2. Energy-Dispersive X-ray Spectroscopy (EDX)

SEM provides useful morphological information, but nothing can be said about the chemical composition, which is particularly relevant considering that it is complicated to achieve a stoichiometric film by PLD growth. For this purpose, energy dispersive X-ray spectroscopy (EDX or EDS) is used. EDX can be used to measure surface element composition and element fractions. The Bruker Quantax EDS chemical microanalysis system for SEM is available in the same device as the SEM. Quantification is then possible through available fitting models and specific elements can be targeted [33]. This technique uses the X-rays emitted by the sample when they are excited in some way. Our system uses an electron beam that is focused on the sample and accelerated with a variable voltage of a few kV; The higher the acceleration voltage, the deeper the electrons penetrate into the film, so different sample depths can be achieved by changing the voltage. When an

(a) Raith LEO 1525 placed in the yellow room.

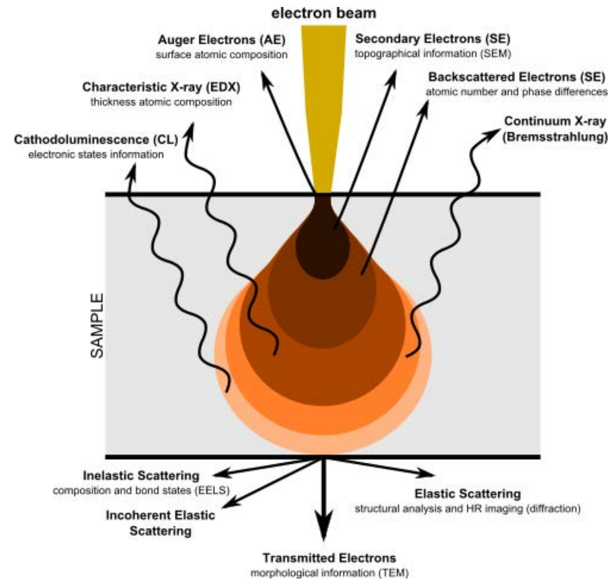

(b) SEM primary electron beam interaction with a specimen [31].

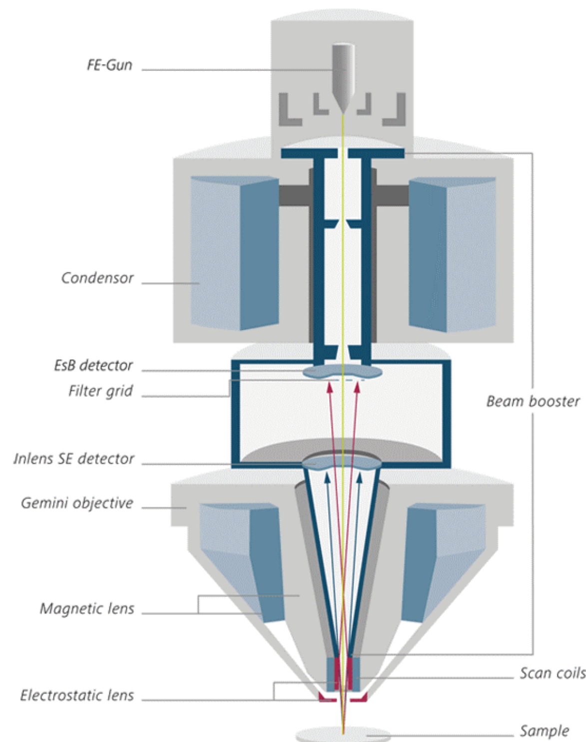

(c) SEM cross section [32].

Figure 2.4: Raith LEO 1525 in the yellow room and working principle of the SEM.

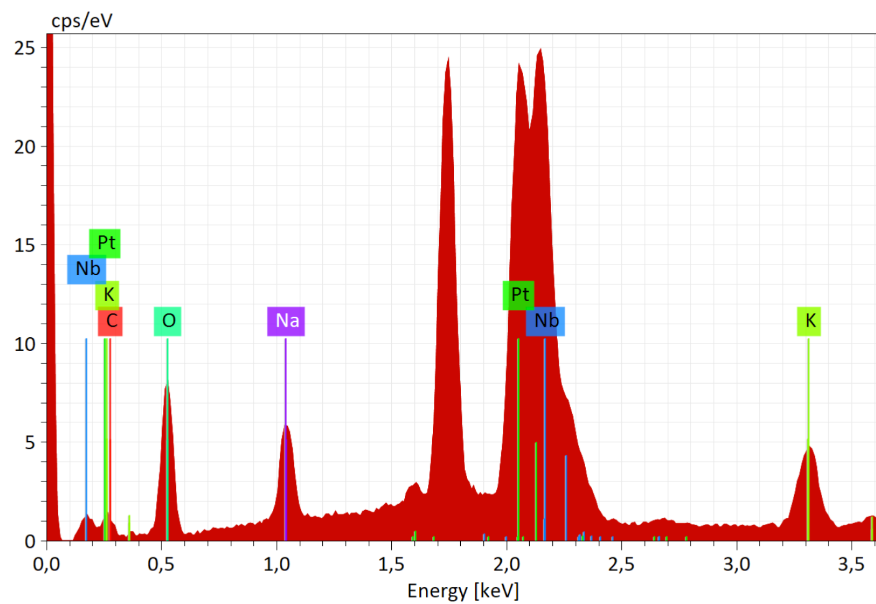

(a) EDX spectrum. Intensity peaks are associated to different elements as can be seen in the spectra.

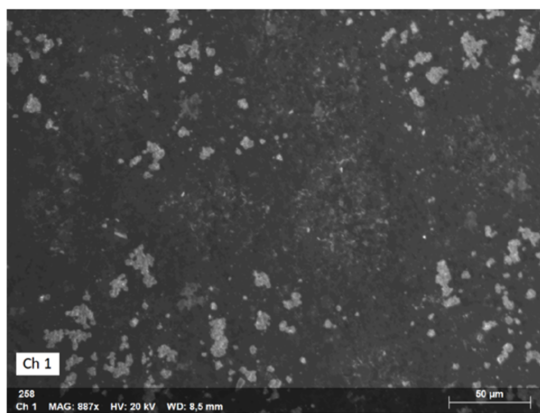

(b) SEM image of the selected area.

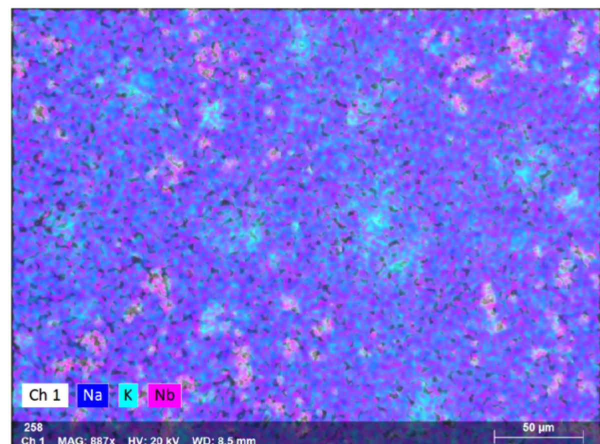

(c) EDX color coded of the selected area.

Figure 2.5: EDX spectra example and spatial information encoding.

electron of sufficient energy strikes a material atom, there is a likelihood that it will excite an electron from an internal energy level of the atom. A critical condition for this is that the beam electron energy is greater than the binding energy of the atomic electron (the former should be at least twice the latter for efficient excitations). That electron is then ejected from the shell, while an outer, higher-energy electron could take its place, decreasing in energy. The energy difference between the higher energy state and the lower energy final state of this electron is emitted as X-rays. The energies of atomic shells are sharply defined, as are the energy differences between two shells. The emitted X-ray photon is therefore characteristic of the atomic shells and thus of the type of atom itself; For this reason it is also known as the characteristic X-ray. These characteristic X-rays result in sharp peaks in the EDX spectrum. A second contribution to the spectrum is formed by the so called bremsstrahlung which comes from electrons that are slowing down due to interaction with the lattice. However, this radiation provides a frequency-continuous contribution to the spectrum and acts as a noise background that limits the resolution achievable with EDX [34]. An example of a signal acquired and fitted by the model is shown in figure 2.5; peaks intensity are directly proportional to their height. One useful thing that EDX provides is the fact that is it possible to use the signal obtained and mesh it with the image acquired by SEM to create a color coded map where the signal is directly proportional to the brightness of the color in that area. Not only it is possible to have a visual inspection of the film X-ray signal but also it is possible to filter the image for each element as can be seen in figure 2.5 where only nickel, niobium and potassium were chosen to be shown.

2.3.3. X-Ray Diffraction (XRD)

X-ray diffraction (XRD) is a common technique that can be used for a variety of purposes, including determining sample composition, strain measurement, and sample phase. In the present work, XRD is used to measure the lattice constant of the film structure and thus obtain the lattice orientation of the deposited film. X-rays are used because a wavelength similar to the distance between atoms in the sample is needed, otherwise longer wavelengths would not be affected by the crystal. The ray, which is incident at an angle θ (called a diffraction angle) with respect to the sample surface, is deflected upon hitting an atom at an angle 2θ with respect to the direction of the incident ray. Rays are diffracted by different atomic planes; at some diffraction angles the diffracted rays cancel each other out, at others constructive interference occurs. The diffraction angle at which constructive interference occurs can then be used to determine the difference between atomic planes using Bragg's law $2dsin\theta = n\lambda$, where λ is the beam wavelength,

θ is the diffraction angle, n is an integer, and d is the distance between atomic planes; see figure 2.6 for a brief scheme of the working principle. At these angles, a peak in intensity will be detected. Angles of these peaks can thus be used to obtain information about the atomic planes distance through Bragg's law equation, and distance can be used to determine composition or crystalline structure of the sample [35], [36]. Our measurements were performed at room temperature (θ–2θ scans) with a Rigaku SmartLab XE X-Ray Diffractometer [37]; the instrument exploits the characteristic X-ray radiation of a Copper anode (with a characteristic wavelength of $\lambda = 1.5406$ Å).

2.4. Leakage characterization

Morphological and compositional measurements of the sample can give preliminary indications of the quality of the deposited film while electrical characterization provides information about the electrical properties of the sample; in particular we are interested into probing the current leakage through the film. Electrical measurement results can vary depending on many factors, from electrode material [21] to temperature [40]. In order to apply a voltage to the film metal contacts must be deposited onto the ceramic, then with a two point probe current leakage is measured.

2.4.1. Pad deposition

To characterize the films in terms of current leakage, a matrix of square pads had to be deposited onto the growth KNN. Various technique has been exploited to deposit different metals; for nickel, titanium and chromium we have employed a metal evaporation while for platinum a metal sputtering has been used. However, in order to deposit the Platinum metal pads to probe the cantilevers, litography techinque has been exploited to deposit a mask onto the film to preserve the platinum in a well shaped pattern the was previously deposited using the standard sputtering methods. Ion Beam Etching technique has been used to create the nickel pads as in fact in order to have a pad onto the film, a first layer of nickel must be deposited and then, after the deposition of the titanium pads matrix, it has to be removed to avoid short circuits while probing for I-V curves. All the matrices of pads were deposited using a physical mask. The obtained pads have different thicknesses (that depends on the deposition rate or the technique used) with a section of 38x38 μm^2.

Metal sputtering

The sputtering system used to deposit platinum pads onto the KNN films is the AJA ATC Orion 8 manufactured by AJA International Inc. [41]. Magnetron sputtering is a

(a) X-Ray Diffractometer Rigaku SmartLab XE [38].

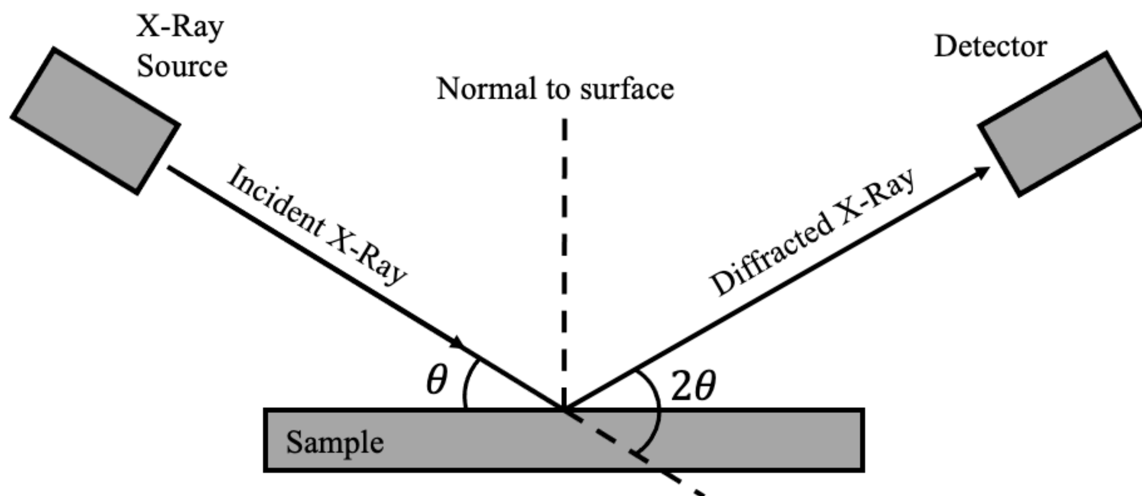

(b) XRD schematic setup and working principle [39].

Figure 2.6: X-Ray Diffractometer used and working principle.

physical vapor deposition technique, which allows a good film adhesion to the substrate, and a high control on the thickness, uniformity and composition of the deposited material. By first creating a gaseous plasma and then accelerating the ions from this plasma into some source material (i.e. the target), the source material is eroded by the arriving ions via energy transfer and is ejected in the form of neutral particles – either individual atoms, clusters of atoms or molecules. As these neutral particles are ejected, they will travel in a straight line unless they come into contact with something – other particles or a nearby surface. If a "substrate" such as a Si wafer is placed in the path of these ejected particles, it will be coated by a thin film of the source material. In order to create the plasma, atoms of an inert gas (frequently Ar) are introduced into the HV (High Vacuum) chamber and a negative bias voltage is applied to the target. Free electrons are immediately accelerated by the electron field in proximity to the target and ionize by collision the Ar atoms leaving Ar+ ions. This cascade process ignites the plasma. At this point, positively charged Ar+ ions are accelerated towards the negatively biased electrode, striking the surface and releasing source material and more free electrons by energy transfer. In magnetron sputtering, permanent magnets are located behind the target in order to confine the free electrons in a magnetic field directly above the target surface. This provides a double advantage: first, the free electrons, which are rejected by the negatively charged target, are prevented from bombarding the substrate, which would cause overheating and structural damage; second, the circuitous path carved by the free electrons along the lines of the magnetic field enhances the probability of ionizing neutral Ar atoms by several orders of magnitude. This increase in available ions significantly increases the rate at which target material is eroded and subsequently deposited onto the substrate. Due to the high cost of the platinum this technique was not exploited that much as in fact to deposit metals that has a certain cost, to optimize the process cost ratio, the deposition is done in batches of different sample all in one process phase.

Ion Beam Etching (IBE)

Sputtering and Ion Beam Etching System – Kenosistec VS80 manufactured by Kenosistec [43]. Ion Beam Etching is a physical dry etching technique where Ar+ ions are accelerated towards the sample in a vacuum chamber. Not dissimilarly to what happens with sputtering targets, the sample material is removed by energy transfer between the accelerated Ar atoms and the sample surface. Ar+ ions are generated from inert Ar gas through a discharge current. Here, a filament run by current, which is the cathode, emits electrons by thermoionic effect. These electrons, accelerated towards the anode by the voltage applied between the electrodes (discharge voltage), hit and ionize the Ar atoms giving rise

(a) AJA ATC Orion 8 [41].

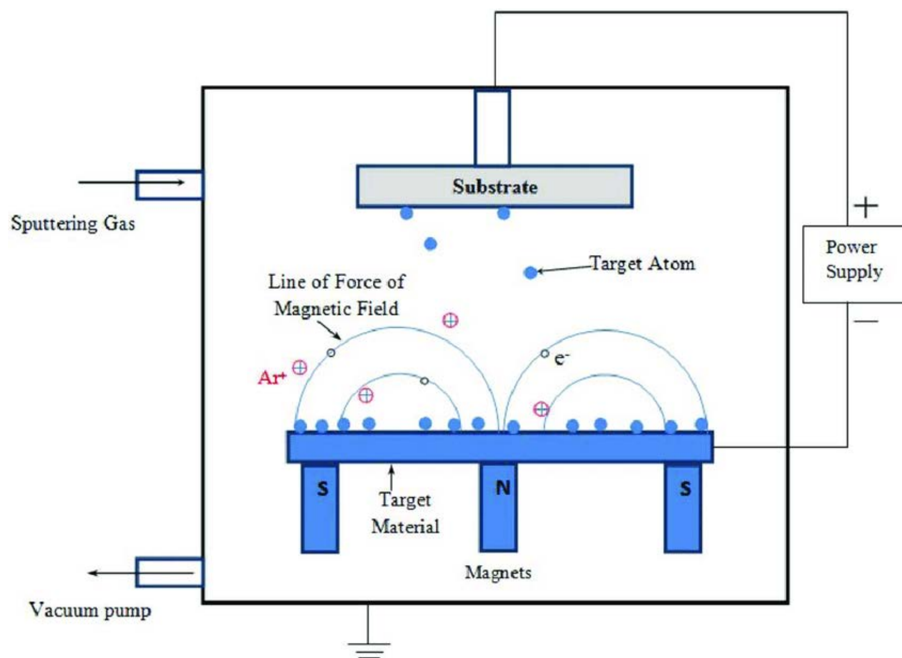

(b) Sputtering deposition schematic (from [42]).

Figure 2.7: AJA magnetron sputtering machine and schematic.

(a) Kenosistec VS80 [43]

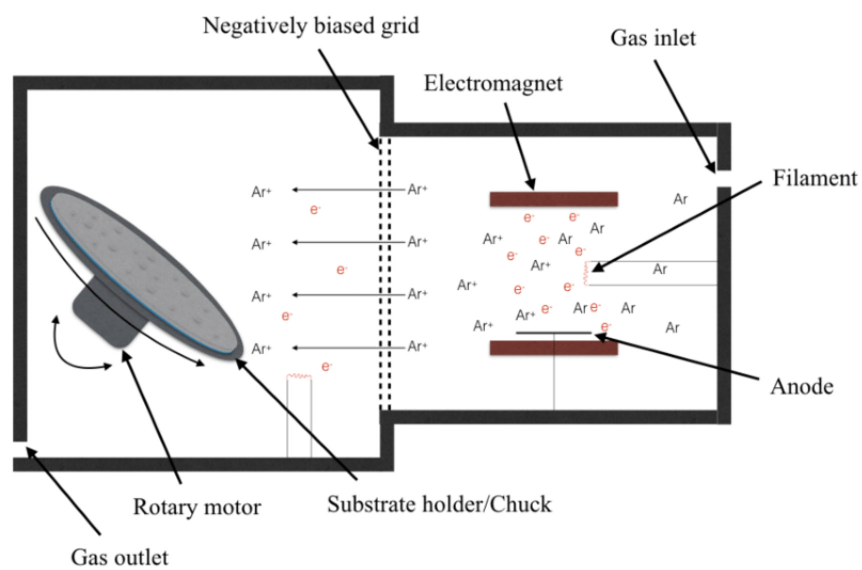

(b) IBE schematic [44].

Figure 2.8: Ion Beam Etching machine and schematic.

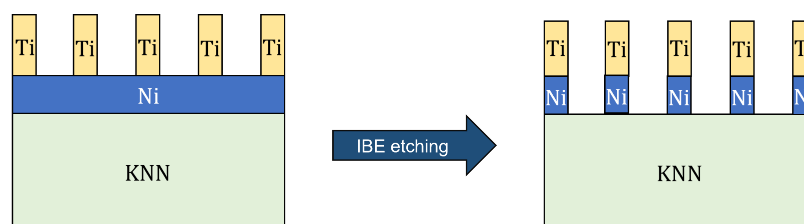

Figure 2.9: IBE schematic to remove the Ni layer after the Ti pads deposition.

to Ar+ ions and free electrons. These free electrons, which are also accelerated by the potential difference, contribute to maintain the plasma. Some of the Ar+ ions are then accelerated toward the sample by a grid set at a negative potential (accelerator voltage). IBE in particular has been used to create the Ni pads as the physical mask has been giving not good results in the previous deposition experiment; since what is important for the leakage characterization is the Metal-KNN interface we need firstly to deposit Ni to create such interface and then we need to remove it to avoid having a continuous metal layer that could have given us back a short circuit while measuring the I-V curve. After the Ni deposition a matrix of Ti must be deposited in order to create the actual contacts, after that Ni is etched via IBE. Etching rate in normal condition for Ni is 30 Å/min ($\sim$ 3nm/min) while for Ti is 30 Å/min [45] so the Ti on top was basically untouched after the process (usually 10-12 minutes of etching as the deposited Ni layer is 30nm); also no particular damage has been found on the KNN film. In figure 2.9 is possible to have a visual representation of this process.

2.4.2. Two-points probing

The measures are carried out ex-situ in a controlled atmosphere using a Manual Electric Probe System, the SÜSS MicroTec PM5 provided by SÜSS MicroTec AG [46], while voltage source used is the Keithley 2612 System SourceMeter provided by Keithley [47]. Despite the insulating properties of piezoelectric oxide films, leakage current is always measured. Because this current, however small, could affect the proper functioning of a device and the electrical properties of the film, measurements of this current must be made. Is it possible to measure the leaking current by sweeping the voltage with a positive triangular followed by a negative triangular voltage profile. For measuring current, there are two possible setups. While top-bottom measurements are performed between a bottom metal layer on which the thin film has been placed and a top electrode, top-top measurements are performed between two identical electrodes deposited on the thin film. Even though the top-bottom structure is inherently asymmetric, measurements made in this configuration should be symmetric. As a consequence, the reported capacitance is the same as that of a single thin film that is twice as thick as the actual film. In the case of the top-bottom configuration the tip touching the metal pad is always the one controlling the bias while the tip placed on the bottom electrode is kept at ground potential.

2.4.3. Conductive Atomic Force Microscopy (C-AFM)

Conductive atomic force microscopy (C-AFM) or current-sensitive atomic force microscopy (CS-AFM) is a mode in atomic force microscopy (AFM) that simultaneously measures

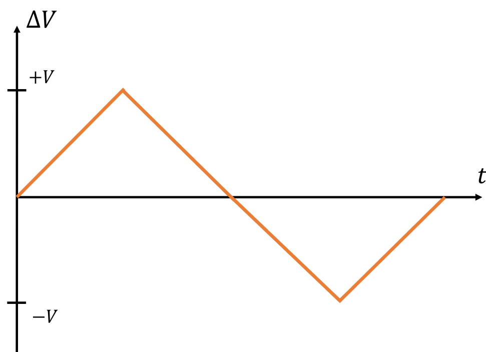

(a) Voltage signal used to measure the leakage.

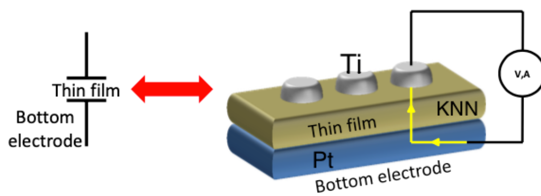

(b) Top-bottom configuration [48].

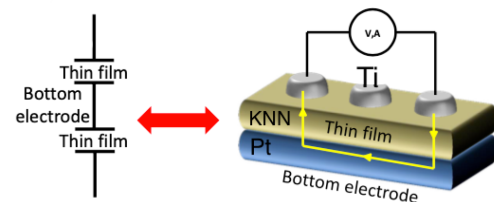

(c) Top-top configuration [48].

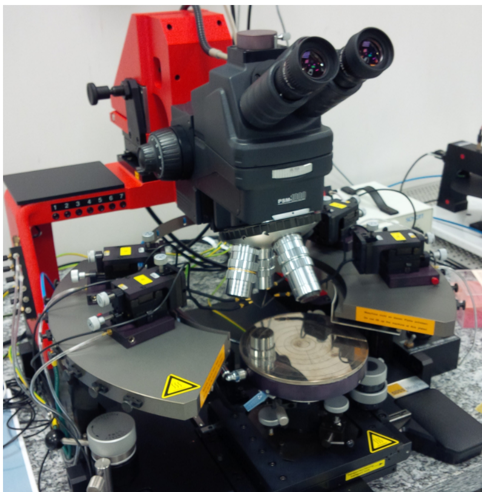

(d) SÜSS MicroTec PM5 [49].

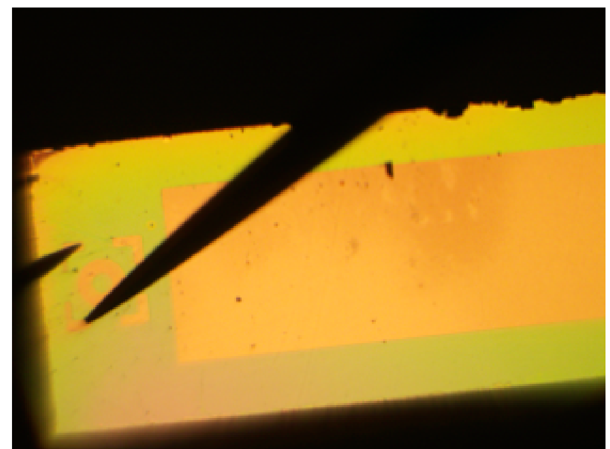

(e) Image of a top-top measurement on the cantilever top pads.

Figure 2.10

the topography of a material and the electric current flow at the point of contact of the tip with the sample surface. The topography is measured by detecting the deflection of the cantilever with an optical system (laser and photodiode) while the current is detected with a current-voltage preamplifier. The C-AFM is usually operated in contact mode; the tip can be kept at one location while the voltage and current signals are applied/read, or it can be moved to scan a specific region of the sample under a constant voltage (and the current is collected). In order to transform a simpler AFM into a C-AFM, three elements are needed: firstly the probe tip must be conductive, then a voltage source has to be present to apply a potential difference between the tip and the sample holder, and lastly a preamplifier is used to convert the (analogical) current signal into (digital) voltages that can be read by the computer. In C-AFM experiments, the sample is usually fixed on the sample holder using a conductive tape or paste, such as silver paint. Using this schematic, when a potential difference is imposed between tip and sample an electrical field is generated, which results in a net current flowing from tip-to-sample or vice versa [50]. For this work a NX10-AFM by Park System has been employed with a measurable current range of 10 $\mu A \sim 10\ nA$ [51]. In figure 2.11 is it possible to see the schematic of the instrument and the result of a measurement.

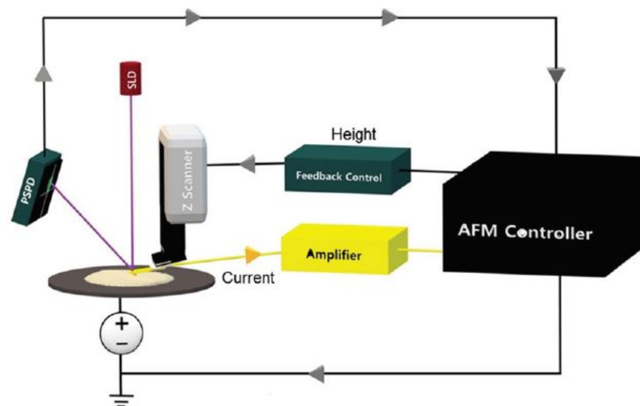

(a) Schematic of the working principle of C-AFM [52].

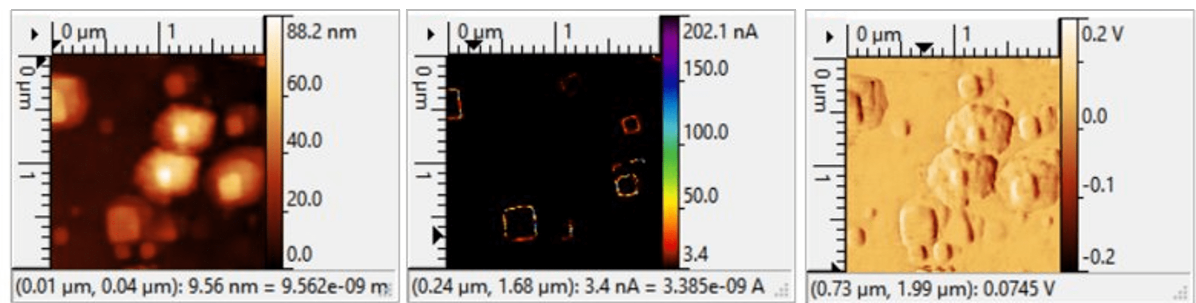

(b) Local current measurements map coded with topography. Those images are taken using the C-AFM techinque.

Figure 2.11: C-AFM schematic and a measure example.

(a) Maskless aligner Heidelberg-MLA100 [53]. This instrument is placed in the yellow room.

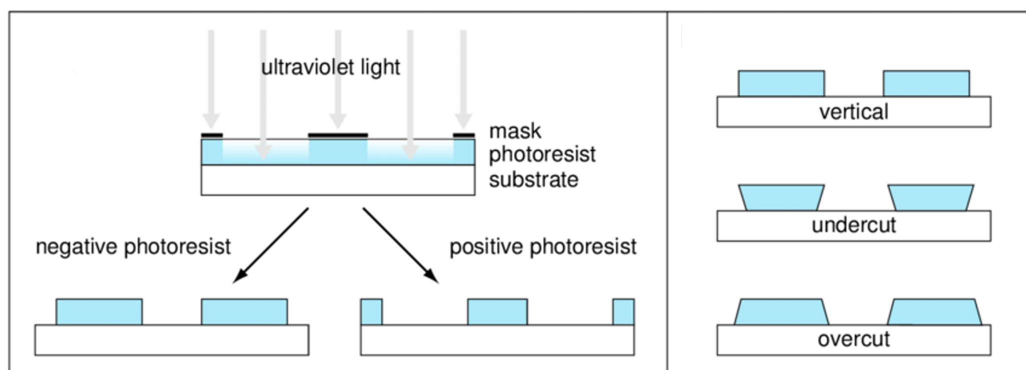

(b) Schematic of a positive and a negative resist with the possible outcomes for the profiles (from [54]).

Figure 2.12: Used instrumentation and visualization of the photolitographic process.

2.5. Optical lithography

Lithography is a process that uses focused energy, such as light or an electron beam, to imprint a sensible substance called resist. The resist is then developed to remove the areas that were or were not exposed to the focused energy: specific patterns are created in this step. These patterns can be temporary or used to add or remove material from a given area, for example by sputtering in the first case or by etching in the second case (dry or wet). Optical lithography uses light to imprint patterns on a light-sensitive substance called photoresist. Lithography is used to pattern specific designs and this can be exploited either with a physical mask (called photomask) or without it by simply operating with a mask design software and a light source. In the first case each design needs to be associated with a unique physical mask; therefore this method is not flexible as even the tiniest change in the design would require a new mask and this is usually an expensive process. Operating using a maskless approach is instead a more flexible process as the design of the mask can be changed every time by just changing it using a software;

to pattern the resist a focused light source (which is usually in the UV range) is required. A major drawback of maskless lithography is the time required to impress the resist since the scanning is raster and not in parallel like it is using a physical mask; this can lead to very long exposures. To pattern the cantilever pads a maskless lithography approach has been used. The instrument is a Heidelberg-MLA100 [55] which is a maskless aligner equipped with a high power LED source tuned at 365nm. This machine is able to write down to 1 μm with a maximum speed of 50 mm^2/min. The instrument is shown in figure 2.12a. In order to pattern a specific design, as already said, a photoresist must be used. Photoresists are organic compositions consisting in light sensitive polymers or polymer precursors which are dissolved in one or more organic parts [56]. A photoresist is usually made by three different components that can react differently in order to obtain the desired design. Those three components are: a photoactive part, which changes its structure when it is exposed, a matrix which is an inactive resin, and a casting solvent, which disappear after prebaking. A photoresist can be positive or negative. In positive resists, light causes chain scission, making it more soluble, so the exposed parts are removed by a developer, or negative, in case there is cross-linking of exposed parts, so that they become less soluble and are not removed by the developer. Photoresist in order to be able to create patterns are sensible only to precise light energy; in this work AZ5214E photoresist has been used [57] since it can be impressed by a wavelength of 365 nm, which is the one of the MLA. This resist can be either positive or negative if heated after exposure and the enlightened with UV light; this is mandatory to obtain the first exposed areas insoluble in the developer and make the areas which are not yet been exposed able to be developed [58]. The final resist profile is determined optical system used and the properties of the resist. In the case of positive resist the etch profile is usually overcut which means that the slope is positive (or vertical if necessary). Usually, this kind of resist is used for etching both dry and wet etching can be used to remove the resist; the vertical profile is ideal for reactive ion etching (RIE), while the overcut is often used for wet etching. In the case of negative development the result slope is negative, so there is an undercut, which is ideal for liftoff process that in this work has been exploited to remove the resist after the platinum sputtering. The detail process to obtain the cantilever is shown in section 3.1.1 while a brief schematic of the photolitographic process, with the possible outcome for the profiles, is shown in figure 2.12b.

3 | Piezoelectric cantilevers at PoliFab

Piezoelectric materials can be exploited in many different applications. In particular, in the field of MEMS (Micro Electronical Mechanical Systems) they are used in a series of layouts that can exploit the piezoelectricity of the material to achieve an electronic signal when facing a mechanical deformation. Piezoelectric materials are used as transducers in many different fields (as already cited in the introduction). Regarding MEMS they are currently used in different designs such as membrane and cantileveres as well for energy conversion, radiofrequency (RF) and biomedical applications [59], [60], [61], [62]. One of the simplest approach to exploit the piezoelectricity of a material is with a suspended structure. One of the most important parameter for a piezo in the sensing field is the conversion of its mechanical vibration into a electric signal. This can be done by analyzing the piezoelectric charge coefficients that describe the strain induced by an applied polarization.

The piezoelectric charge coefficient is expressed as a tridimensional tensor $\underline{\underline{d}}$ where the coefficients d_{ij} of the matrix describe the ratio between the strain applied to the j-axis and the electric field applied along the i-axis, or also as the ratio between the short circuit charge per unit area that flows in a direction perpendicular to j and the stress applied in the i direction. Indeed, the piezoelectric charge coefficients are expressed with dimensionality of $[\frac{pm}{V}]$. From the piezoelectric constitutive equation (eq.) are based on the assumption that the total strain in the transducer is the sum of mechanical strain induced by the mechanical stress and the controllable actuation strain caused by the applied electric voltage.

$$\varepsilon_i = S^E_{ij}\sigma_j + d_{mi}E_m \tag{3.1}$$

$$D_m = d_{mi}\sigma_i + \xi^{\sigma}_{ik}E_k \tag{3.2}$$

where σ $[\frac{pm}{V}]$ is the stress vector, ε $[\frac{m}{m}]$ is the strain vector, E $[\frac{V}{m}]$ is the vector of the applied electric field, ξ $[\frac{F}{m}]$ is the permitivity, d $[\frac{m}{V}]$ as already cited is the matrix of piezoelectric strain constants, S $[\frac{m^2}{N}]$ is the matrix of compliance coefficients stress vector,

and D $[\frac{C}{m^2}]$ is the vector of electric displacement. Is it possible to observe that a pure piezoelectric strain is obtained only if zero mechanical stress is applied ($\underline{\sigma} = 0$). This results is shown in equation 3.3 where $\underline{\epsilon}$ is the strain vector induced by the polarization effect and $\underline{E}$ is the applied electric field [63].

$$\underline{\epsilon} = \underline{\underline{d}}\, \underline{\mathrm{E}} \tag{3.3}$$

For a trampoline design the most important parameter is the longitudinal piezoelectric charge coefficient d_{33}, which describes the strain-induced polarization in the same direction (in particular in the out of plane direction) at which the strain is applied or otherwise can express the displacement upon an applied tension (converse piezoelectric effect). Another important coefficient for piezoelectric trampolines is the dielectric coefficient e_{ij} which determines the charge per unit area in the i-axis due to an electric field applied in the j-axis. In most piezoelectric materials a field applied along the j-axis causes electric displacement only in that direction [63]. For piezoelectric cantilevers usually the dielectric coefficient $e_{31,f}$ is measured.

3.1. Process layout

A first run of classic PLD processed KNN cantilevers has been delivered to be tested in PoliFab and later by STMicroelectrics to obtain other characteristics such as the response to the displacement in function of the frequency. In order to get possibly good results in

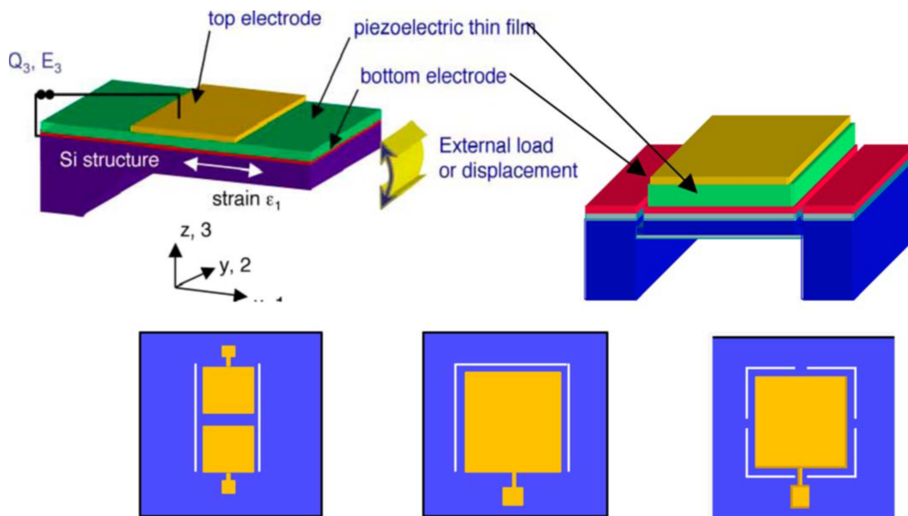

Figure 3.1: Laminated Piezoelectric/Si deflecting structures used in piezoelectric MEMS: bridge, cantilever and suspended membrane (from [59]).

terms of displacement and piezoelectric coefficients a fully suspended trampoline structure is required, however a convenient way to approach this result is to firstly operate with a full wafer thickness cantilever. In this way it is possible not only to extract electric characteristic but also to track the tip displacement of the structure as a function of the externally applied electric field. This geometry is particularly useful for two main reasons. First of all the sample preparation does not need advanced micromachining or etching steps, as just top electrode patterning with photolitography is required. Second is it possible to evaluate the in-plane stress analytically ($e_{31,f}$) if the sample geometry and the elastic properties of the substrate are known, and most importantly independently on the elastic properties of the film since it is much thinner than the substrate and the whole elastic properties are given by the silicon as it is much thicker [64]. Parameters for well known materials are widely available while for KNN is it possible to use dielectric characteristic found in other studies. A little insight on this is presented in section 3.2.3 where evaluation on the displacement are reported.

3.1.1. Cantilever fabrication process

In order to create the first cantilever prototypes, a classic PLD growth has taken place to obtain a 300 nm KNN film on the substrate. Then, its morphology has been characterized to check for major defects. After the film deposition, a plasma in oxygen atmosphere has been done to clean the film before putting the resist on. After spinning and baking at 110°C for 90s, the resist becomes a solid homogeneous film all over the substrate. The film is then exposed in the MLA (MaskLess Aligner) with a chosen mask (figure 3.2). This layout has been adopted since it shapes the top Pt pads for later current and displacement testings. After this, a second bake has taken place in order to obtain a reversal development. Finally the substrate is put under UV light and then developed. After the development the 50nm platinum layer to create the top metal contact has been sputtered using the AJA machine. The last step is to remove the unwanted platinum (lift-off). To do so a bath in acetone takes place. After this, another simple plasma cleaning is performed (descum). The reversal development (i.e. negative resist) has been exploited in order to obtain a profile for the resist with a negative slope; thanks to this the non wanted sputtered platinum can be detached from the surface in an efficient way. Also, the edges of the platinum pad are quasi vertical [65]. To obtain three cantilevers the sample patterned is diced into three sub-samples each one being a cantilever itself. A sketch of the obtained cantilever can be seen in figures 3.2b-c.

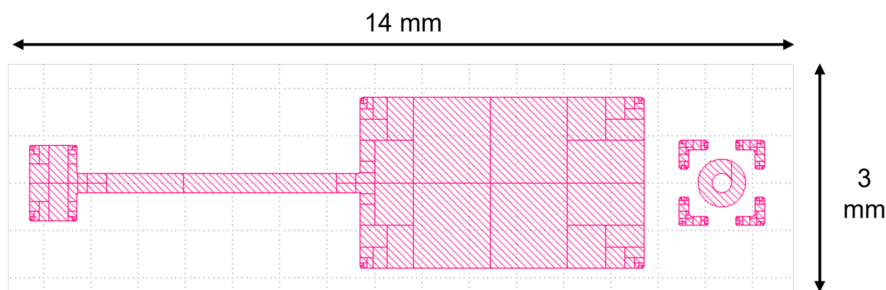

(a) Mask used to expose the resist in the MLA. This design is repeated three times in total on the shortest side to create three cantilevers.

(b) Sketch of the final layered structure.

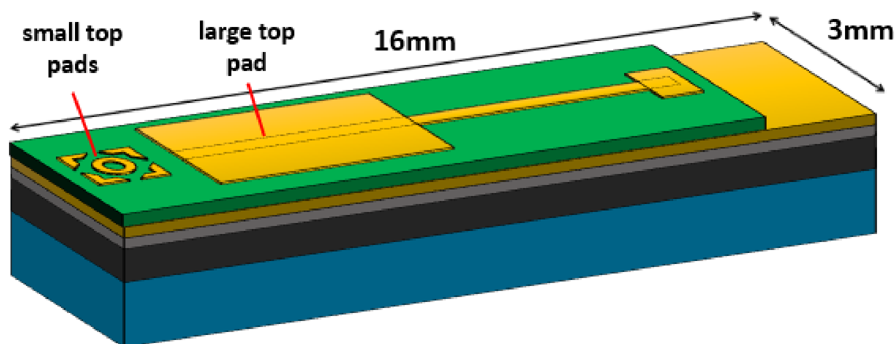

(c) Visualization of the obtained structure.

Figure 3.2: Mask used to pattern the platinum top electrodes and sketch of the obtained structure.

3.2. Results

In between the whole process, and after its completion, different measurements where performed on the sample to characterize it [20]. In principle, the KNN film obtained in this process has the same morphologic characteristic of the classic PLD sample presented in section 4.1. However, a brief characterization has been done anyway. After a visual inspection, current voltage measurements were performed to retrieve its behavior in terms of current leakage.

3.2.1. Morphology

The sample obtained after the PLD growth was briefly analyzed using a SEM with a energy of the beam of 10 kV. What is possible to observe from figure 3.3 is that no big defects are found to be present through the film but still crystallites of different orientation with respect to the preferred KNN(001) are arising from the surface. This can be also seen in figure 4.2 where the orientation of the crystallites is depicted. Unfortunately, during other measurements a cantilever has broke in half. This however has let us take a cross section of the whole structure confirming not only the thickness of the different layers but also the compactness of the KNN film (figure 3.3b). The KNN film obtained seems to be not very different with respect the other films obtained in previous works [21], [20]. This can confirm that up to this point the process is in control and capable of producing similiar samples.

3.2.2. Current leakage

A series of current-voltage measurements have been taken out from the sample in both top-top and top-bottom configuration. Measurements where done using a voltage of 3V and a compliance of 100mA for the current to avoid damage to the film. After taking some curves, leakage-mean values are calculated and reported in the graphs (figures 3.4 and 3.5). For top-top measurements good results in accordance to previous studies where found while for top-bottom measurements we have found a very high leakage, mostly ohmic conduction. The density of current has been evaluated considering the fact that the smallest pad between the top and the bottom electrode (or the top and another top one) is the one limiting the flux of current and so it is chosen to be the area to calculate the density of current J.

We can first analyze the top-top measurements in figure 3.4 and in particular since the substrate has been cleaned following the same procedure reported in previous works in

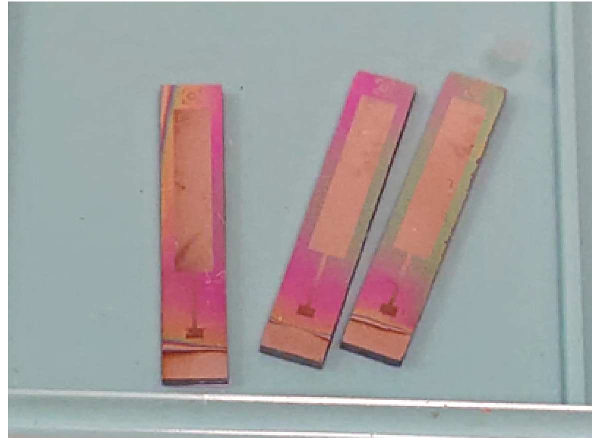

(a) Visual inspection of the obtained cantilevers.

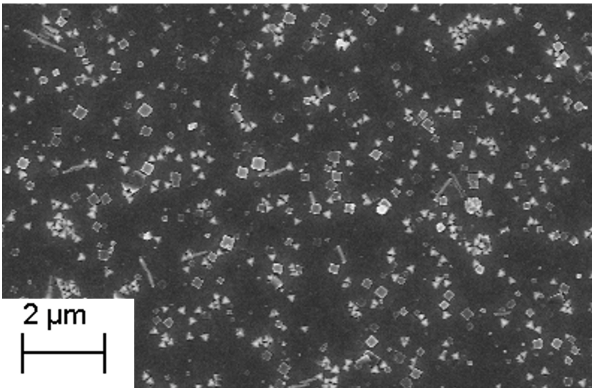

(b) SEM top view of the film. No huge defects are present through the film however many crystallites are arising form the surface representing different orientation. See figure 4.2 for more insights.

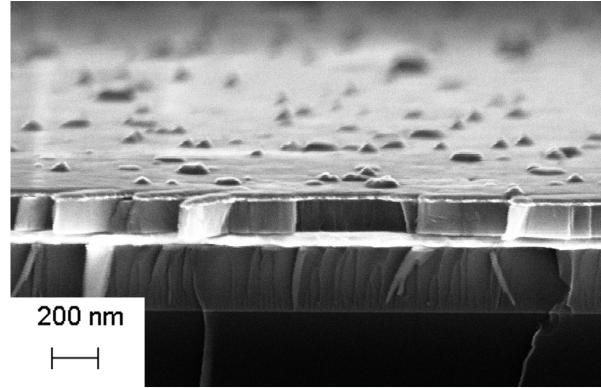

(c) SEM cross section of the cantilever; is it possible to appreciate KNN layered in between the two platinum layers. Also is worth to observe that the KNN film obtained is compact and does not present any mayor defects.

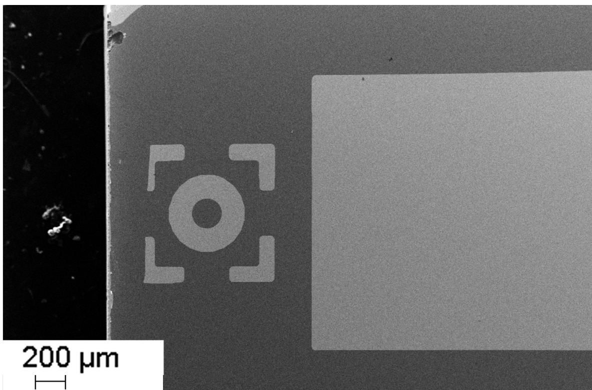

(d) SEM detail of the target of the cantilever.

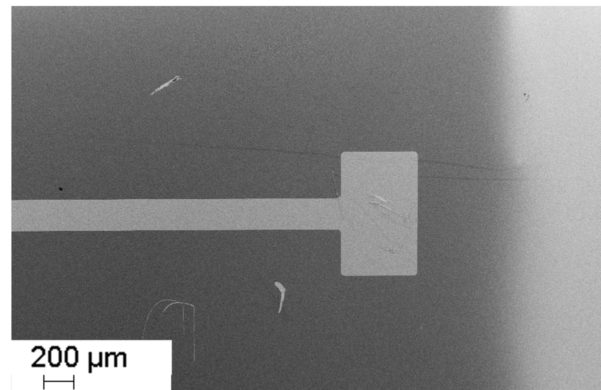

(e) SEM detail of cantilever and the bottom platinum layer.

Figure 3.3: Visual inspection and SEM images of the obtained cantilevers.

order to grow oriented films is then possible to compare then the measurements reported in those past studies as in principle the film should behave similarly [20]. Measurements from the paper by Groppi et al. are shown in figure 3.4e. As it possible to see that leakage follows the same behavior of previous works leading to the conclusion that the grown film share the same properties of the past made KNN films in terms of leakage.

If probing small pads lead to a good measure of the leakage properties of the film this is not always true when increasing the top pad size. In fact, as is possible to observe in figure 3.5, the curves retrieved are mostly straight lines in the $V-I$ graphs. We have interpreted this behavior considering the fact that when choosing as a top metal contact a big platinum pad the probability to cover a huge defect in the film or to find a way to reach the bottom platinum (leading to a short circuit) increases. A comparison with this ohmic behavior and the one that can be given by only a metal is then mandatory. Considering the layer of the bottom platinum as our metal "wire" where current flows we can evaluate its resistance. And so considering it as a slab of $w = 3$mm, $l = 16$mm, $h = 100$nm, is it possible to estimate its resistivity ρ [Ωm] considering its cross section $A = w \cdot h$ and its length l. By retrieving the value of the resistance $R = V/I$ from the measurement (where $V = E \cdot d$ and $I = J/A$, with d being the thickness of the KNN film and A the area of the metal contacts) is it possible to evaluate the resistivity of the ohmic conductions. In particular from figures 3.5c and 3.5d values of $R = 18.75\ \Omega$ and $R = 0.1162\ \Omega$ are found. From here using the formula:

$$\rho = \frac{RA}{l}$$

is then possible to calculate the resisitivity. From the leakage shown in fig. 3.5c, which refers to the top-bottom configuration represented in fig. 3.5a, is it possible to extract (from the ohmic curve) a resistivity of $\rho = 3.5 \cdot 10^{-7} [\Omega \cdot m]$. While from the ohmic leakage curves shown in fig. 3.5d, which refers to the top-bottom configuration represented in fig. 3.5b, is it possible to evaluate for the resistivity a value of $\rho = 3.5 \cdot 10^{-7} [\Omega \cdot m]$. To better estimate the resistivity in this case $l = 2$mm has been used since the top tip is placed very close to the bottom tip. It is clear from the last obtained value for ρ that the model used to evaluate the resistivities is too simple and does not consider other parameters that for sure must be taken into account. Even though the values obtained for the resistivities are unfeasible, the slope of the ohmic I-V curves obtained for the two top-bottom configurations can be comparable with the resistivity of the Pt layer underneath the KNN film ($\rho_{Pt} = 1.06 \cdot 10^{-7}$ [66]). This indeed is an insight that probably there is a spot in the KNN film covered by the top platinum pad which can lead to a short-circuit where the effect of the insulating layer is avoided and the main conduction path is made

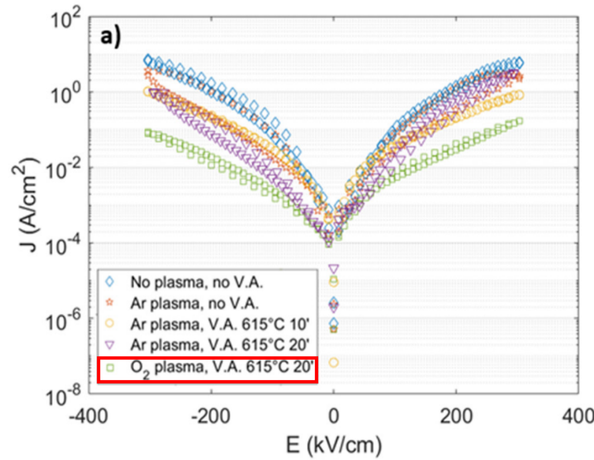

(a) Top-top measurements on KNN films. The measure used to compare the leakage is highlighted in the legend (from [20]).

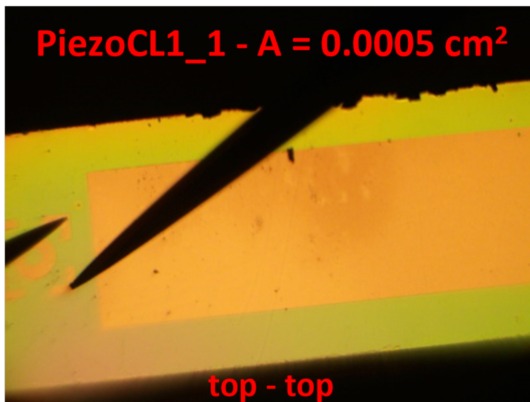

(b) Detail of the top platinum pads from one cantilever used for the top-top measure.

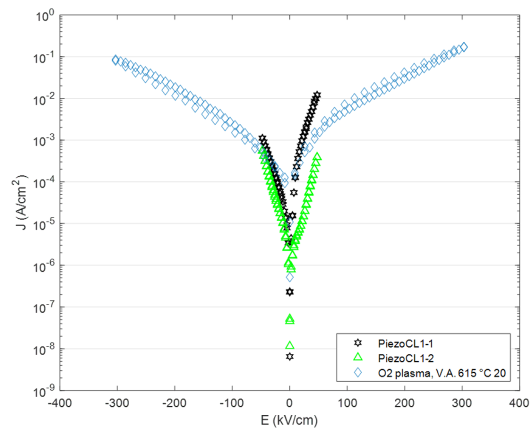

(c) Comparison between the top-top measurements of this work and the one of the past studies. The curves follow the same trend.

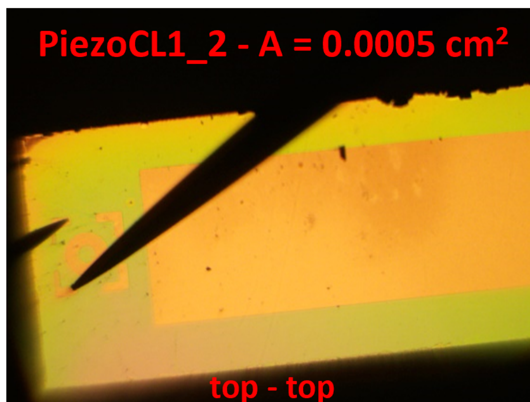

(d) Detail of the top platinum pads from one cantilever used for the top-top measure.

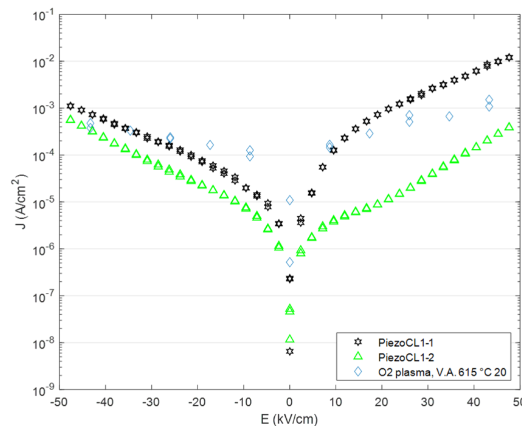

(e) Comparison between the top-top measurements of this work and the one of the past studies. The scale here is enlarged to better appreciate the measurements from this work.

Figure 3.4: Caption

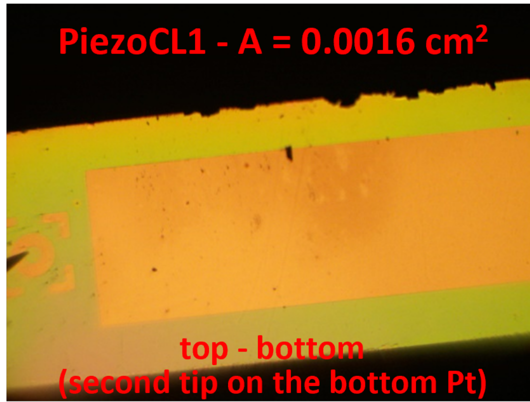

(a) Detail of the top platinum pad used for the measure. Top metal contact is the small circe of the target with an area of $A = 0.0016\ cm^2$.

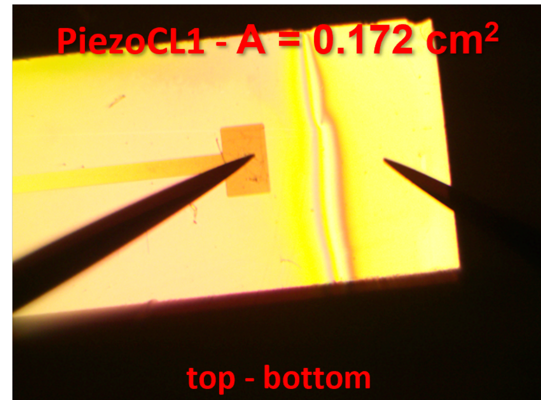

(b) [Detail of the top platinum pad used for the measure. Top metal contact is the T-shaped big platinum pad with an area of $A = 0.172\ cm^2$.

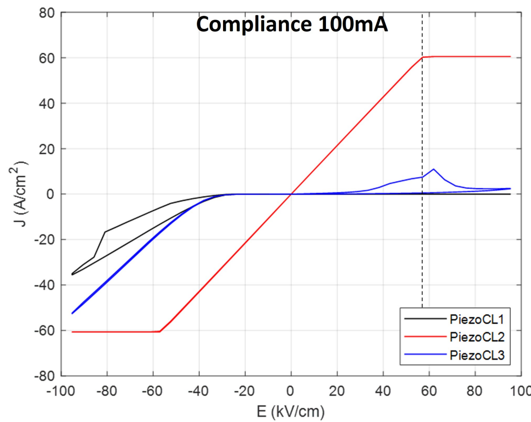

(c) J vs. E graph of the above figure ($A = 0.0016\ cm^2$). Linear scale. The value of the evaluated resistivity is reported. The compliance of the measure is 100mA.

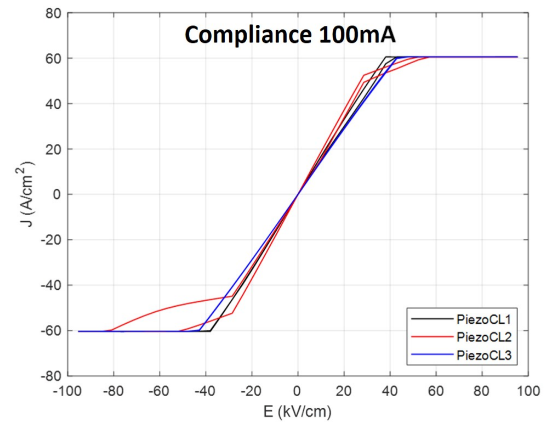

(d) J vs. E graph of the above figure ($A = 0.172\ cm^2$). Linear scale. The value of the evaluated resistivity is reported. The compliance of the measure is 100mA.

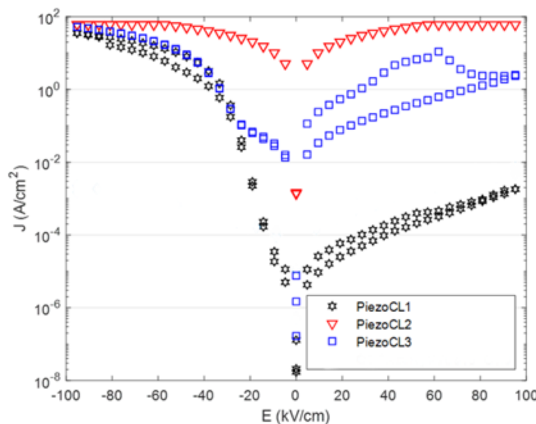

(e) J vs. E graph of the above figure ($A = 0.0016\ cm^2$). Logarithmic scale.

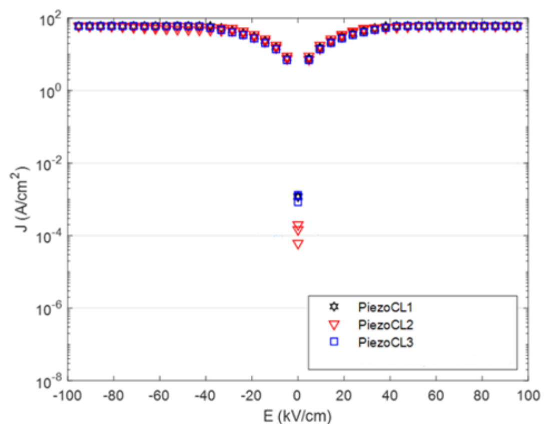

(f) J vs. E graph of the above figure ($A = 0.172\ cm^2$). Logarithmic scale.

Figure 3.5: Top bottom current measurements of the cantilevers. Mean values of the curves are reported

only by platinum. A part from the found ohmic behavior, asymmetric curves can also be seen; this kind of measure will be later analyzed in section 4.2 as it is characteristic of the top-bottom measurements in this KNN film. Last, the huge leakage reported here could also be found due to the arising crystallites from the surface; in fact it has been found that sometimes large crystals arising from the surface are actually connected to the bottom platinum. This kind of defect can enhance the quasi ohmic conduction; an investigation of this can be found in section 4.2.2.

3.2.3. Simulations

Since the geometry of the proposed cantilever is simple, as it is not a suspended structure, it is possible to evaluate its in-plane stress coefficient $e_{31,f}$ analytically or otherwise to evaluate the displacement of the trampoline if all the characteristics are known. For example, it is possible to use for the in-plane stress coefficient the value reported in the paper by Nguyen et al. ($e_{31,f} = 5.6\ C/m^2$) where a fully suspended KNN growth by PLD is characterized [67]. While for the displacement of the tip is possible to use the formula (equation 3.4) by Mazzalai et al. where all dependencies for a full thickness clamped cantilever are shown [64]. Considering then a full stack layered structure the displacement of the cantilever in the coordinate x_2 (reference to figure 3.6) is evaluated using the following equation:

$$w(x_2) = \frac{e_{31,f}(2x_2 - x_1)x_1 c_f (1-\nu)3V}{Y t_{Si}^2} \tag{3.4}$$

where $t_{Si} = 725\ \mu$m is the thickness of the silicon substrate, $\nu = 0.064$ is the Poisson ratio for the SCS(001)[110], $Y = 169$ Gpa is the Young modulus of silicon [68], $x_1 = 15$ mm is the length of the piezo patch, $x_2 = 15$ mm is the spot where the laser is measuring the displacement of the trampoline, $e_{31,f} = 5.6\ C/m^2$ is the dielectric piezo coefficient [67], $c_f \sim 1$ (for simplicity) is the ratio between the area of the cantilever (i.e. the piezoelectric layer) and the area of the top electrode, finally V is the applied tension to the structure ($V = E/t_{piezo}$ with E being the applied field and $t_{piezo} = 300$nm the thickness of the KNN layer). With these conditions, a total displacement of 400nm has been found upon applying a 10 V static tension; this result is shown in figure 3.6b. Another simple finite elements simulation has been performed through COMSOL Multiphysics ® [69] where a four layered material Pt(50nm)/Piezo(300nm)/Pt(100nm)/Si(725μm) is stressed with a DC signal of 10V. The piezo material in between the two metallic pads is characterized by the values reported in literature [67] while for the other materials the data is already present in the database. The edges of the structure facing right in figure 3.6c are kept fixed

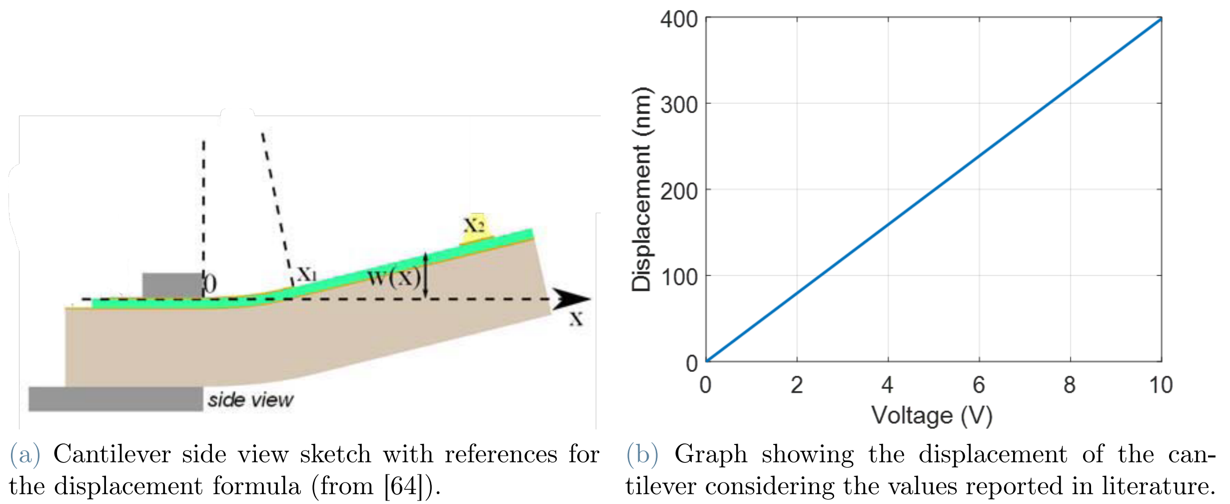

(a) Cantilever side view sketch with references for the displacement formula (from [64]).

(b) Graph showing the displacement of the cantilever considering the values reported in literature.

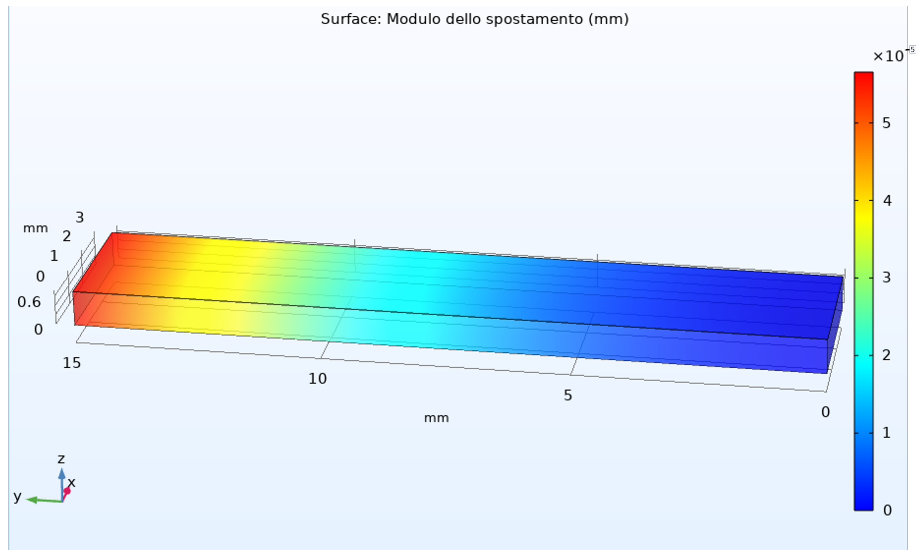

(c) 3D color coded representation of the cantilever obtained through COMSOL.

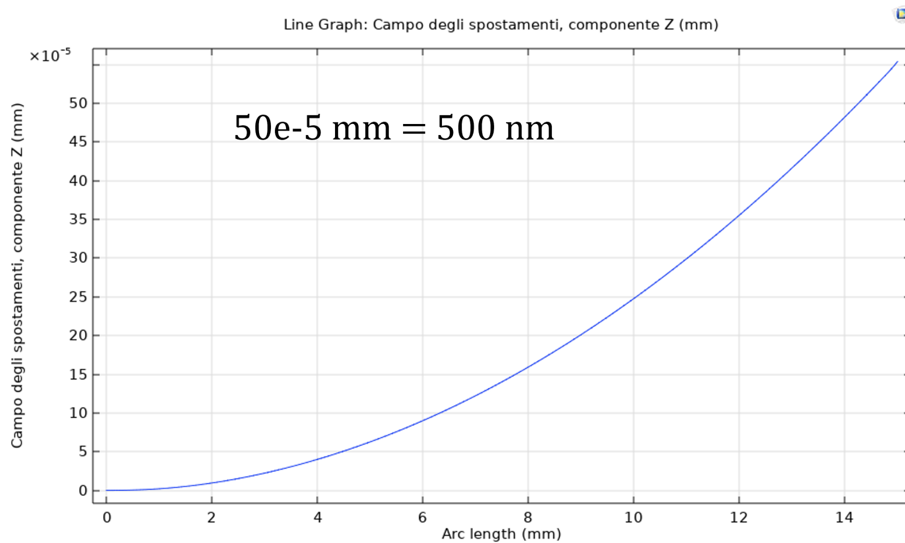

(d) Displacement of the structure along the y axis for a 10V applied voltage.

Figure 3.6: Numerical simulations results.

to a imaginary wall. With this conditions a total displacement of $\sim$ 500nm is found, not so far from the analytical model. Is it possible to conclude then that the analytical model can match the numerical simulation; for sure a more detailed study of the parameters is required to achieve a better precision in the physical model.

3.2.4. Measurements from STM

The cantilevers samples were given to a STMicroelectronics facility to be tested for piezoelectric characteristics such as the piezoelectric response probing with an AC signal and the displacement upon an applied field. The dynamic hysteresis measurements and the capacitance-voltage measurements were extracted using the Keysight B1500A Semiconductor Device Parameter Analyzer [70]. In particular to extract the polarization-voltage curve a triangle waveform has been used with frequency range of 10 Hz to 1 kHz and a amplitude of 1V to 5V. Both two curves obtained, the one at 10 Hz and the one at 1 KHz, show a purely resistive behavior as is not possible to define a saturation polarization for a certain voltage [67], [71]. In figure 3.7a and 3.7b this result is shown. Capacitance-voltage analysis were also carried out using an AC signal at 1 kHz varying the amplitude from 0.5V to 2V. This measure is reported in figure 3.7c. Is it possible to observe that the curve is very noisy and difficult to be interpretable as a valid result. STM conclusion

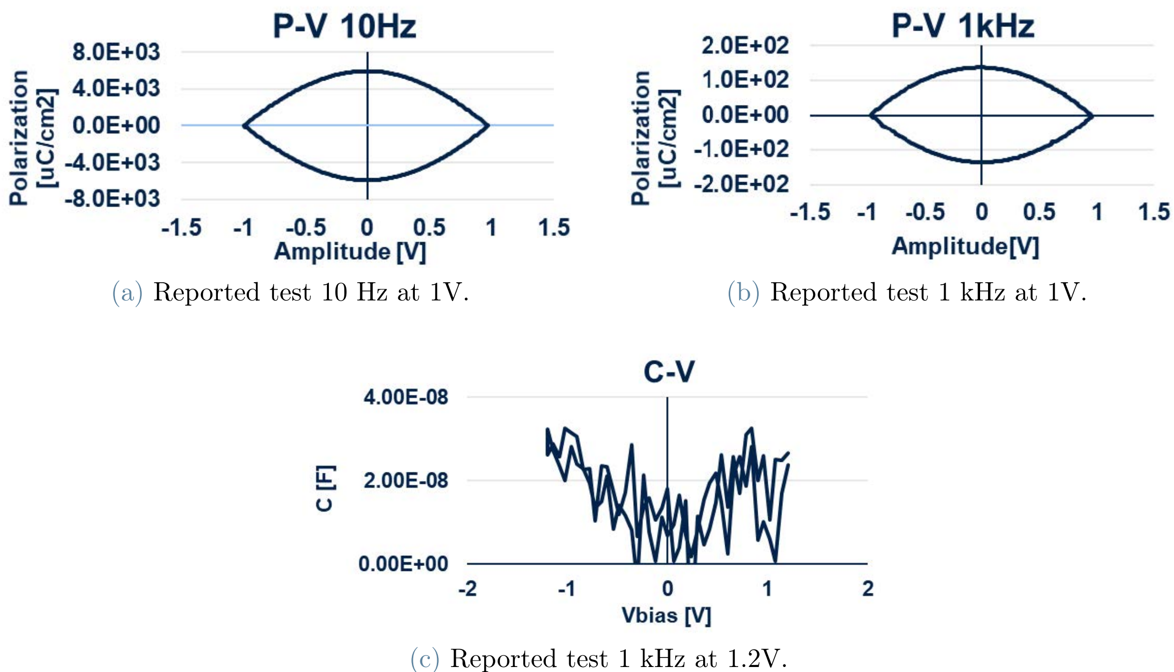

(a) Reported test 10 Hz at 1V.

(b) Reported test 1 kHz at 1V.

(c) Reported test 1 kHz at 1.2V.

Figure 3.7: Keysight B1500A characterization. Courtesy of STMicroelectronics.

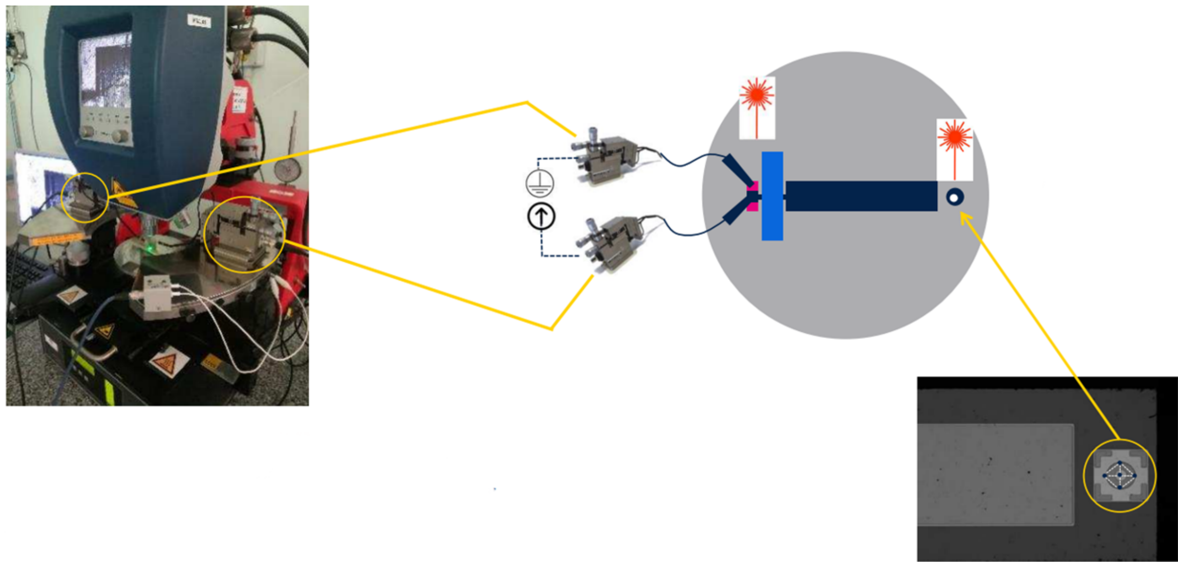

(a) Polytec laser vibrometer measurement setup.

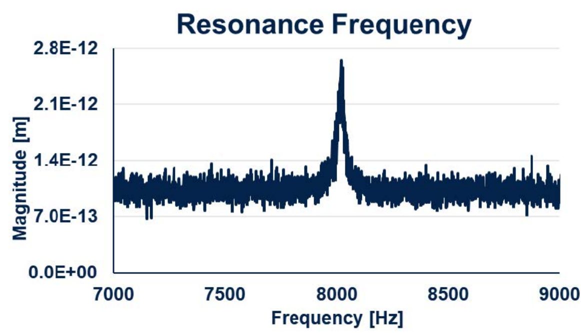

(b) Resonance Frequency Spectrum (frequency domain). The found resonant frequency is ~ 8 kHz.

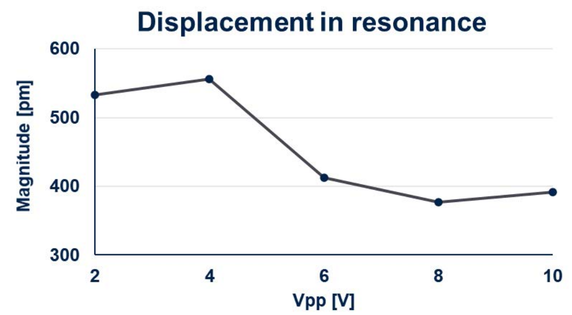

(c) Displacement of the cantilever measured in resonant condition in function of a sinusoidal signal.

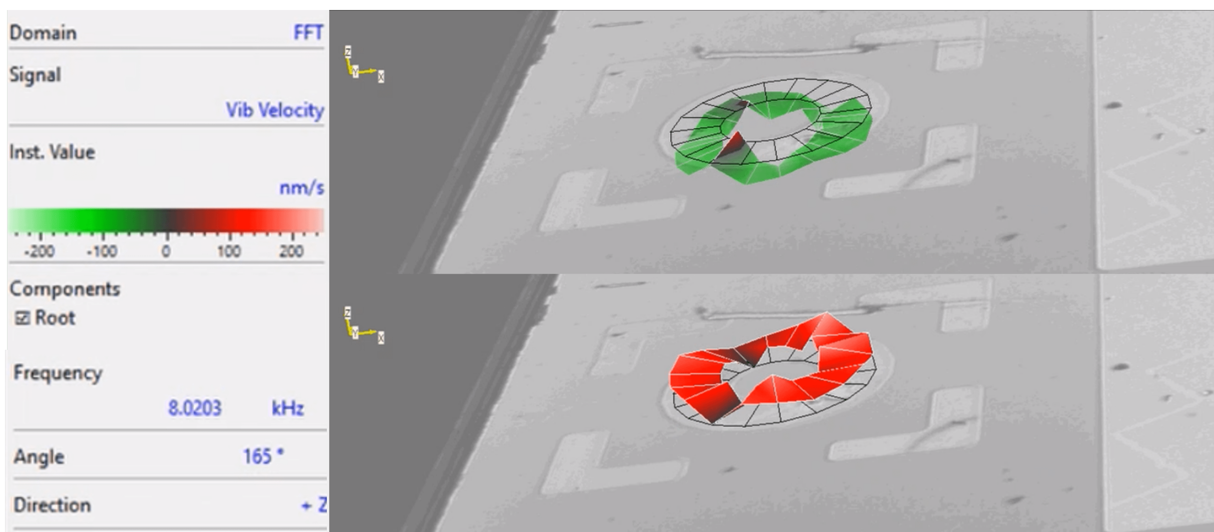

(d) Frames of the video showing the motion of the cantilever at resonant frequency.

Figure 3.8: Vibrometric measurements. Courtesy of STMicroelectronics.

was in fact to say that this was an unreliable measurement due to noise. In conclusion to this first analysis no valid behavior is found for a capacitor as the polarization-voltage doesn't show any hysteresis loop. This can be due probably to its high leakage. In fact, not shown I-V measurements confirm that it acts as a resistor showing a short-circuit behavior. Is it possible to measure the cantilever deflection under application of a voltage using a Polytec laser vibrometer [72] (figure 3.8a). The bottom pad access of sample is kept fixed letting the active area free to move under the applied field. A laser hitting the target of the cantilever is being reflected; the change in position of the reflected laser determines a displacement of the cantilever. In principle two analysis are required; the displacement in the normal frequency range and at its resonant frequency. In the normal regime the displacement of the cantilever has to be linear while in the resonant domain the displacement is non-linear. A first analysis in the frequency domain has been carried out to find the resonant frequency. The analyzed frequency range is from 0.5 kHz to 10 kHz, while the applied signal is a periodic chirp with null DC component and a amplitude of 0.5V for the AC component. The resonant frequency is then found to be $f_{res} = 8.02$ kHz with a maximum displacement of 2.64 pm. The FFT graph can be seen in figure 3.8b. Since it was not possible to measure the displacement in non resonant condition, an attempt to measure the non linearity of the deflection in resonant condition has been made. For this, dynamic motion analysis a sinusoidal signal has been applied varying from 2V to 10V. The maximum displacement for each voltage is reported in figure 3.8c where it also possible to appreciate that it is not linear with the applied voltage as it should be when stressed in a non resonant frequency domain; the non-linearity in resonant condition is then confirmed. A couple of frames taken from the video showing the displacement in resonant condition are shown in figure 3.8d; here is possible to see by a color coded image the displacement in the vertical direction for a AC signal. In conclusion the measurements done by the STMicroelectronic team shows a device which is not able to behave like a capacitor. In particular, even if out of resonance the trampoline seems to move upon an applied AC signal, the amplitude of the displacement is not appreciable and can be associated also to Brownian noise.

3.2.5. Conclusion and future directions

FEA simulations have demonstrated that the simple adopted stack model can be a valid approach to evaluate the piezoelectric characteristic of KNN. Also, the cantilever fabrication process seems to be feasible in order to obtain what, is in principle, a functional trampoline to be treated as a transducer. Since we have not tried parameter optimization in the fabrication, we cannot consider the configurations used for the realization and the

final obtained layered structure to be the optimal ones. For sure, the process of cantilever fabrication can be improved under a lot of aspects such as the realization time and the different parameters such as, for example, the development time after the UV exposition, or the plasma cleaning power. For certain one thing that has to be improved is the quality of the films since the major piezoelectric properties come from a low current leakage; this is confirmed by the measurements performed by STMicroelectronics where it is evident that piezoelectric characteristic cannot be retrieved due to the resistive behavior of KNN. Minimizing the quantity of defects present in the film can be a solution to improve the current leakage; to do so a new process can be exploited. Only after the improvement of the piezoelectric characteristics of the growth KNN film it would be interesting to consider to develop a process for a fully suspended trampoline.

4 | Asymmetric leakage in KNN capacitors grown by PLD

One crucial property that a piezoelectric material must have in order to become a proper candidate for MEMS applications is a low current leakage value; in fact this can lower the d piezoelectric coefficients that tells us how much strong is the conversion between mechanical stress and current signal (such as the d_{31} and the d_{33}), this in particular is important for out of plane sensing cantilevers [73]. In this section, films are probed in a top-bottom configuration and current leakage is measured. A huge dependance on the type of metal used as top pad, with a common bottom Pt electrode, is found and different models for the current are considered. For this discussion only classic PLD processed films are studied.

4.1. Overview of characteristics of films

In order to deposit four different types of metal pads two 1x1 cm^2 samples of KNN had to be grown and cut in half to create four samples with metal. By doing this, as we were dealing with two slightly different samples, slightly different thicknesses were found. In particular we have a 270 nm thick film for the film with cromium and titanium and 300 nm for Nickel and Platinum pads. Films were analyzed using SEM to retrieve morphology and stoichiometry. Crystal orientation was explored with XRD analysis. Overall, the two samples have good morphology properties. They both are compact and have a preferential crystal orientation through the film; moreover they are coherent with the previous works [21], [20].

4.1.1. Crystallographic orientation

X-rays crystallographic measurements (XRD) have been performed on those two samples with an energy for the $\theta - 2\theta$ diffraction experiments of 8.04keV (30 mA/40 kV) using a $K\alpha$ copper source. All the measurements were taken at room temperature. With the obtained

diffractogram is possible to study quantitatively the orientation of the grown film; different peaks represent different orientation of the crystal. The diffractogram obtained follows the one of previous works [21], [20]. A comparison can ben see in fig. 4.1. The process is then stable and repeatable to obtain KNN(001) oriented films. The orientation of the film is crucial for piezoelectric properties as a better orientation can provide enhanced piezoelectric coefficient. The peak KNN(011) can be related to misoriented crystallites that can also be seen in the SEM pictures (fig. 4.2). The deposited films shows a strong preferential direction for the KNN in KNN(001) leading to a uniform film. Is it possible also to observe that in the acquired diffractogram, for this work the peaks KNN(100) and KNN(200) are much more visible with respect to the previous work; this is due to a better resolution of the used XRD instrument.

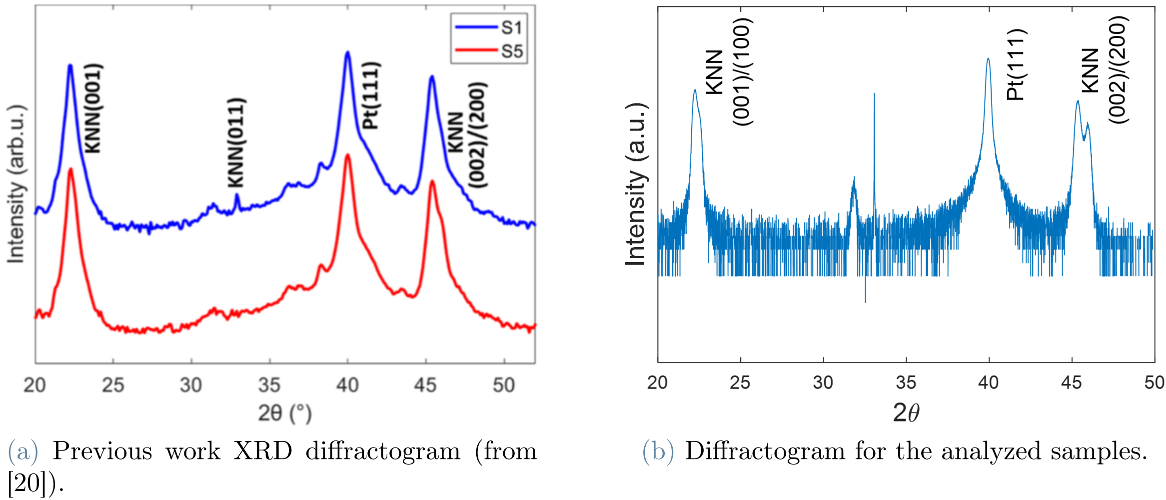

(a) Previous work XRD diffractogram (from [20]).

(b) Diffractogram for the analyzed samples.

Figure 4.1: Comparison of XRD diffractogram. On the left, the one taken from past works is shown while on the right the acquired diffractogram of films deposited in this work is shown. As it is possible to observe, the two diffractogram show strong preferential growth direction of the KNN out of plane. Other peaks such as KNN(002) and KNN(200) are clearly visible in the diffractogram acquired in this work; this is due to the multiplicity of the Bragg's law (see section 2.3.3).

4.1.2. Morphology

The films showed both uniformity and compactness, no huge physical defects are found through the entirety of the film (fig. 4.2). Is thus possible to observe misoriented crystallites arising from the surface; in particular in the cross section images (fig. 4.2e-f). An interesting feature that can emerge in high ordered piezoelectric films is related to the

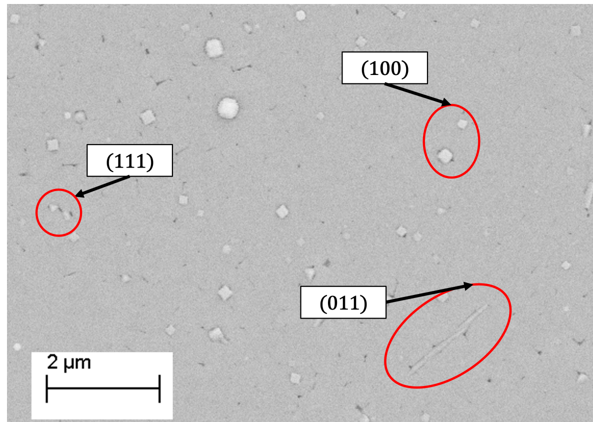

(a) 270 nm sample. SEM top image taken with secondary electrons. Is it possible to observe outgrows and other crystal orientations.

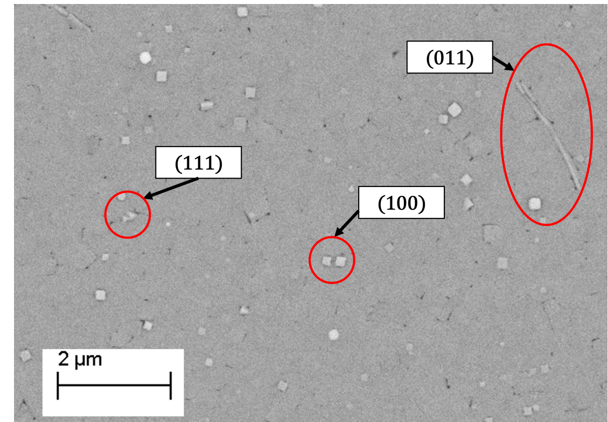

(b) 300 nm sample. SEM top image taken with secondary electrons. Is it possible to observe outgrows and other crystal orientations.

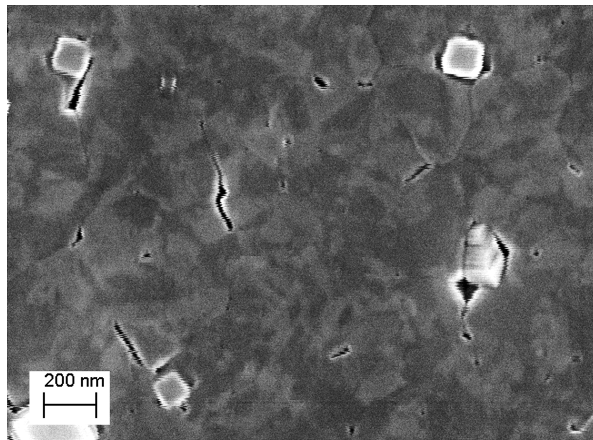

(c) 270 nm sample. SEM top image. Is it possible to observe ferroelectrics domains and outgrows.

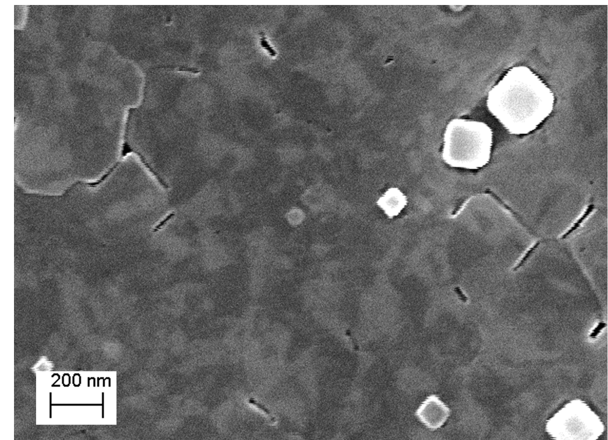

(d) 300 nm sample. SEM top image. Is it possible to observe ferroelectrics domains and outgrows.

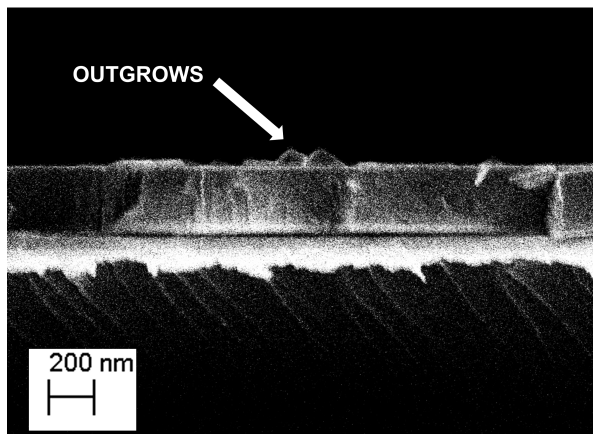

(e) 270 nm sample. SEM cross section image. is it possible to observe outgrows coming out from the surface.

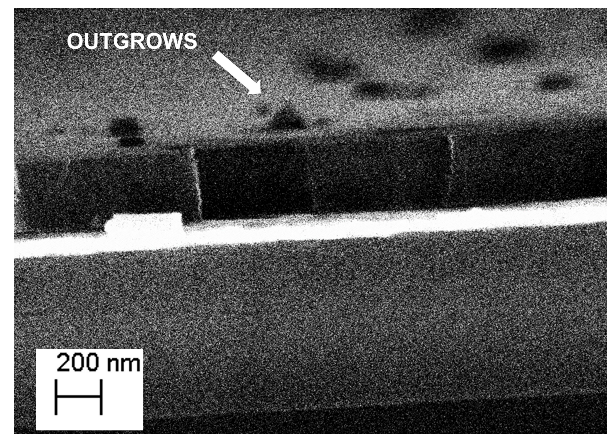

(f) 300 nm sample. SEM cross section image. is it possible to observe outgrows coming out from the surface.

Figure 4.2: Comparison between the 270 nm film and the 300 nm one. The films are very similiar and share the same morphological properties.

black and white zones that can appear on the surface of the sample in a SEM measure; this texture has been observed in literature and can be related to the material's spontaneous ferroelectric domains [74], [75]. The dark zones and the light zones correspond respectively to opposite domain polarization [76]; this effect has also been observed in previous works and has been correlated also to the the presence of (001) orientation of the film that can enhance the this spontaneous polarization perpendicular to the film surface [20], [77]. This can all be observed in figure 4.2 where the two films are compared side by side. Is it possible to observe that they are mostly identical even if they come from two different runs; the only difference comes from the fact that one sample is 270 nm thick while the other is 300 nm thick.

4.1.3. Film stoichiometry

As already reported in previous works [21], [20], one of the major problem related to KNN films is related to alkali components as they have the tendency to be more volatile with respect to other elements at high temperature. In particular alkali are know to be lost during the deposition phase ($\sim$ 615°C) and annealing phase ($\sim$ 500°C) of the PLD process. This has the effect to lower the stoichiometry ratio between potassium and sodium with respect to the other elements and can also have some effects on the leakage properties. In particular a high current leakage is related to alkaline vacancies [78]. EDX analysis was conducted on the films considering for each measure a different 1x1 mm^2 section. For each measure, four repetitions has been done. The reported value is the mean value calculated between them. The energy used to obtain the diffractogram was fixed at 10kV, which was good enough to probe the material deposited. With the obtained diffractograms three ratios have been studied as they can be representative of the stoichiometry of the film: Na/Nb, K/Nb and K/Na. The oxygen signal has been also acquired, but since the diffractogram were taken ex-situ the exposition to the controlled but still normal atmosphere, can change in principle its quantity, making the oxygen peak not representative for our analysis. The ratios can be seen in table 4.1 and are in perfect agreement with previous works [21], [20]. In fact, it is possible to observe that the stoichiometry of the film is not the one of a perfect KNN ceramic but instead we can see that a small quantity of the alkaline component has been lost. Still, the ratios obtained are considered to be in good agreement for most of the applications in literature [79]. The loss of alkali ions can be related to higher current density leakage.

Na/Nb	K/Nb	K/Na
0.44	0.41	0.91

Table 4.1: Stoichiometry ratios obtained analyzing the EDX diffractogram.

4.2. Measurements variability

After a first visual inspection metal contacts were placed on top of the films and top-bottom measurements have been performed at different voltages. This kind of analysis is important as previous studies [21] have demonstrated that different kind of metals pads can have a huge effect on the measured leakage. It is already know at this point the Pt is the best material to obtain good leakage results but is rather expensive thus other materials such as Ni, Ti and Cr are employed since are cheaper; however their usage come with the trade off that the current leakage is higher. The bottom pad is kept always at ground potential (i.e. 0 V). The different materials used as contacts have a different behavior regarding first of all the ability to sustain higher voltages. In particular it has been observed that platinum is able to sustain much higher voltages with respect to the other metals; in terms of performances nickel can be compared to platinum (but still have a lower resistance after a certain voltage) while titanium and chromium having the worst even at low voltages.

Even though different metals have a different resistivity in terms of intensity of the applied voltage it is possible to observe that a great dispersion in the measurements is found between metal pads of the same material in a rather small area portion of the film. In fact I-V measurements performed on a film region show a very different leakage behavior depending on the chosen film (fig. 4.3). The curves obtained are in fact different both in terms of current intensity and slope. The latter is usually associated with different conduction mechanisms.
Another feature observed in the leakage measurements between different pads and different material is the degradation of the pad/film after a certain amount of cycles due probably to the stress of the applied voltage; this is shown in the graphs reported in figure 4.4. Here the blue line represents the very first measure performed on the pad while the red curve is the last current density measured. Measurements taken between those two are also reported in black. The effect of the degradation of the pads can also be observed in figure 4.5 where huge defects are introduced to the pads due to high voltage (i.e. the breakdown voltage). When this happens, usually the measure observed is more like a short circuit (current value was usually limited to 100mA - 300mA to avoid more damages to the film).

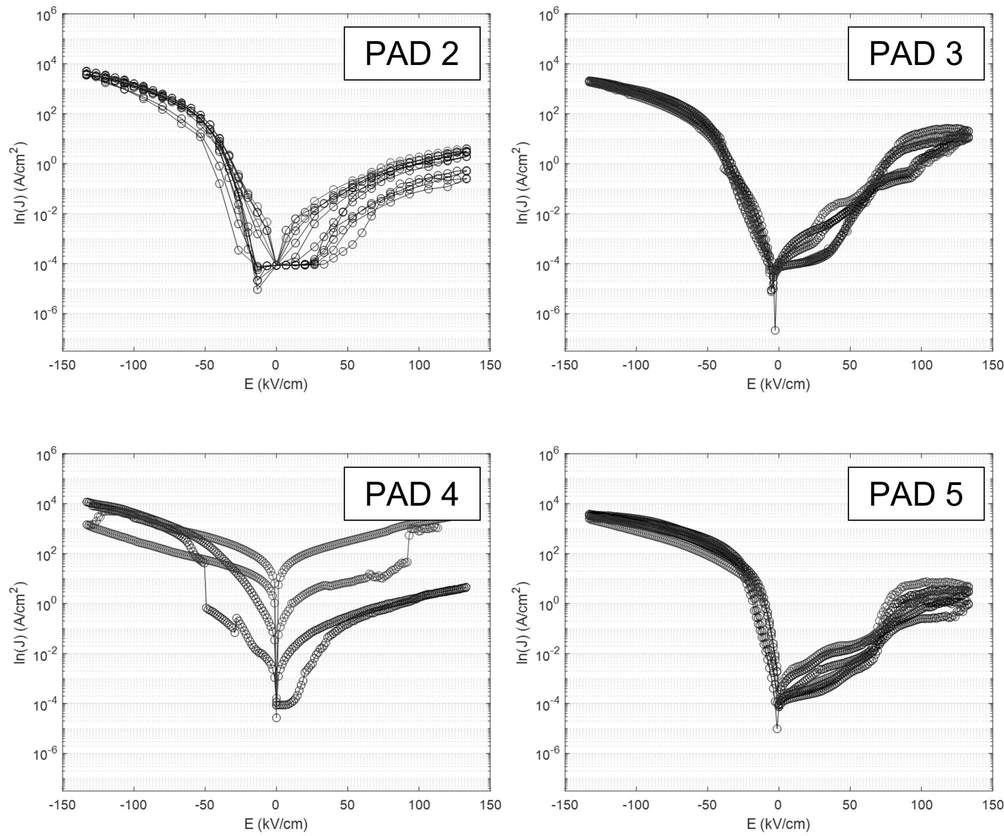

Figure 4.3: I-V curves taken at 4V for different Ni pads on the same portion of film. Curves are reported in black to better visualize the dispersion trend of the measurements.

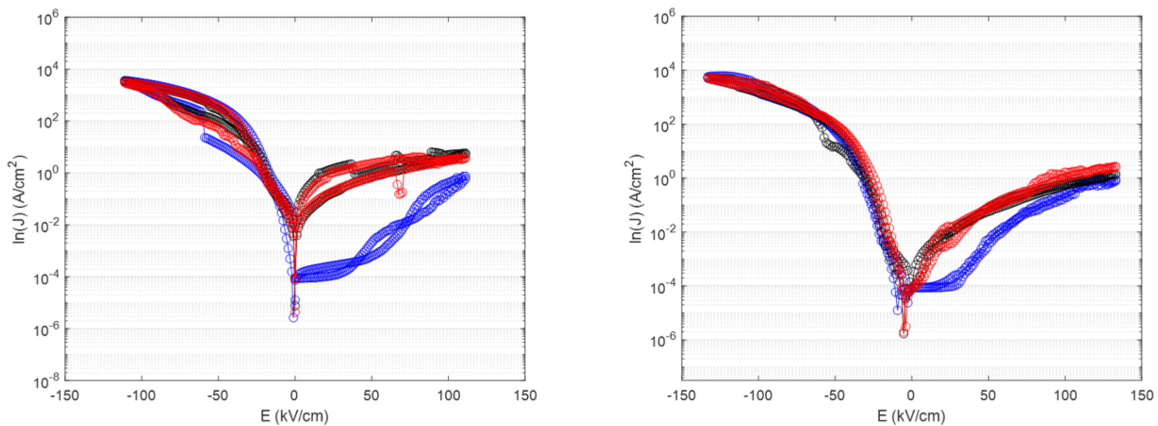

(a) Chromium pads degradation trend at 3V.

(b) Nickel pads degradation trend at 3V.

Figure 4.4: Increasing current density leakage after cycling different measurements on the same metal pad. Blue line is the first measure, red line is the last one and black lines are the ones taken in between.

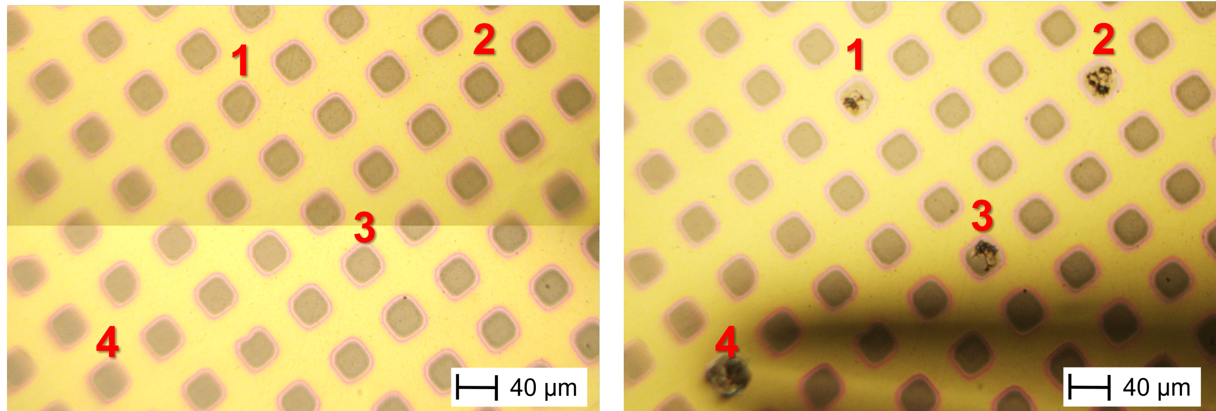

(a) Platinum pads before the measurements.

(b) Platinum pads after a full cycle of measurements. For each pad the breakdown/melting voltage is around 7V.

Figure 4.5: Burned pt pads after reaching the breakdown voltage, pads are clearly damaged due to the applied voltage. This image can also be taken as a reference to understand how much variability we can have in the same small region.

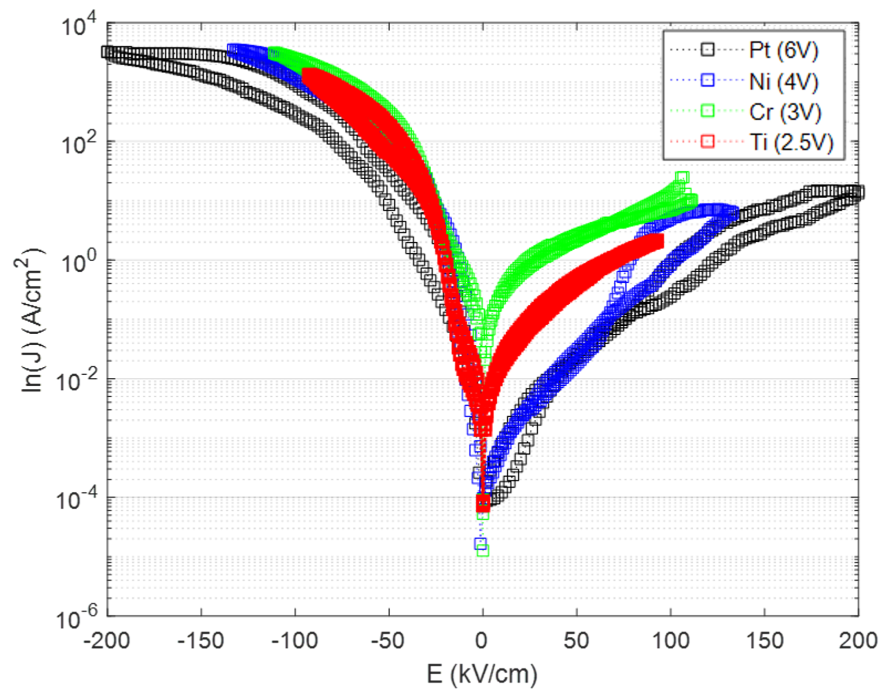

Figure 4.6: Mean current density leakage values for different metal pads. Platinum is able to sustain up to 6V while titanium pads were already breaking at 3V. The asymmetry in all of the pads is evident.

Those trends that have been found while measuring are an indication of the fact that the KNN films are not homogeneous and have defects that can lead to a higher current leakage or a complete different behavior. Also, the quality of the metal contact should be taken into account as they have the tendency to be damaged after a certain number of measurements; to do so another technique with respect to the classic sputtering can be considered. Considering this large variability and discrepancies among measurements, only the meaningful curves have been considered and mean values calculated. A summary for this story is shown in figure 4.6 where all the mean values of the current leakage for different pads are graphed. Since metals affect the dielectric properties of the KNN film pads can easily have a breakdown even at small voltages; different metals can sustain different voltage intensities. From figure 4.6 another important aspect of the current measurements can be extracted: the asymmetry of the measurement. In fact is it possible to notice that the two branches, positive and negative voltages, have a very different leakage; in fact the right branch has always a lower leakage and the slope of the curve is much less pronounced. This is more evident for nickel and platinum pads while for titanium or chromium the two branches are not very different.

4.2.1. Influence of top-electrodes on leaking current

From figure 4.6 is possible to extract two conclusion: different metals lead to different current density values and the measure is asymmetric even if in principle the system can be fully symmetric (for example in the Pt/KNN/Pt stack). The first observation can be explained using already present results in literature. As it is reported in the literature, the variation in the magnitude of the leakage current of a ferroelectric thin film in a MIM stack usually correlates with the different d-shell occupation state and with the electronegativity of the metal used for electrodes [80], [81], [82].

Metal	d-shell	Electronegativity (Pauling)	Work function [eV]
Pt	$5d^9$	2.20	5.65
Ni	$3d^8$	1.91	5.15
Cr	$3d^5$	1.66	4.50
Ti	$3d^2$	1.54	4.33

Table 4.2: Electrode materials properties (from [83]).

The higher the d-shell occupancy state or electronegativity, the lower the leakage current. In table 4.2 is possible to observe relevant parameters for each electrode material, ordered from the lower leakage metal to the higher current density leakage metal based on what just reported. From the data obtained (fig. 4.6), we can see a good accordance of our

results with the model proposed. In fact Pt is the electrode material which has the lowest leakage and is also the material with the higher occupancy of the d-shell. Then we have in this exact order Ni, Cr and Ti. Ni pads leakage are in good agreement with the model while Cr electrodes need further considerations; in fact according to the d-shell filling and the electronegativity, the Cr contact leakage current should be in between Ni and Ti but from what we have observed the density of current is higher with respect to the one provided by Ti pads. This is true for the positive biased branch where this incoherence with the model is evident while for the negative biased one one could say that the model is working. It is also possible to see that Cr electrodes show a higher leakage than the other electrodes materials, thus the correlation between the different occupancy state of the d shell of the electrodes different metals and the electronegativity with the leakage current density seems to be consistent with the results. Previous works have encountered this leakage trend but the conclusions were different not only in selecting which metal pad has the highest leakage but also they have encountered a different rectifying behavior; in our work the most pronounced rectifying behavior is given by the Pt pads while in the work of Shweta et all. [81] platinum pads produced a symmetric behavior, the same for palladium (another metal used in their work to create contacts); this had been linked to the occupancy of the d-shell ($4d^{10}$ for Pd).

4.2.2. Potential barrier at the bottom pad

In literature is it possible to find a similar leakage asymmetry for other MIM (Metal-Insulator-Metal) systems [84], [85] as well for piezoelectric stacks such as PZT and KNN [86], [87]. This rectifying behavior is then a characteristic of those stacks and similarly in our case a high current leakage was only obtained when the stack was probed with a negative bias while when a positive voltage was applied the intensity of the leakage is to be attributed to the nature of the metal. The important result in the obtained data is to point out that top and bottom interfaces are substantially different from one another; in particular it seems that the bottom interface is limiting the flow of charges when the top electrode is biased with a positive voltage. This effect is more evident at lower voltages; in fact is it possible to see that even if in figure 4.6 the effect is already evident by considering lower voltages (in particular for Pt and Ni) this behavior is much more present as they even show a quasi flat curve at low voltage, so basically only a tiny current flows through the system. This is presented in figure 4.7a. We have thus a rectifying behavior such as the one of the diode depending on the sign of the voltage applied at the top metal contact. This suggests the presence of a potential barrier at the bottom interface and this is typically attributed to the presence of oxygen vacancies in the proximity of

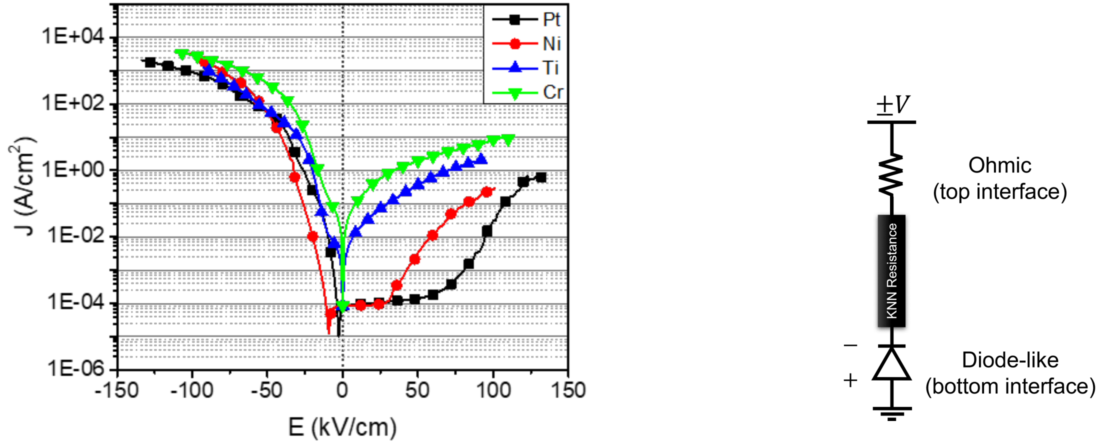

(a) Current density leakage measurements for different metal pads. Used voltages are limited to 3V (from [90]).

(b) Simplified electrical model for the Metal-KNN-Platinum stack (from [90]).

Figure 4.7: Figures taken from [90].

the Metal-Insulator contact [88], [89]. This barrier creates a net effective potential barrier that can overcome the migration of the charges in one direction [40]. Is then clear that the bottom and the top interface behave in a very different way, respectively we can describe the bottom interface as a rectifying Schottky junction and for the top interface we can point out that it behave almost like an ohmic contact . A simplified scheme of a proposed equivalent circuit is shown in figure 4.7b. From the figure, considering the diode, is even possible to associate as "forward bias" the negative voltage applied and as "reverse bias" the positive applied voltage.

Trying to understand the origin and the location of the potential barrier, Conductive-AFM (C-AFM) measurements on the samples were performed. In particular, no metal pads are considered in the discussion, only bare KNN/Pt stacks were probed. All the outcomes of this analysis are reported in figure 4.8; here it'is already possible to observe a topography of a section of KNN surface with squared outgrows (indicated before as KNN(100)) and agglomerated particles on the surface, which lie at slightly different levels above the surface (10-30 nm). The sample was silver pasted to a metal holder; thanks to this we have set the tip of the AFM to zero potential while the bottom Pt was kept at +3 V. In this configuration current was collected during the scan. Electrical properties for the KNN film are otherwise uniform across the majority of the surface, according to C-AFM testing. However, the borders of some square outgrows have some notable hot spots. It's interesting to note that just a few of the crystals, primarily the larger ones, are affected by this finding. There is no present contrast for the agglomerated particles

or smaller crystals. This suggests that although the smaller crystals are either just on the KNN surface or do not make direct contact with the bottom Pt, the bigger crystals may have a direct link to the bottom interface and be fully embedded into the KNN matrix below. Indeed, a cross-section SEM image of a KNN/Pt film was used to experimentally confirm this. On top of the Pt bottom layer can be seen in the figure a compact KNN film. However, a few crystals with square faces are also discovered. The one on the far left that is smaller appears to have sprouted from the KNN surface. However, a larger one on the right demonstrates that one crystal edge extends all the way to the KNN-Pt interface at the bottom. According to the finding, current preferentially passes via some crystal boundaries that exist from the very beginning of the film deposition. Additionally, these KNN characteristics have been linked to a larger concentration of defects, particularly oxygen vacancies [91]. When negative bias (-3 V) was applied to the sample,the C-AFM image did not show significant contrast. This seems to imply and confirm that only the bottom interface is limiting the electrical conduction to KNN while the top contact is not.

After pointing out this evident behavior, local conduction measurements were taken in four different points (figure 4.8d). Is it possible to see that when the tip is placed on the conductive edges of the crystal a large current develops saturating the detector (points 1 and 2); moreover the current shown is not symmetric as it only appears for positive bias and not for negative voltages. This again points to the formation of a barrier at the bottom interface and exhibits a diode's activity. It's interesting to note that an asymmetrical current also forms for a few measurements on less leaky areas, but this time its value is significantly lower. The current measured not on the edges of the crystal show a peak that might result from KNN moving to a unipolar polarization state, or it might be the result of some other charge migration and excitation phenomenon. The introduction of a negative bias, however, results in the absence of a comparable peak, indicating once more that there is a barrier at the bottom, causing voltage reduction. It is not clear if we are dealing with a genuine switching peak despite the current peaks' centers being at 56 kV/cm and near to the coercive field for KNN (40 kV/cm [92]). To understand this a P-E loop can be measured using ferroelectric analyzer; peaks in this way should be more visible if the material behave as a good ferroelectric [93]. Despite the doubt, a potential barrier is clearly present at the bottom interface, and hot current spots are present on the film as a result of crystal boundaries connected to the bottom Pt electrode. The hot spots make up 3% of the C-AFM image's surface area but account for roughly 30% of the leakage current through the film, according to an estimate of the total charge passing through them. This means that hot spots are an important element for the leakage of the KNN films but still not the main factor; still they can for example explain the great

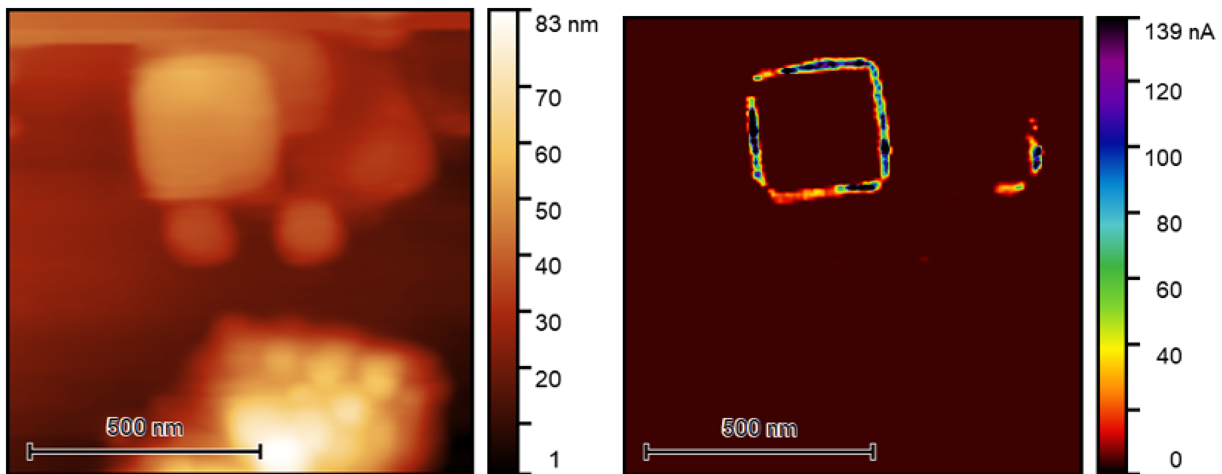

(a) AFM topography of bare KNN surface on bottom Pt electrode.

(b) conductive-AFM image of the same area with variation in leakage around crystal borders.

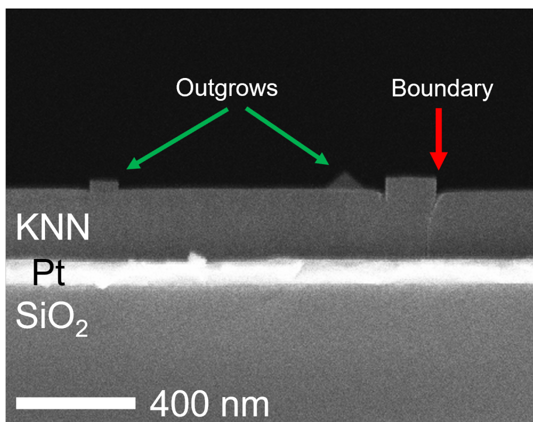

(c) SEM cross-section image of a KNN/Pt/SiO_2 stack (from [21]). A direct access to the bottom Pt is clearly visible.

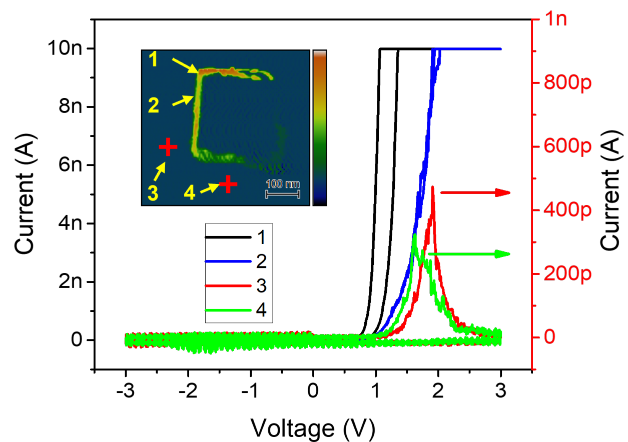

(d) I-V characteristics of several spots on the film as measured by C-AFM.

Figure 4.8: C-AFM measurements and topography (from [90]).

dispersion in the current measurements among different pads in the same area (i.e. a pad covering a defect). In view of the experimental Metal-Insulator-Metal stack behavior, but also in the assumption that only the higher barrier interface at the bottom dominates the current, the system has been considered instead as a metal-semiconductor Schottky interface (MS) device, with an ohmic contact attached to the semiconductor (top electrode) [94]. The simplified electrical model (figure 4.7b) describes how the electronic current is allowed mostly in one direction (towards the bottom Pt).

Considering the diode as Schottky-semiconductor interface, capacitance measurements were made in the reverse bias. This characterization in fact is usually performed to verify the Schottky diode model. In particular we have measured a small signal capacitance as a function of the applied bias. This characterization has been performed in the assumption that only the higher barrier at the bottom dominates the current. A series of measurements has been performed only on the samples with Pt and Ni pads as they show a huge asymmetry even at low applied voltage; due to this they can give back reliable capacitance measurement (fig. 4.7). Moreover the capacitance of Ti and Cr was also measured but was not significant as they show an ohmic-like contact behavior. A small AC signal (50 mV - 10kHz) has been applied on the top metal contact in the condition of reverse bias (and so with a positive applied voltage while the bottom contact was kept at ground condition) and the complex capacitance was measured using a LCR meter (Keysight E4980A). From Schottky theory the inverse of the square capacitance should show a linear behavior with the applied voltage; this is exactly what can be depicted from the graph where the behavior of $1/C^2$ vs. the applied voltage is shown (figure 4.9). From here is it possible to observe a linear behavior thus confirming that we have a Schottky junction [95]. In detail, according to Schottky theory, the following equation has been considered:

$$\frac{1}{C^2} = \frac{2(\Phi_{bi} - V_a)}{q\varepsilon N_d} \tag{4.1}$$

where Φ_{bi} is the built-in voltage, V_a is the voltage applied from the metal and the semiconductor , q the electron charge, ε the dielectric constant and N_d the density of donors. As it possible to observe, $1/C^2$ increases moving toward larger biases applied, which according to the above equation, should correspond to $V_a < 0$, i.e. a negative voltage drop between the metallic electrode and KNN. In our structure, this condition applies only to the bottom KNN/Pt(111) interface, thus pointing towards the fact that the rectifying behavior is determined by the bottom interface. In figure 4.10, we report a sketch of a qualitative band diagram in KNN microcapacitors for zero applied bias which is consistent with our measurements. KNN is a dielectric ceramic and there is very little quantitative data on its behavior as a “wide-gap semiconductor” (E_{gap} = 3.54 eV [96]).

However, it is well known that KNN is highly prone to n-type or p-type doping by oxygen vacancies and alkaline vacancies, respectively, which typically originate during deposition and processing. As reported in literature KNN is tipically considered to be n-type doped due to oxygen vacancies [91], [97]. The qualitative band alignment depicted in fig. 4.10 is obtained assuming a n-type doping, which is coherent with the fact that the overall scenario from our experimental data can be explained in terms of creation of oxygen va-

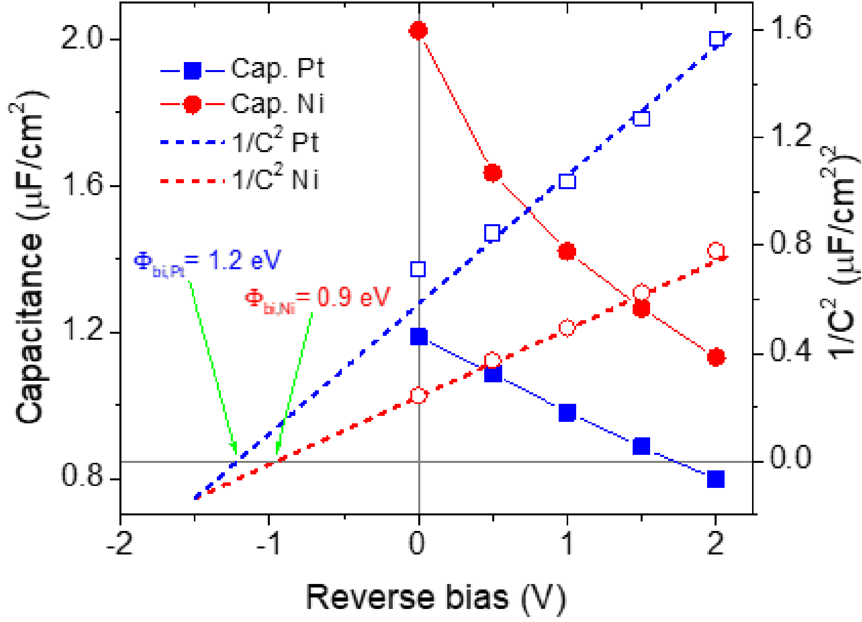

Figure 4.9: Graph of the capacitance and $1/C^2$ versus voltage as used in the model of a Schottky-semiconductor diode interface [95]. From [90].

cancies due the scavenging action by metals deposited on KNN. At the bottom interface, due to the large work function of Pt ($\Psi_{Pt} \sim 5.65$ eV) compared to the sum of the KNN energy gap ($E_{gap} = 3.54$ eV) and electron affinity ($\chi_{KNN} \sim 1.1$ eV similarly to other niobates [87]), we expect an electron flow from KNN to Pt, leading to an upwards band bending and subsequent space charge accumulation due to oxygen vacancies acting as point defect donors. The precise entity of the Schottky barrier height (Φ_B) and built-in potential (ϕ_{bi}) cannot be determined using the simple Schottky model ($\Phi_B = \Psi_{Pt} - \chi$, $\phi_{bi} = \Phi_B - E_C + E_F$) due the well-known phenomenon of Fermi level pinning by interfacial states. Whatever their values, however, the relevant point here is that a Schottky barrier like that depicted in the band figure is expected at the bottom interface. At the top interface we expect a similar situation, this even though the work function decreases among the series of electrodes employed ($\Psi_{Pt} > \Psi_{Ni} > \Psi_{Cr} > \Psi_{Ti}$ - table 4.2) so that different barriers height can arise. From this picture, it clearly turns out that for a perfectly symmetric capacitor (like in the case of Pt/KNN/Pt) there would be two counteracting rectifying barriers giving rise to a symmetric high impedance behavior. The experimental asymmetric density of current versus field curves instead indicate that only one of the two junctions determines the effective rectifying behavior. As the experimental low impedance (high current) state is for negative bias from the band diagram of figure 4.10, it turns out

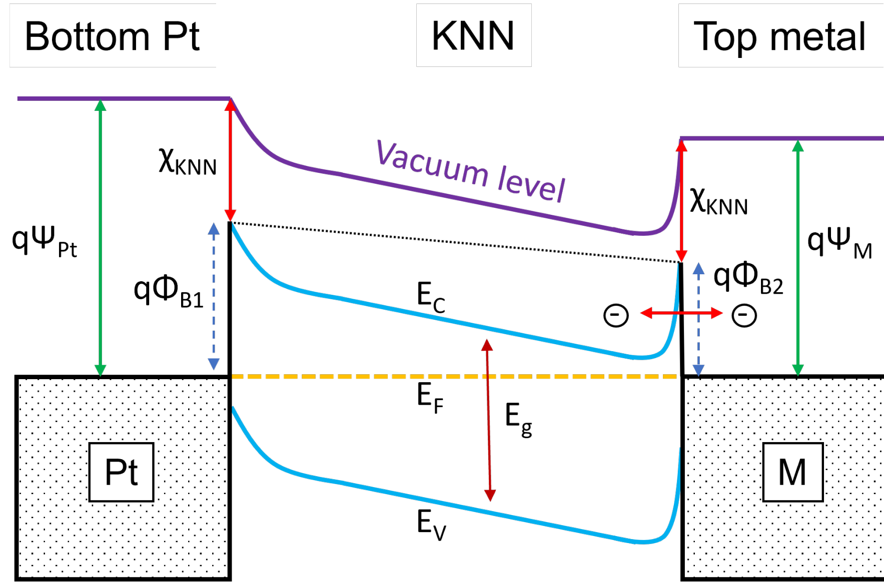

Figure 4.10: Qualitative band-structure scheme for the metal-semiconductor-metal stack (platinum-KNN-top metal) at zero bias. From [90].

that in this condition the top junction is in reverse mode while the bottom one is in the forward mode. This means that the net rectifying behavior of the MIM device is mainly determined by the bottom junction, between KNN and the Pt(111) template, which is indeed the common contact for all investigated devices, all showing the same polarity of the conduction asymmetry. The reason why the top barrier is much less influent, displaying a sort of ohmic behavior, cannot be just related to the different work-function of the metal pads, as the more pronounced rectifying behavior is found in case of a symmetric Pt/KNN/Pt capacitor. Another idea can come from the reactivity of the metals deposited on KNN to realize the top contacts. As a matter of fact, Secondary Ion Mass Spectroscopy measurements done in previous works [20] have revealed a sizable interfacial oxidation of Ti, Ni and Cr overlayers, which is expected to be associated to a high concentration of oxygen vacancies in the KNN film underneath by oxygen scavenging. This can produce a local heavy doping inducing a thinning of the barrier and almost ohmic transport across it due to tunneling, in analogy with ohmic contacts used in semiconductor technology. Other sources of doping could be the interdiffusion of metals inside the KNN through morphological defects [98] possibly leading also to direct conductive paths. While this could be evident for highly reactive materials like Ti and Cr, the case of Pt seems questionable. However, it is well known that during the deposition of Pt on oxides, highly reactive nanoparticles can be formed [99], ultimately leading to sizable energy scavenging at the top interface while at the bottom one, originating by the growth of KNN onto a flat Pt(111) surface, the reduced Pt reactivity can definitely lead to a much lower oxygen

vacancy concentration and thus preserve the rectifying behavior of the junction. From the analysis of our experimental results, the simplified concentrated parameters model of figure 4.7b emerges, with a diode representing the rectifying bottom interface, a complex impedance describing the bulk KNN behavior, and a resistor which represents the “ohmic behavior “ of the top contact. With reference to this model, we can qualitatively explain the $J-E$ curves of the figures where the mean leakage is presented; in particular the one represented in figure 4.7a. For small bias an almost ohmic behavior is found in case of Ti and Cr electrodes. As a matter of fact, the equivalent resistivities for positive and negative bias (ρ_+ and ρ_+) estimated from a linear fit of the $J-E$ curves from 0 to ± 5 kV/cm from the minimum, are essentially the same (see table 4.3). This is not always true for Pt and Ni. In half of the investigated devices we found a more ohmic, but still asymmetric, behavior like that of Cr and Ti, even though the resistivity is higher, while for the rest of devices (like those giving the $J-E$ curves in figure 4.7a) the more pronounced rectifying behavior reflects in a sizable small-bias asymmetry so that a linear fit for positive bias is not meaningful, as expected for a true diode in series with a resistance. The fact that for Cr and Ti the equivalent resistivities are much smaller than for Pt and Ti is in agreement with the higher concentration of oxygen vacancies due to oxygen scavenging for the latter electrodes, or to the tendency of Ti and Cr to diffuse into the KNN films [98]. Moving towards larger positive bias (in reverse mode for the diode at the bottom interface), we enter a region of the graph where the leakage current is limited by the bottom interface in reverse bias and a plateau appears for Pt and Ni. This is the region where small signal capacitance measurements have been carried out, confirming the presence of a space-charge region. By further increasing the voltage, we assist to a remarkable increase of the leakage current which could be associated to a sort of breakdown of the bottom junction, due to the activation of additional conduction processes. For Ti and Cr, we do not see a plateau at low voltages, most probably because of the higher reactivity of Ti and Cr giving rise to high leakage also at small positive bias. We should also mention that also for some Pt and Ni pads we did not find a plateau but just a less pronounced curve like those measured for Ti and Cr with less current density. Indeed, it has been reported that, apart from creation of oxygen vacancies at the interface, other effects can arise. Titanium can diffuse through grain boundaries of KNN to the full thickness of KNN and produce oxygen vacancies deep within the insulator [98]. It is also very likely that different surface states appear at the bottom KNN-Pt interface depending on the choice of the top electrode material, thus altering the barrier height by Fermi level pinning and affecting the rectifying behavior [88]. The enthalpies of formation of oxides of Pt, Ni, Ti, and Cr are -80, -240, -945, and -1128 kJ/mol at standard conditions. Therefore, it is expected that Cr and Ti can more easily scavenge oxygen from KNN at the top interface to form the corresponding

	Pt	Ni	Ti	Cr
ε_r	6.25	1.10	1.06	7.32
ρ^+ $(\Omega \cdot cm)$	/	/	$8 \cdot 10^5$	$8 \cdot 10^4$
ρ^- $(\Omega \cdot cm)$	$8.8 \cdot 10^8$	$5.6 \cdot 10^8$	$7 \cdot 10^5$	$8 \cdot 10^4$

Table 4.3: Estimated dielectric constant using the Poole-Frenkel model and resistivities. For the latter values are extracted near the minimum of the leakage current; due to the huge rectification effect provided by Ni and Pt the estimation of ρ^+ would have lead to a non realistic estimate. (From [90]).

oxides. For Ni and Pt, the oxidation process is energetically less favorable, but the higher reactivity of nanoparticles formed at the early stage of the growth of metals on oxides is expected to produce oxygen vacancies in the topmost KNN layers, in analogy with what has been observed for other noble metal/perovskite interfaces, with concentration high enough to generate a local heavy doping [99]. On the other hand, the sizable difference in the enthalpies of formation is expected to reflect in a marked difference in the bulk doping of the KNN film by oxygen vacancies which is connected to the intrinsic leakage. This is clear looking at the absolute values of the leakage currents reported in figures 4.6 and 4.7a, which are definitely lower for Pt and Ni than for Ti and Cr, both for positive and negative bias. Coming back to our concentrated parameters model, applying a negative voltage at the top contact the bottom junction is in the forward mode, so that the applied voltage effectively drops across the KNN film and we assist to a steeply current growth reflecting the intrinsic leakage mechanisms within the bulk of the film. For larger negative values of the applied voltage, we see a reduction of slope indicating that another phenomenon is limiting the leakage current. In the theory of metal-insulator interfaces, Schottky and Poole-Frenkel emission models are frequently used to interpret the reverse bias regime for high applied voltages [100], [101]. The first is an electrode-limited conduction mechanism in which the most important limiting factor is the work-function of the metal used, determining the effective barrier to be overcome to inject electrons from the metal into the insulator. The second is a bulk-limited conduction mechanism describing how electrons (or mobile negatively charged defects) are emitted from traps in the dielectric thanks to a field-induced reduction of their potential barrier. Both have more relevance at high applied electric fields and increasing temperatures, where excitation of charges is more energetic [40]. In our case, as we are dealing with films with thickness (300 nm) larger than the electron mean free path, both effects are expected to play a role. Evaluation of Schottky emission can be done by plotting $\ln(J)$ vs. $\sqrt{E}$, while emission by Poole-Frenkel can be tested by a plot of $\ln(J/E)$ vs. $\sqrt{E}$ [40], [101]. In such plots, evidence of linear behavior at high voltages (confirming the model proposed) is evaluated and the slope of

the line contains a value for the optical dielectric constant of the insulator. From the density current equations (eq. 4.2 and eq. 4.3 for Schottky and Poole-Frenkel emission, respectively) is in fact possible to retrieve the value of the optical dielectric constant using a linear fitting. For the Schottky conduction method we have:

$$J = A^{*}T^{2}\exp\left[\frac{-q(\phi_B - \sqrt{qE/4\pi\varepsilon_r\varepsilon_0})}{kT}\right] \tag{4.2}$$

where the effective Richardson constant is defined as:

$$A^{*} = \frac{4\pi q k^{2} m^{*}}{h^{3}} = \frac{120m^{*}}{m_0}$$

While for the Poole-Frenkel mechanism the current density can be defined as:

$$J = q\mu N_C E\exp\left[\frac{-q(\phi_T - \sqrt{qE/\pi\varepsilon_r\varepsilon_0})}{kT}\right] \tag{4.3}$$

In those equations we find different parameters, m_0 is the free electron mass while m^{*} is the effective electron mass in the dielectric. T is the absolute temperature, q is the electron charge, $q\phi_B$ is the Schottky barrier height (i.e. conduction band offset), E is the electric field across the dielectric, k is the Boltzmann's constant, h is the Planck's constant, ε_0 is the permittivity in vacuum and ε_r is the optical dielectric constant. Additional parameters for the Poole-Frenkel conduction method are μ the electronic drift mobility, N_C the effective density of states in the conduction band and $q\phi_T$ is the energy level of the traps. In figure 4.11 is possible to see both mechanism in action using a band diagram. Evaluation of the dielectric constant of the KNN film can be made using a linear fitting for the proposed models; but firstly is it possible to express it mathematically from the equation of the current density. From equation 4.2 is it possible to retrieve the optical dielectric constant for Schottky conduction method:

$$\varepsilon_r = \left(\frac{q\sqrt{q}}{mk_BT\sqrt{4\pi\varepsilon_0}}\right)^{2} \tag{4.4}$$

Analogously from the equation for the density of current in the Poole-Frenkel model:

$$\varepsilon_r = \left(\frac{q\sqrt{q}}{mk_BT\sqrt{\pi\varepsilon_0}}\right)^{2} \tag{4.5}$$

Where m is the corresponding slope of the Schottky or Poole-Frenkel plots. In the forward regime for the diode (negative bias applied) both conduction models such as the Schottky one with the introduction of the effect of bulk traps and the pure Poole-Frenkel one predicts a linear behavior according to the theory. Fittings for the models were made in forward bias, thus avoiding the diode and only considering the KNN and the top contact resistances. For most of measurements on different pads, we found a linear behavior as predicted by the model, especially for Pt, and Ni thus confirming that at higher negative voltages Schottky emission at the top electrode and Poole-Frenkel emission could be the main phenomena limiting the leakage current at high negative bias (as it possible to see in figures 4.6 and 4.7; in particular in the first figure for very high applied fields $E < 150$ kV/cm the leakage do not change for the Pt pads, indeed a plateau is reached). However, the extraction of physical quantities like the dielectric constant and the effective barrier height from this kind of analysis is prevented due to the huge variability of experimental results which can be understood if one considers that a sizable fraction of current is localized at crystal edges, with random distribution under different metallic contacts. Still an effort was made using both the fitting and the dielectric constant formulas (equations 4.4 and 4.5). Values are reported in table 4.3. In particular the ε_r numbers reported are extracted from the Poole-Frenkel fitting as for the Schottky fitting no physically

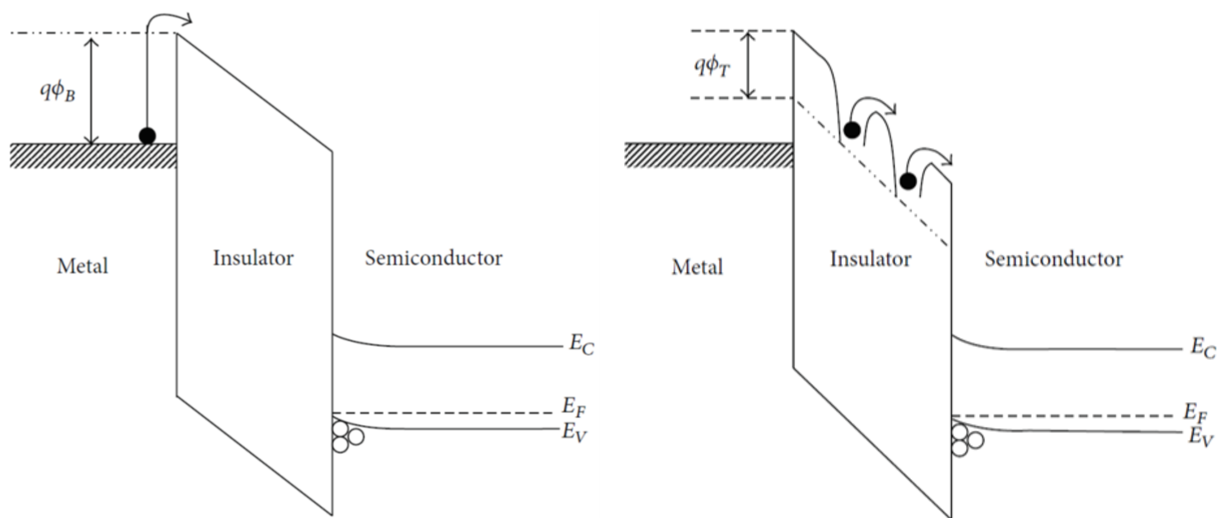

(a) Schematic energy band diagram of Schottky emission in metal-insulator-semiconductor structure.

(b) Schematic energy band diagram of Poole-Frenkel emission in metal-insulator-semiconductor structure. The application of an external electric field can influence the current intensity, increasing the probability of a thermal emission of an electron from a trap state.

Figure 4.11: Schematic energy band for the Schottky and Poole-Frenkel conduction method (from [101]).

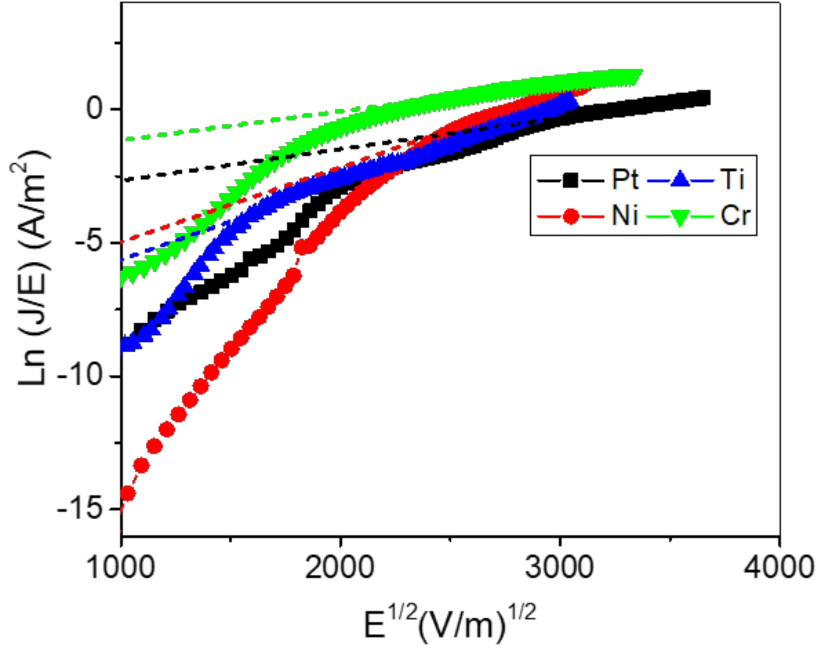

Figure 4.12: A fitting of $\ln(J/E)$ vs. $\sqrt{E}$ for fitting of Poole-Frenkel emission due to traps in KNN for forward bias (negative applied voltage).

meaningful dielectric constant were found for KNN; in fact values extracted were always less than a unity. Is it possible to see the linear fitting for the Poole-Frenkel method from which values for the dielectric constant were extracted in figure 4.12. From a practical perspective, if KNN wants to be used as a ferroelectric, it should be highly insulating and make an ohmic contact with bottom and top electrodes, but without significant semiconducting depletion regions. In such case, the electrode-KNN interface will allow for balancing charges to counteract the permanent polarization of the ferroelectric. The conduction will be bulk-limited by KNN and, if properly insulating, low leakage will be ensured [81], [102]. Nevertheless, another kind of ohmic contact is possible, but it needs to be avoided. If the insulator is doped significantly at the interface, it will behave as a semiconductor and establish a depletion region with the electrodes, with a corresponding built-in-bias. Thus, a metal-semiconductor diode interface forms, which establishes a space-charge region with considerable capacitance. If doping is increased even further, the depletion region becomes very thin and tunneling through it can become the most important conduction mechanism (top electrode in the present study). In this case, an ohmic contact is also established [103]. Nonetheless, the doping also affects the bulk of the insulator, which transforms it to a more conducting material. In this scenario, the effective electric field across the ferroelectric will not be uniform, switching will be

ineffective, and leakage high. All in all, considering the effect of doping, if it is minimal, the depletion region is not of much importance, as it does not produce a significant capacitance. When doping becomes substantial, a rectifying behavior appears due to a smaller depletion region, which causes a measurable capacitance, a potential drop, and ineffective ferroelectric switching. Overall, our results point to the need of minimizing such rectifying barriers by interface engineering in order to avoid the asymmetric operation of the piezo material.

4.3. Conclusions and suggestions for improvement

In conclusion, the mechanisms leading to asymmetric leakage currents in Metal/KNN/Pt(111) microcapacitors is interpreted as the result of the creation of the oxygen vacancies which can naturally spawn due to the scavenging of oxygen by the metal pads deposited on the top of KNN to create the top contacts. For all metals used as top electrode, we found a rectifying behavior with leakage currents for negative top-bottom voltage much higher than for negative bias. The asymmetry was more dramatic for Pt and Ni, while for Ti and Cr a more symmetric ohmic behavior was found. This behavior is found both in macroscopic measurements on micro-capacitors and from local conductive AFM measurements. This asymmetry is explained by the presence of a rectifying Schottky-like junction at the bottom interface between the KNN film and the Pt(111) substrate, as confirmed by small signal capacitance measurements which are consistent with space charge accumulation at the same interface. Noteworthy, the rectifying behavior is more pronounced in materially Pt/KNN/Pt capacitors, thus pointing out that the origin of the asymmetry cannot be purely ascribed to the different work functions of top and bottom electrodes. Instead leakage current increases with the chemical reactivity of the electrodes (Ti $>$ Cr $>$ Ni $>$ Pt), following the enthalpies of formation of related oxides. Thus, the main driving mechanism could be connected to the oxygen insufficiency during the deposition of KNN and with the subsequent creation of oxygen vacancies by scavenging of top metals thus creating electron donors. This gives rise to the creation of “ohmic contacts” at the top interface, to an increase of the bulk KNN conductivity, and a decrease of the overall asymmetry, due to oxygen vacancies diffusion towards the bottom electrode and consequent reduction of the rectifying action of the Schottky barrier, with larger impact for the more reactive electrodes (Ti and Cr). This can also suggests that the usage of direct metallic contacts should be avoided in any case. Not by chance, commercial KNN with good leakage properties has a thin oxide layer before the top contact [104]. The potential impact of this asymmetric leakage on the ferroelectric switching and bipolar piezo operation is discussed, pointing to the need of minimizing asymmetric potential barriers at the

top and bottom interfaces to reach a symmetric operation of the piezo-material. Based on literature to dope the PLD target with some atomic species able to compensate the oxygen vacancies, such as Mn is a highly recommended suggestion [105], [106]. We also have to take into account how to reduce the alkali loss as they have also found out to be an important defect causing high leakage. Other techniques to reduce the alkali loss in KNN can be given by exploring the temperatures of the process.

5 | Rapid Thermal Annealing

Rapid Thermal Annealing (RTA) process is a processing technique that has been explored in the past and is a useful crystallization resource for thin films, including ceramics. For example PZT has been found to be capable to crystallize using RTA and under certain conditions even in a well ordered orientation where morphology, structural and ferroelectric properties are able to improve using such technique [107], [108]. The research in this direction was initially proposed to trying to solve the problem of the limited temperature work-range of the sputtering machine that has a top limit of 400°C (Evatec Clusterline [109]). This new installed sputtering machine could in principle help with the realization of many samples in just a deposition step as in fact the KNN is being deposited directly on the substrate (wafer diameter $\sim$ 300mm) and only after the growth could be cut in many different samples (even with different measures). This can reduce a lot the working time with respect to PLD increasing the number of samples that can be analyzed and characterized, in principle from a 300mm wafer is possible to obtain hundreds of 10x10mm^2 KNN films. That is why RTA process is so important to study for KNN; if we can demonstrate that is possible to obtain good KNN crystalline films in this way is it possible to improve the process and characterize more the obtained films. After the low temperature growth (more details on the whole PLD process can be found in section 2.1), instead of being annealed in oxygen atmosphere (0.5 atm) at a fixed temperature ($\sim$ 550°C) for 30min a rapid thermal annealing was performed. Annealing is performed by fixing a rise up ramp of around 20°C/s then to hold the selected temperature for 60s seconds and just after that to let the film cool down for an arbitrary amount of time, more details on the machine used can be found at chapter 2. The film is then characterized to see the morphology, current leakage and stoichiometry.

We are now going to explore what Rapid Thermal Annealing technique has been able to produce. All of this work was motivated by a good first result obtained at the beginning of this new process technique. Despite the not so constant results in terms of leakage, RTA processed films were still able to crystallize (still without a preferential phase through the film), also stoichiometric ratios were found to be close to the one of the

target making RTA processed films in principle valid alternative to the classic standard grown films.

5.1. Preliminary results

In this first section we are going to discuss the main differences between the films that, later in the text will be referred as the reference ones; in particular, we are going to compare a classic PLD growth film versus a RTA processed film. The classic PLD deposited films - the film that has followed a *nominal condition* growth - has a thickness of 300nm while the RTA processed film have a thickness of 220nm only even if the deposition time was the same. This can be reconducted due to the fact that the growth rate is temperature dependant, depositing at a lower temperature gives a slower growth rate; in fact the RTA film has been deposited at a temperature of 400°C while the nominal condition growth one has been deposited at 615°C [110] (for further details about the PLD and processes see chapter 2). The RTA sample after the growth has been annealed in normal atmosphere for 60s at 700°C with a ramp of 17°C/s. Since both films shows at first impression good properties and measurements were reproducible, they can be directly comparable under various aspects.

5.1.1. Crystallographic orientation

A series of X-rays crystallographic measurements (XRD) has been performed on those two sample plus another sample grown at low temperature but without the RTA step. The energy used for those $\theta - 2\theta$ diffraction experiments is the one of Copper $K\alpha$ (8.04keV), all the measurements were taken at room temperature. Also a double monochromator slit was used. With the obtained diffractogram is possible to understand quantitatively the orientation of the deposited film; in fact different peaks indicate different orientation of the crystals. Taking as reference the previous works, is it possible to confirm that the film that has followed a classic PLD process shows the same diffractogram [21], [20] (fig. 5.1). This can be a confirmation that first of all the classic process is repeatable and the obtained sample is valid. Peaks showing a defined crystallization can be found in all the diffractograms. The non annealed one shows only the peak associated to the oriented (111) Platinum substrate [111]. Since at room temperature the KNN (for almost every Na percentage) is orthorombic, the peaks at 22.5° and 45° can be associated respectively to KNN(001)/(100) and KNN(002)/(200) planes, while the peak around 33° is linked to the rod-shaped KNN(011) crystallites (that are clearly visible in fig. 5.3) [20], [112], [113], [114]. In principle other peaks associated to the KNN (such as the KNN(111)

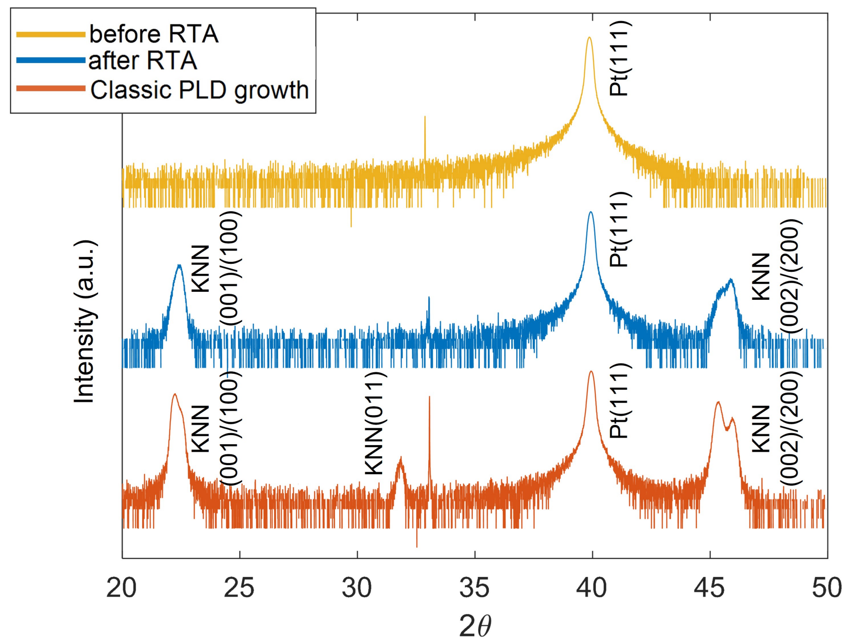

Figure 5.1: XRD measured diffraction pattern of the KNN film. Peaks indicate the different orientations of the KNN film or the Platinum substrate. The graph is in a semilogarithmic scale.

tetrahedron-shaped) should be present in this diffractogram, however they are absent since their quantity in the film is much more less with respect to KNN(100) crystals; it would be possible to exploit those peaks in a powder diffraction [115]. By observing the obtained diffractogram in a linear scale is possible to measure the peak height and since it is directly associated to the quantity of orientated crystal is possible to estimate the relative weight of all the crystal orientation present or at least understand which is the most common orientation for the film. For example by looking at fig. 5.2 is possible to observe a fit of the diffractogram of the classic PLD process. By looking at the intensity and the area of the peaks the film has a preferential orientation which is the (001) for the sample that has followed a classic growth, while it is not the case for the RTA sample. In fact, in the classic PLD growth sample, the ratio between the (001) and the (100) peaks is 2.5 confirming the predominant (001) orientation (also known as polarization out of plane). While for the RTA film the rateo is 0.8, thus showing that the two orientation are present almost in a equal proportion, confirming that no preferential orientation is found in the film.

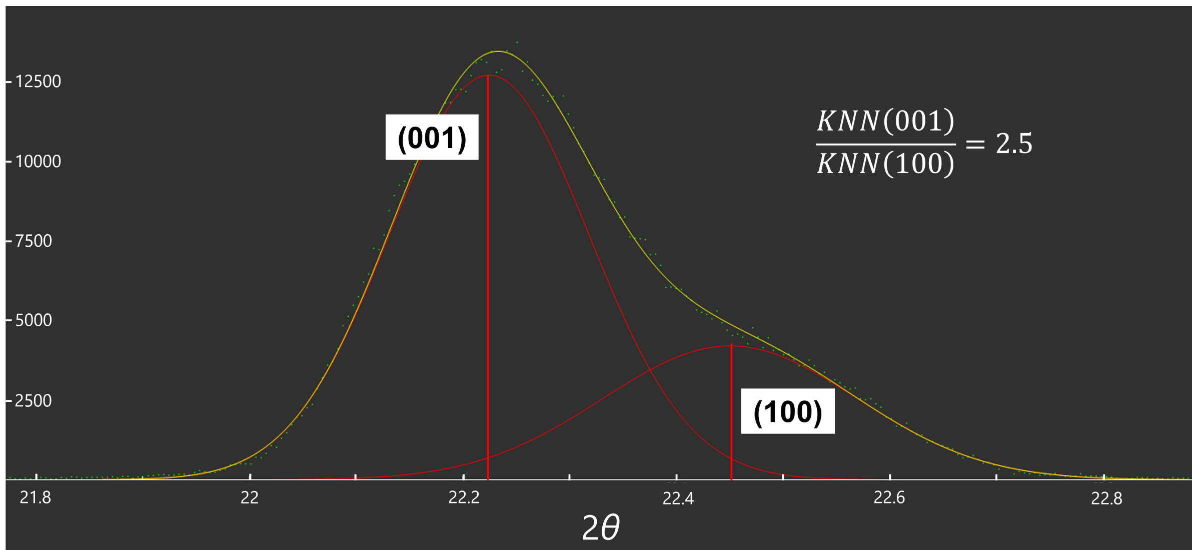

(a) Classic PLD growth

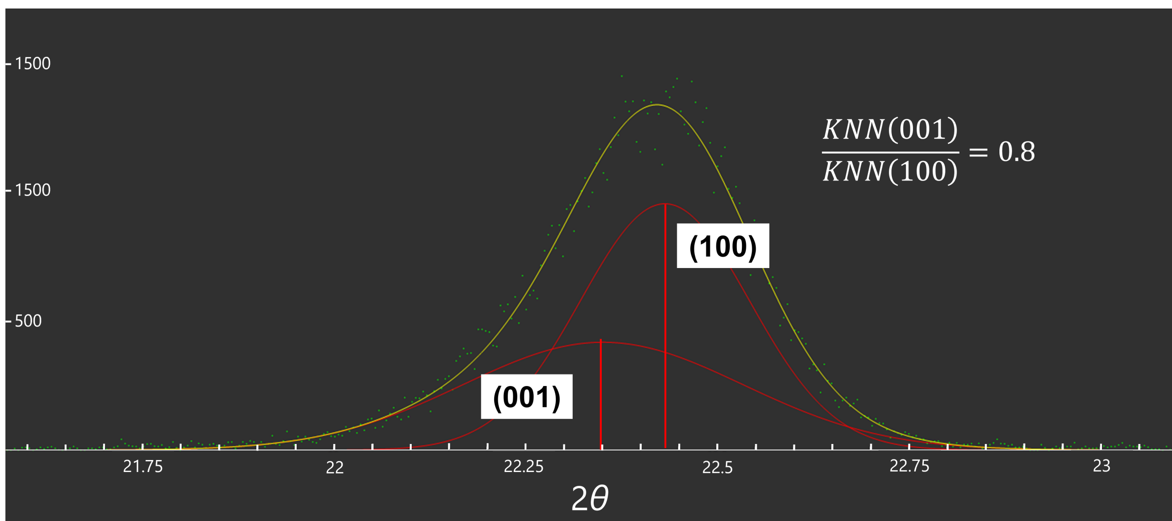

(b) RTA film

Figure 5.2: Fitting of the XRD diffractograms of the classic PLD growth and RTA processed film. The peaks are fitted using a gaussian function through the software Fityk [116].

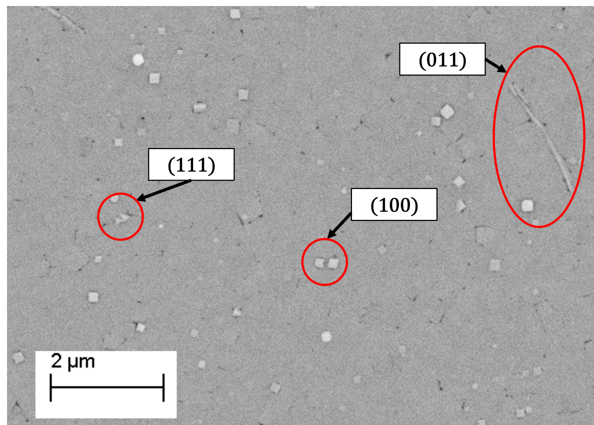

(a) Classic PLD growth - here it is possible to observe different crystal orientations [21]. Image taken using secondary emitted electrons.

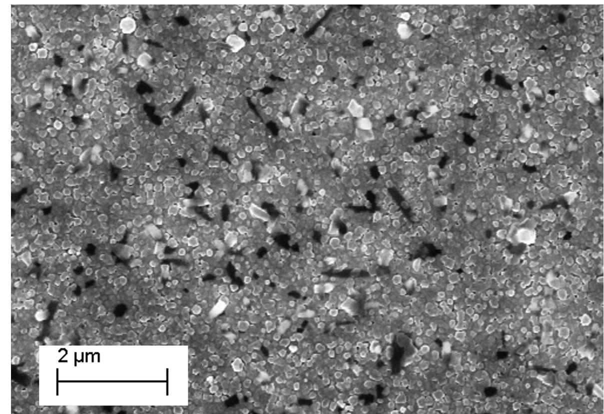

(b) RTA film

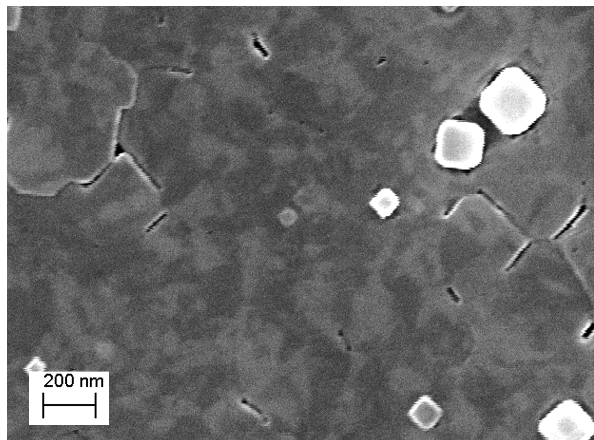

(c) Classic PLD growth

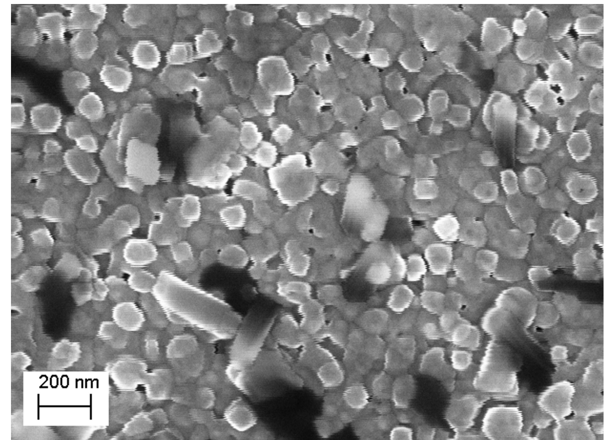

(d) RTA film

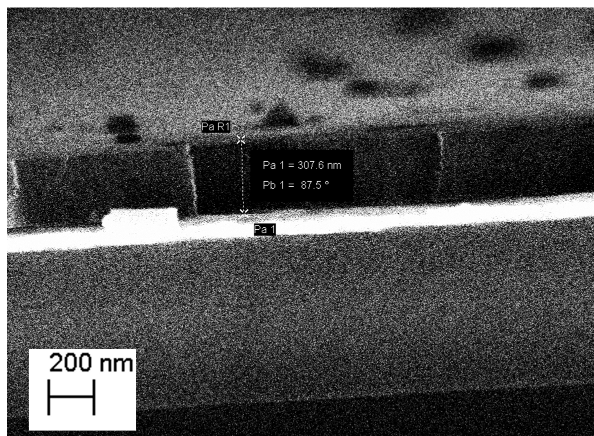

(e) Classic PLD growth cross section (thickness ∼ 300 nm)

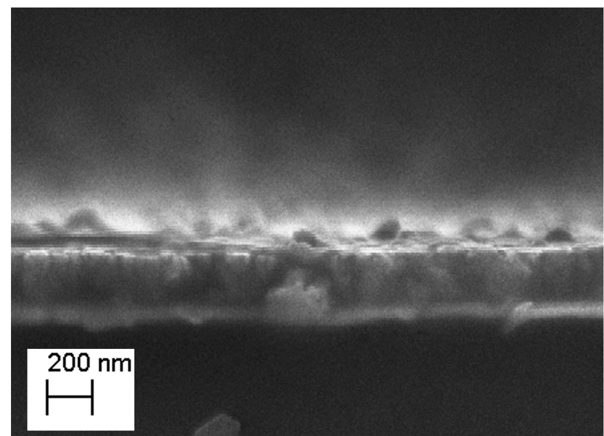

(f) RTA film cross section (thickness ∼ 220 nm)

Figure 5.3: SEM images of the two films.

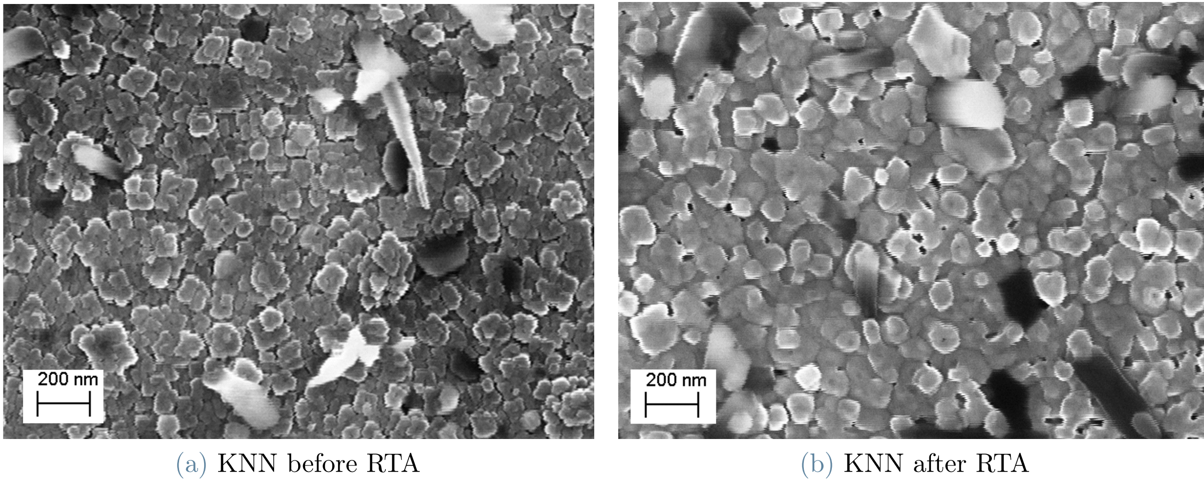

(a) KNN before RTA (b) KNN after RTA

Figure 5.4: KNN morphology comparison before and after RTA

5.1.2. Morphology

A morphological characterization has been performed with scanning electron microscope to evaluate the quality of the obtained surface for the RTA sample and compare it to the surface of the classic PLD growth sample. Images are taken using an electron source accelerated at 10kV. Sometimes, images are taken using secondary emitted electrons since they are more sensible to the local topography [117]. A representative portion of each sample is being shown in fig. 5.3. By visual inspection of the top view and the cross section, it is clear that the two films are very different; in particular, the RTA films shows a grainy and not compact texture compared to the classic PLD growth film. This particular texture of the RTA film can also suggest that both crystal orientations are present in the same quantity, thus the film seems not able to configure into one predominant crystal orientation. This is more evident by looking at the cross section images, where is it possible to appreciate the compactness of the classic PLD growth film. Another interesting feature emerging from SEM images is related to the black and white textures that appear on the surface of the sample, in particular to the classic PLD growth. In figure 5.3 a collection of SEM images is shown to. As reported in literature, this texture can be related to the material's spontaneous ferroelectric domains [74], [75]. It would be possible to take more advanced measurements to study the ferroelectric domains through Piezoelectric Force Microscopy (PFM), but this characterization is beyond the goal of this work. In SEM images the dark zones correspond to an orientation of a certain domain polarization while lighter areas shows the opposite orientation of polarization [76]. This effect is also promoted by the presence of (001) orientation of the film that leads to a spontaneous polarization that is perpendicular to the film surface [20], [77]. Defined polarized domains

are not visible in the RTA sample probably due to the defined crystal phase through the film. Last but not least, the RTA process has not changed that much the topography of the film before the annealing; even before the rapid thermal annealing, the film was showing a grainy structure as can be seen in fig. 5.4. Even though the films appear to carry a high density of defects with respect to the classic PLD growth films, the fact that it does not change its appearance after the rapid annealing is a promising result; in fact, is commonly reported in literature that the presence of inhomogeneity though the film and the spike annealing can cause the film to spawn big defects (such as cracks along the film) due to the high thermal stress, However this is not the case [118], [119].

5.1.3. Film stoichiometry

One major challenge for depositing high-quality KNN-based thin films is the volatilization of light elements, such as potassium and sodium, during the films growth process, which causes a stoichiometry deviation of the resulting films, [120], [81], [75]. This problem has been explored in literature even considering other deposition techniques such as RF sputtering, where the divergence in stoichiometry was usually solved using a deposition target with Na and K excess to prevent their evaporation loss during the sputtering process [121], [122]. Another way to try to restore the proper stoichiometry to the film was to post anneal the film in a alkaline atmosphere [123]. Our case is much different as we only post anneal the film using the RTA process and so we anneal for a short time with a high temperature gradient. EDX analysis was conducted considering different 1x1mm^2 sections of the film and for each section 4 measures were taken, the reported value is the mean value between them. The beam energy for the analysis is fixed at 10kV as the depth resolution is enough to probe the deposited material. In particular the three elements composing KNN and their reciprocal ratios were studied: potassium (K), niobium (Nb), and sodium (Na). The presence of oxygen was measured too, but since EDX measures were performed ex-situ, the exposition to the normal atmosphere alters the observed presence of oxygen in the film, making it non representative for the film. Taking as a reference the previous research done using a classic PLD deposition technique [20], [21] is it possible to observe how the RTA was able to improve the stoichiometric ratios of the light elements (table

	Classic PLD growth	RTA	Δ%
Na/Nb	0.45	0.50	+12%
K/Nb	0.41	0.43	+8%
K/Na	0.92	0.83	-9%

Table 5.1: Stoichiometry ratios comparison between the previous works [21], [20] and RTA

5.1). The ratio between the light elements and the niobium is higher if the film grows at a lower temperature and only after this step annealed at a higher temperature. This result is promising as one of the main goal of the PLD deposition technique is to obtain a nominal film stoichiometry of $K_{0.5}Na_{0.5}NbO_3$ as the alkali presence seems to inhibit the formation of alkaline ion vacancies which can lead to a higher current density leakage [79]. Apart from the stoichiometry difference between the classic PLD growth and the RTA annealed films, another considerable result is given by observing how little the RTA has impacted on the stoichiometry of the film before and after the RTA process. By looking at table 5.2, is possible to appreciate the small change in stoichiometry of the film. In particular the alkali presence is not much affected by the RTA process. This result is also explored in section 5.2.3, where the RTA process is compared to a classic PLD growth but using an overstoichiometric sample.

	before RTA	after RTA	Δ%
Na/Nb	0.52	0.50	-4%
K/Nb	0.45	0.43	-5%
K/Na	0.85	0.83	-3%

Table 5.2: Stoichiometric ratios comparison between pre and post RTA process

5.1.4. Electrical characterization

After the qualitative morphological analysis and the quantitative EDX measurements, an electrical characterization of the film is needed to comprehend the performances in terms of current leakage. This kind of measurement is a way to understand not only the insulating properties of this material, but also the piezoelectric performances [124]. The measurements were carried out using a top-bottom configuration where the tip that controls the voltage bias is always on the deposited pad, while the ground tip (that stays always at zero voltage) is touching the bottom platinum contact. As already discussed in chapter 4 choosing between different metals for the top contact is mandatory to obtain reproducible and coherent measurements; in this case Nickel has been chosen to be the top electrode material. Also top electrode metals have a different pad breakdown voltages; in fact contacts often break down (not only if the measure has been performed at a high field) but also measure after measure. This gave the impossibility to measure the leakage at higher fields (limiting the measurements to 150/200 kV/cm). Due to this, nickel, again, has been chosen since is able to sustain slightly higher fields with respect to other metals [21]. The leakage current through the Ni/KNN/Pt capacitor was measured at room temperature using a Manual Electric Probe System (more detail on the machine in

section 2.4.2). A pulsed stair-chase shape has been used as DC bias voltage (fig. 5.5), with 200ms span between each pulses, giving approximately a frequency of 50 Hz for the signal. Measurements on both films were repeated 5 times on a set of 5 different pads, the mean value is then calculated.

Current leakage

The current leakage of both samples has been measured and the comparison between the obtained result can be seen in fig. 5.6. As observed the leakage of the RTA processed film has the same asymmetric shape shape of the classic PLD growth (labeled as Nominal KNN), but its value is much lower, even two orders of magnitude lower. The fact that the two curves have the same asymmetric behavior can lead to think that the two films have the same rectifying properties that is given possibly by the oxygen vacancy barrier situated between the film and the bottom interface [40]; however, this conduction method mechanism is discussed in more detail in section 4, in this section only the value of leakage is considered.

5.1.5. Preliminary conclusions

This first RTA processed film could be a great point of start into modifying the process to let it be suitable for different growing methods (such as the RF sputtering) to increase the obtained sample size. Even though the film has a big defect density, it is able to show crystallization and a good leakage behavior. The major challenge now is to optimize the process in order to obtain a comparable morphology to the classic PLD grown film.

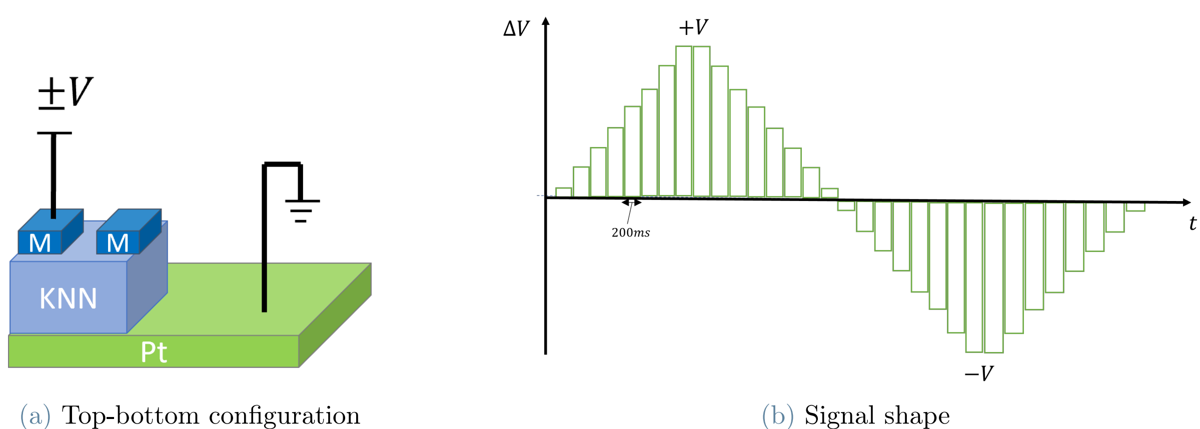

(a) Top-bottom configuration

(b) Signal shape

Figure 5.5: Signal shape and setup configuration for the current leakage measurements

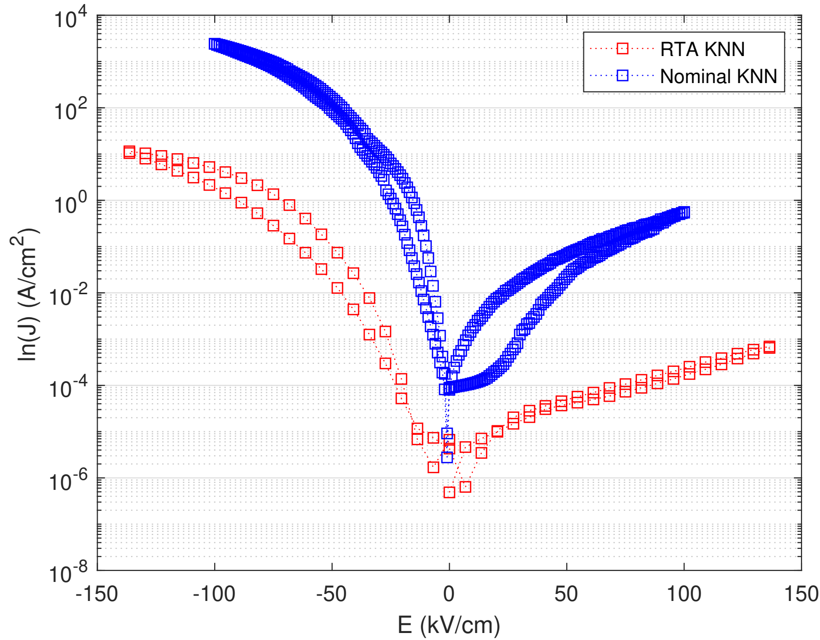

Figure 5.6: Top-bottom measurements (mean value) comparison between the classic PLD grown film (blue curve - here labeled as Nominal KNN) and tha RTA processed one (red curve). Both measurements are taken in the range $-3/+3\ V$ and in both case the top contact is made of Ni. The films have different thicknesses, the classic growth KNN is 300 nm, while the RTA one is 220 nm.

5.2. Effect of annealing temperature

After the first good result discussed in the previous section, we decided to try different RTA temperatures to see, firstly, if there is a threshold temperature for crystallization, and, secondly, to see the impact on the morphology of the film. In this case, samples are realized by depositing KNN at a low temperature (400°C). Then the 1 cm^2 squared film is cut into four different sub-samples to anneal them at different temperatures, in particular 550°C, 600°C, 650°C, 700°C. The rapid thermal annealing (RTA) process is slightly different with respect to the previous sample. In fact, the ramp is set to 20°C/s, then the temperature is held for 60s. Many samples were annealed, all at the same conditions, to check for reproducibility and improvement of the results. The reproducibility is present. However, the results obtained are not as good as the previously analyzed film, especially for the surface morphology and the current leak behavior. Still film were able to crystallize even at the lowest probed temperature. Sample after sample, different countermeasures were exploited to improve in particular the morphology of the film. It is worth saying from the beginning, that the surface of the samples was already dense in defects even before

the RTA treatment, thus the sample defectivity can only be attributed to the deposition process. In detail, to improve the film quality, we have deposited more material, changed the substrate and re-ablate the target but none of those methods have been successful. All the samples that are going to be shown through this section are going to be compared to the previously discussed RTA treated film, as it is going to be considered from now on the reference sample for all the subsequent RTA experiments.

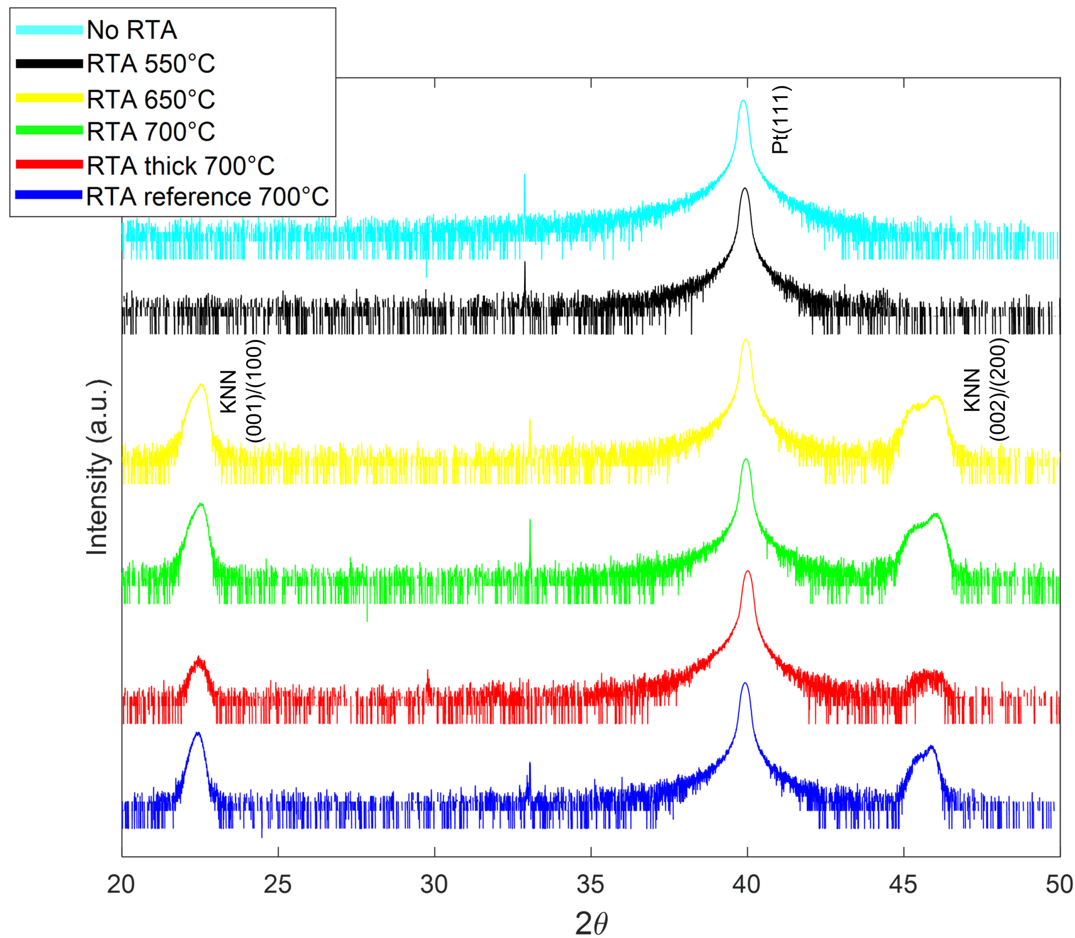

Figure 5.7: XRD diffractogram of a reduced group of sample. A further explanation for the legend is needed as we refer as "RTA thick" a sample with a higher deposition time (leading to a thicker film). Blue curve is the previously discussed RTA film

5.2.1. Crystallographic orientation

As already done before, a crystallographic characterization is performed to understand firstly if the crystallization of the material has taken place, and, secondly, if a defined phase exist through the film. As before, the energy used for these $\theta-2\theta$ diffraction experiments is $K\alpha$ (8.04keV) and all the diffractograms were taken at room temperature using a double

monochromator. All the obtained curves are compared graphically with the RTA film discussed in the previous section as can be seen in figure 5.7. In the figure, is clearly visible how the obtained films have the same crystallographic orientation apart for the film annealed at 550°C. As we can see, the peaks representing the two different orientation for the KNN, in particular the KNN(001) and the KNN(100) both situated between 20° and 25° 2θ value, are overlapping as already seen in the reference RTA sample (figure 5.2). This again is an evidence that we do not find a strong defined phase through the whole film. This collection of diffractograms can also give insight for the so called "crystallization threshold temperature". In fact, is possible to notice that the film annealed at 550° does not have the characteristic peaks associated to the KNN crystallization, but it shows only the strong Platinum (111) peak. The temperature threshold for the KNN crystallization then could lie between 550°C and 650°C. Of course by changing the annealing time to more than 60s, maybe the threshold temperature to obtain a crystal can become even lower than 550°C [125]. It is unclear if the fact that the KNN is not crystalline (and so can be considered in first approximation amorphous) leads to a lower conduction; in fact as can be seen in section 5.2.4 we obtain a lower current leakage for films annealed at 550°C. Temperatures of 800°C were already explored in previous research and proved to be able to crystallize [123]; in this sense, going down in annealing temperature could be an improvement for the process. One of the main goal after this first result could be to find the exact phase transition temperature and fine tuning it by changing other parameters such as the pressure, time and temperature.

5.2.2. Morphology

As already done for the previous film, a morphological qualitative characterization has been performed with scanning electron microscope to evaluate the quality of the surface for those samples. A direct comparison with the previous RTA sample is considered as for the RTA process it is considered a reference sample. Images are taken using an electron source with an energy of 10kV. Pre annealing images and small areas of each sample are shown in fig. 5.8. As it is possible to point out, even from this figure, films have a high concentration of "cracks" that are already present after the low temperature growth (and so cannot be attributed to the RTA process [118]). Many samples were made using the same conditions, but all the obtained films have the same morphology and so not all the SEM images for all the films are presented. The cracks expand through the whole film. By comparing the obtained film with the nominal RTA film (figure 5.3), it is evident that cracks are only found in this new sample. Since their appearance seems to be not dependant on the RTA process, we can only attribute this defectivity to the growing

process. Methods to trying to get rid of those defects are discussed in section 5.2.2. The presence of cracks seems to be the major cause of huge current leakage and sometimes even short circuits as they leave an easy access to the bottom pad (see section 5.2.4 for details). A detail of the cracks can be found in the figure 5.9, where the cross section of one of the obtained films (in particular the thicker one annealed at 700°C) is shown. Last but not least, as already cited before, the growth rate is lower with respect to the classic PLD deposition and this is always reconducted to the deposition temperature that afflicts the growth rate [110]. Obtained films are in the order of 200-220 nm thickness, and measurements were not straightforward as the films present a very high roughness among all the surface.

Possible solutions to improve the film quality

Since for the reference RTA sample and the first sample growth in the same condition the morphology obtained was so different, it is natural to think that the so called "point of work" of the machine could have changed at some point. In order words the process was still in control, but no more capable of producing the same film obtained as before. This conclusion is of course sustained by the many samples that we have grown after the reference RTA one. The reasons behind this abrupt change of morphology are still to be investigated since as a matter of fact all the countermeasures used to obtain films with no cracks have actually failed. Firstly, we have tried to change the substrate with a fresh new one since the quality of the substrate could have changed in time due to the continuous exposition to air and its quality has already been pointed out as a major cause of film defectivity [20]. Despite the change of substrate, no major improvement have been obtained, the film still presents cracks after the growing phase. The new substrate was provided by STMicrolectronics as the previous one. After swapping the substrate to a fresher one, but with no improvement, we have decided to ablate the KNN target for 3h in order to trying to get rid of a maybe not homogeneous zone of the target. The target ablation is basically a simulation of the deposition phase but with no sample inside the chamber. All this procedure takes place in vacuum. Since no improvements were found in this way, we have manually polished the target to remove a consistent portion of material before another ablation in vacuum. Still, no better films were produced after the procedure. Last but not least, we have deposited more material (increasing the deposition time to from 1h50min to 2h30min) to see if the cracks could have filled up with this extra material, but the only effect we have obtained is to have a thicker film with the same density of cracks as before (fig. 5.9) but with a quasi perfect stoichiometry (fig. **??**). In conclusion, we were not able to get rid of this morphology defects which seems also to be

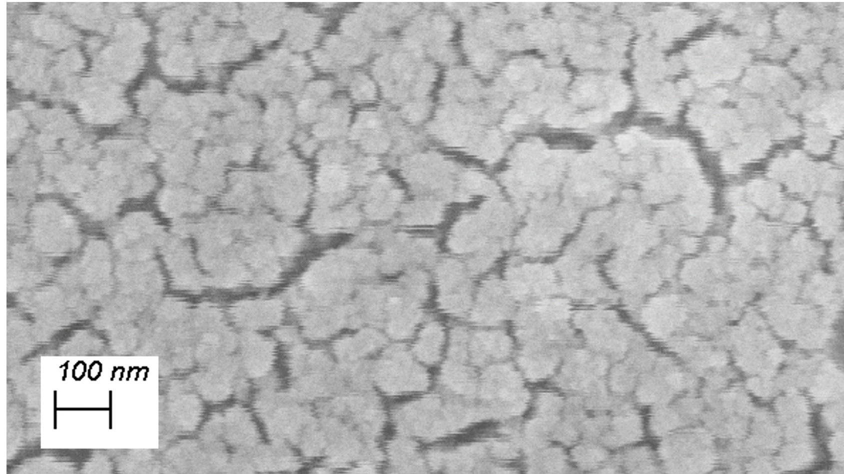

(a) Pre annealing surface. Cracks are already visible.

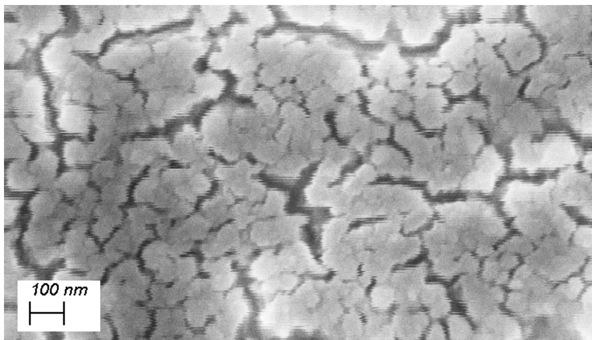

(b) After RTA at 550°C

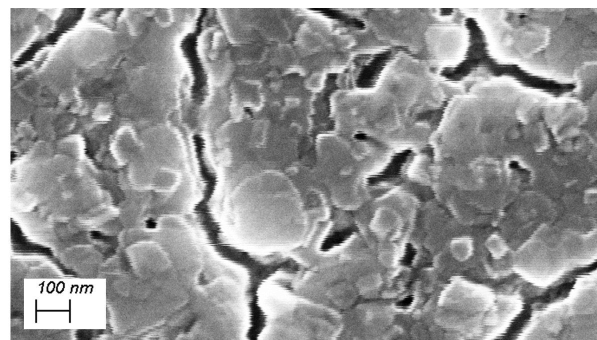

(c) After RTA at 600°C

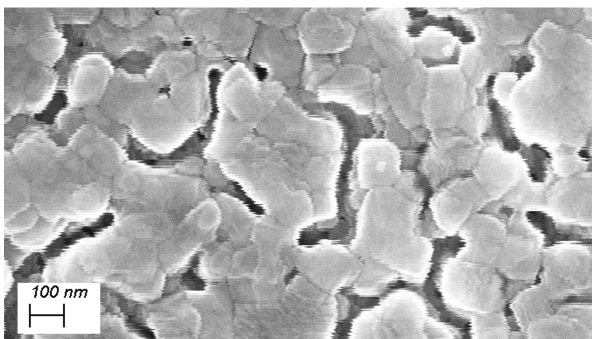

(d) After RTA at 650°C

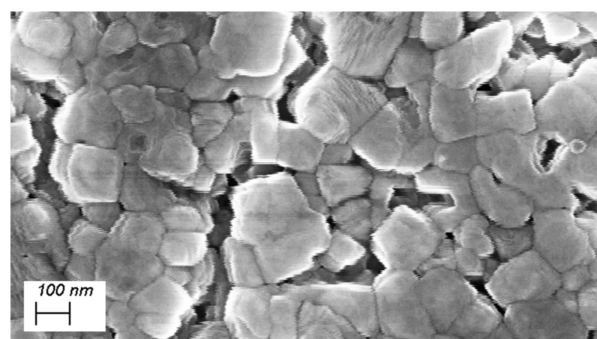

(e) After RTA at 700°C

Figure 5.8: SEM images of the samples. Pre and post RTA images are presented, is it possible to notice that all the surfaces are pretty similar but most importantly is straightforward to notice that cracks are not a product of the annealing.

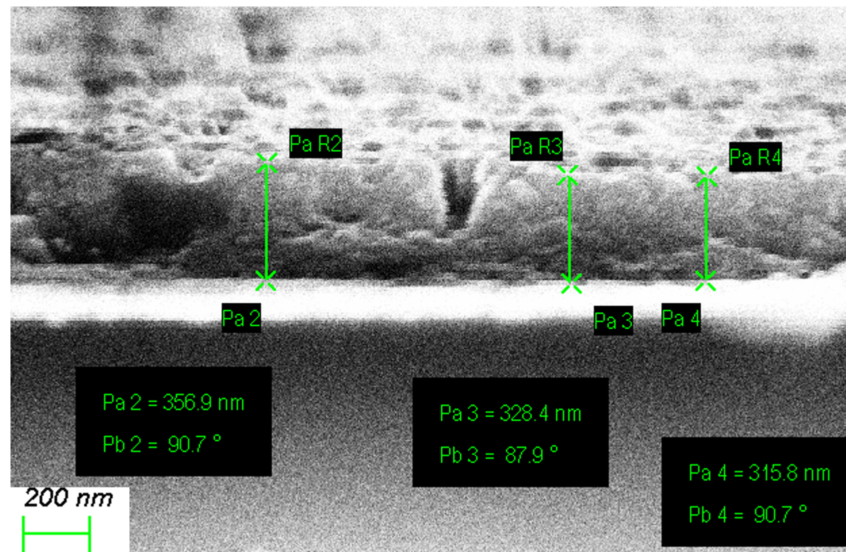

Figure 5.9: Cross section of a RTA film (with higher depositing time) annealed at 700°C; in particular is possible to see the detail of a crack and how this crack can actually lower the thickness of the whole film locally.

the main reason of a very high current leakage (see section 5.2.4).

5.2.3. Film stoichiometry

As already found out in the previous analysis for the RTA reference sample, the effect of the low temperature growing is to obtain a film stoichiometry more close to the target one (i.e. the nominal $K_{0.5}Na_{0.5}NbO_3$). Stoichiometric analysis have been performed with the same condition as before (section 5.1.3) and values are reported in table 5.3 where mean values are presented. Is it possible to observe how stable is the result we have already seen in the previous section. In fact the stoichiometric ratios between the elements is very close to the nominal one, and, with respect to the reference RTA sample, has also improved a little. This result needs to be stressed out as in figure 5.10a is possible to observe how the effect of the temperature can be overwhelming on the stoichiometry ratios. In this comparison graph, it is represented on the left how the deposition temperature in a classic PLD process can affect the stoichiometry of the film even using an overstoichiometric target. The effect of the temperature is devastating, increasing it we basically lose most of the alkali of the composition. While on the right is possible to observe that the stoichiometric ratios remain constant considering all the different RTA annealing temperatures. In this case, the target has a normal stoichiometry. Last but not least, it is important also to compare the thicker RTA sample stoichiometry with a normal PLD film as they have circa the same thickness (around 300 nm). As can be seen from the graph in figure

	Classic PLD growth	RTA reference sample	RTA (mean values)
Na/Nb	0.45	0.50	0.56
K/Nb	0.41	0.43	0.47
K/Na	0.92	0.83	0.84

Table 5.3: Stoichiometry ratios comparison between the previous works [21], [20], the RTA reference sample and the new films annealed at different temperature.

5.10b, the effect of deposition of more material to obtain a higher thickness is to stabilize the stoichiometric ratios was very close to the nominal values of the KNN compound.

5.2.4. Electrical characterization

The same electrical characterization done in the previous section is now repeated depositing again nickel pads. In this particular case, maybe due to the presence of cracks among the film, it was not straightforward to obtain repeatable measurements and it was not rare to observe quasi ohmic conduction in the voltage-current curves obtained. Even though the first result on the reference RTA was promising, in this new batch of samples we have not observed any improvement from the previous situation. Instead we have found, most of the time, a comparable or higher leakage.

Current leakage

As already cited before, the density of current leakage obtained in this new batch of samples is higher or at least comparable with respect to the one obtained in the first RTA process (i.e. the reference RTA sample). This is true for all the RTA temperatures apart from the 550°C as can be seen in figure 5.11 and in figure 5.12. In both graphs, it is possible to observe that, for the sample RTA processed at 550°C, the leakage is much lower for the left branch, while for the right branch (that represent the interface between the KNN and the bottom electrode) the leakage is the same. Since while performing the measurement on this first 550°C RTA annealed sample the curve obtained was not asymmetric, we have forced the measurement up to 10V obtaining the graph in figure 5.11a where it is possible to observe that the leakage remains low; this was done as in previous experiment by increasing the voltage over a certain threshold value. We have observed a total failure of the metal pad (and probably also of the film itself due to a high stress applied) leading to a short circuit conduction, however this is not the case maybe also due to the probably amorphous nature of the KNN. In figure 5.12a it is possible to observe the same low leakage behavior. On the other side, for films that have shown a higher degree of crystallization, considering the XRD diffractogram, the measurements

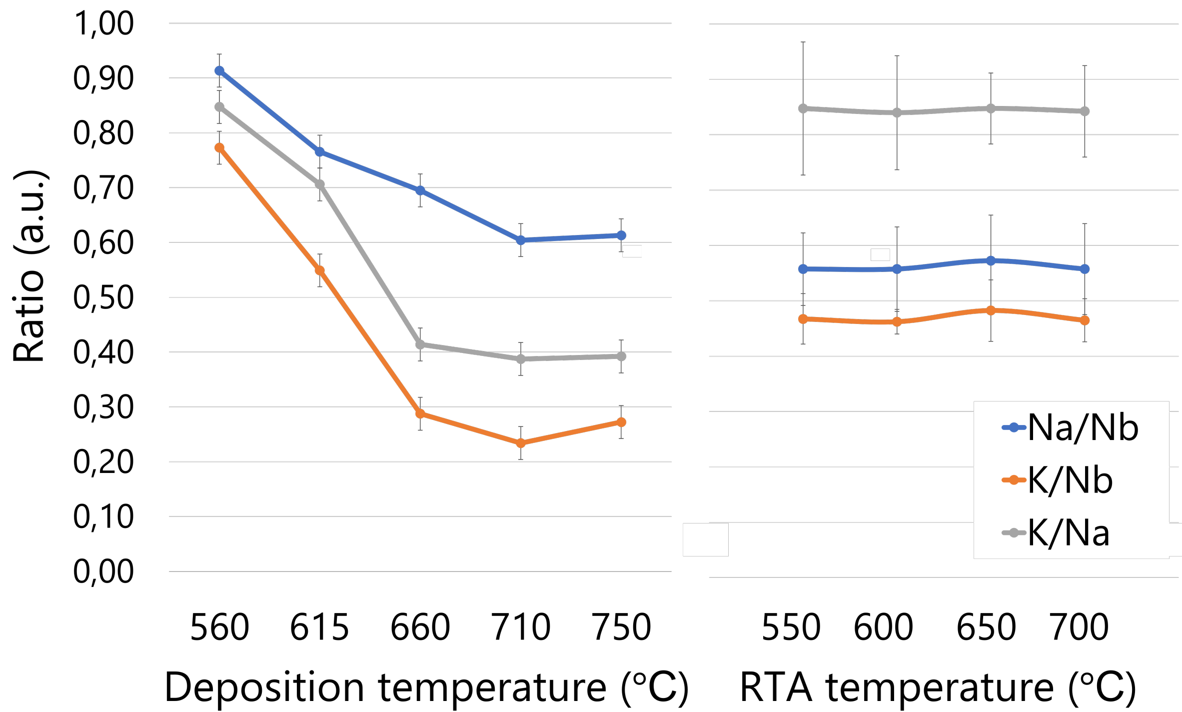

(a) The effect of the deposition temperature on film using an overstoichiometric ratio is shown on the left. Potassium and sodium are easily lost by increasing the working temperature. On the right, it is possible to observe that the stoichiometric ratios remain constant considering all the different annealing temperatures for the RTA process. In this case the target have a normal stoichiometry.

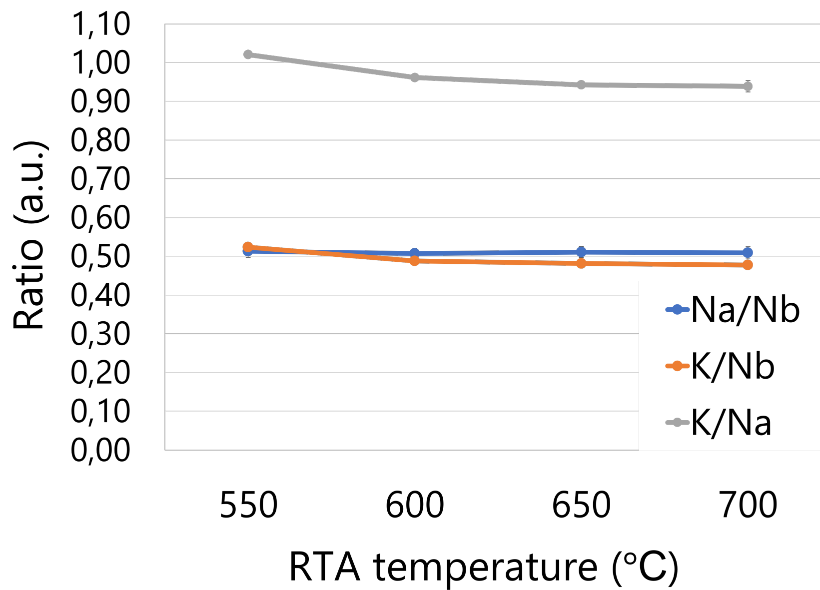

(b) Stoichiometry ratios of the thicker RTA sample. The ratios not only remain constant but are very near to the desired 0.5/0.5 value.

Figure 5.10: Stoichiometry ratios of KNN elements in function of temperature deposition and RTA temperature.

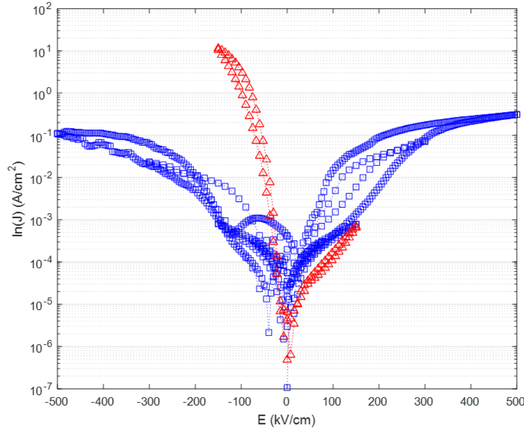

(a) RTA processed at 550°C

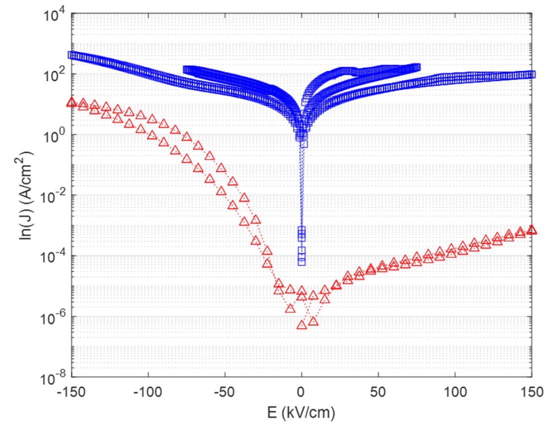

(b) RTA processed at 600°C

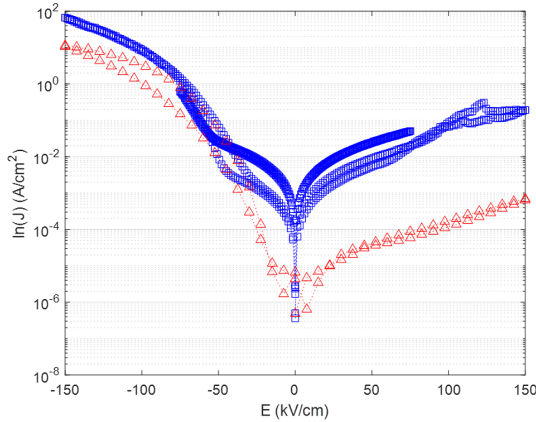

(c) RTA processed at 650°C

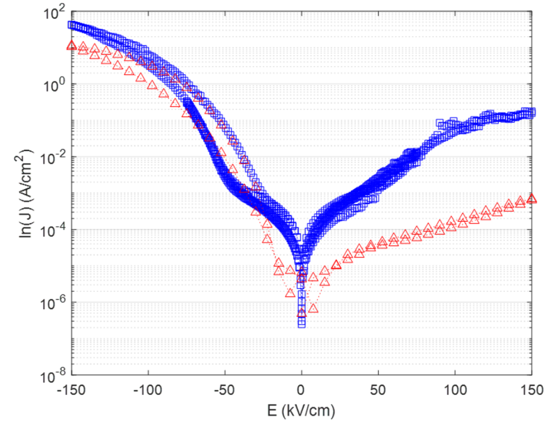

(d) RTA processed at 700°C

Figure 5.11: Density of current leakage in the different films annealed RTA processed at different temperature. Red curve is the reference RTA sample. Blue curves are subsequent RTA samples.

were not always reproducible and repeatable as pads were not always capable to sustain voltages lower than 3V. Also, as it is possible to observe in figures 5.11b and 5.12c, the films more often show an ohmic behavior. If this depends on the fact that cracks are present or it is due to some artifix of the pads is not clear, still probing the pads with current was not trivial.

5.2.5. Suggestions for the future

Many different problems have arised during the deposition of the RTA films that could be taken into account to try to get rid of the cracks along the film. One issue is related to the oxygen pressure in the chamber while depositing the KNN on the substrate. From

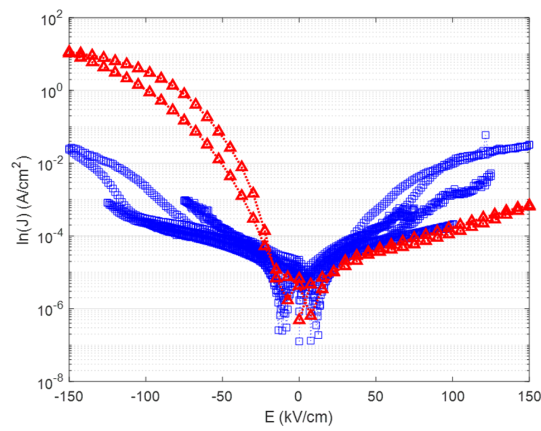

(a) RTA processed at 550°C

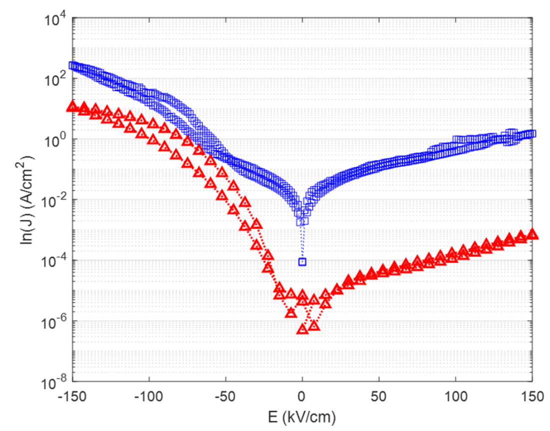

(b) RTA processed at 600°C

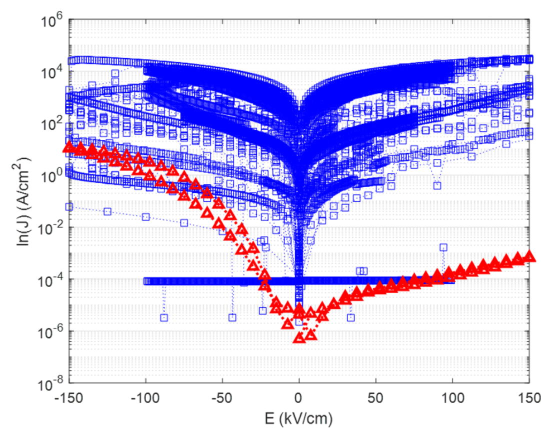

(c) RTA processed at 650°C

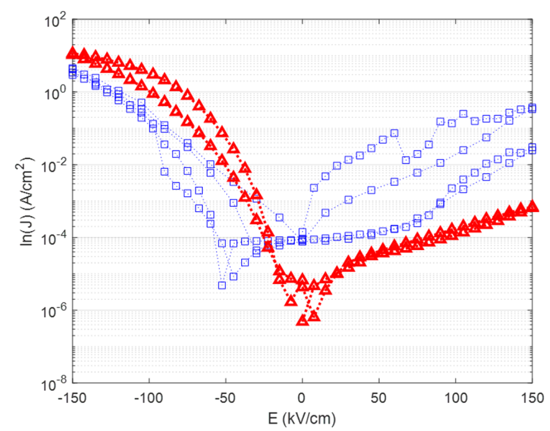

(d) RTA processed at 700°C

Figure 5.12: Density of current leakage in the different films annealed RTA processed at different temperature for a new batch of samples. Red curve is the reference RTA sample. Blue curves are subsequent RTA samples.

the standard procedure the pressure is settled to 220mTorr and must be kept constant. This was not so difficult when the automatic feedback system, that was capable of autonomously venting and pumping the oxygen, was present and fully functioning. However at some point, in between the classic PLD growth experiments and the RTA ones, the feedback loop was shifted with a valve that had to be manually operated to have a constant pressure. This for sure includes another degree of freedom in the entire process as with the feedback system even a small change in pressure was able to trigger the valve, but using a manual valve one must be able to recognize in time when and how to open or close it. Another important thing to point out is the small mechanical defect of the motor of the carousel that is responsible for moving the target up and down in the deposition chamber.In fact, it has turned out that sometimes when returning to the zero point position[1] there was a small offset in the z-axis value that could have leaded (after n cycles) to let the laser point hit the target holder (and by doing so depositing impurities on the sample) and even the glass of a viewing window (placed behind the target carousel), creating a small hole in the latter that at some point has forced to shut down all the pumps for a while. A closer inspection to the whole motor mechanism is indeed mandatory in order to understand where the problem, of the offset arises, and how to solve it to avoid the laser to point other thing than the target.

5.3. Conclusions and future direction

Low temperature deposited films have been demonstrated to be amorphous and a subsequent thermal treatment is required to promote crystallization. RTA has been exploited to crystallize the obtained films, a temperature of 650°C has found to be the threshold value for this process with the employed parameters. The obtained crystal orientation was a mixture of KNN(001) and KNN(100), thus no preferential orientation has been obtained. By SEM imaging is it possible to see that the grown films is not compact and oriented as the films obtained through classic PLD deposition. Probably due to this not good morphology the measured current leakage in RTA samples is not optimal. Also problems with the PLD machine arose and the obtained films were no more depending on the RTA process' parameters. After reestablishing the point of work of the PLD machine it should be possible to re-optimize the process for the RTA method to try to achieve a better morphology and to lower the current leakage. The future for this topic could be to find the exact condition of temperature, pressure and time to understand in which the

[1]The zero point position is a particular set of coordinates for which the laser is pointing exact in the middle of the target that moves towards the up direction while rotating thanks to the carousel. After a full cycle (when the laser has reached the outermost region of the target) the carousel moves back to the zero point position to restart the cycle.

KNN become a crystal to improve and fine tune furthermore the RTA process in order to optimize the properties of the obtained KNN film.

6 | Overall conclusions

$K_{0.5}Na_{0.5}NbO_3$ films were grown by pulsed laser deposition technique and many different aspects of this piezoelectric material were studied such as crystal structure, morphology, stoichiometry and, most importantly, its current leakage, which is a fundamental benchmark for the characterization of an active oxide. To conclude this work, a brief recap recalling the main results with the addition of suggestions for future improvements is presented.

We have successfully demonstrated that a process to create a MEMS structure such as a cantilever by using KNN as an active layer is feasible. This was been done by exploiting different microelectronic devices techniques such as photolithography and metal sputtering. The obtained trampoline structure shows a good morphology, but lacks proper insulating properties; this however seems to be material-dependent only. A further improvement of the process is of course necessary as the proposed structure was not fully suspended like the majority of the already commercially available applications, but the priority remains to be able to deposit a less defective material. The cantilevers reported in this thesis show defects that makes the processed devices not being capable of deforming in an appreciable way due to high current leakage. Numerical and simple finite elements simulations however support this stack device design as it can be used as a starting point to characterize and optimize piezoelectric cantilevers that exploit KNN as the active element.

Thanks to a deep electrical characterization, we have given an interpretation for the asymmetric curves found in the voltage-current plots in chapter 4. If the intensity of the current value can be related to free charges in the oxide layer, which are usually associated to oxygen and alkali vacancies, the peculiar asymmetric shape can be interpreted by the means of the oxygen vacancies created in between the piezoelectric layer and the metal electrodes. The oxygen vacancies create a rectifying behavior of the device. Thus a barrier, located at the bottom pad, can be depicted as a diode that when working on its reverse bias condition is limiting the amount of charges moving. Their presence has been linked to the scavenging of the oxygen by the metals in order to create local

oxidation states near the interfaces. This is also responsible for free carrier doping, and consequently, KNN is stated to be n-type doped. Future improvements must consider to correct this elemental vacancy as it is crucial to enhance the current leakage properties of the material. One way to approach the solution can be related to the increase in oxygen flow while KNN is being deposited. Another possible compensation of these vacancies can be doping with different elements. This method seems to be effective into removing the diode behavior and reducing the current leakage.

A first approach aimed to reduce the alkali loss of the KNN films has been proposed with a successful outcome. The not ideal stoichiometric configuration of the KNN and so the alkali loss of the material has been associated to the increase of free carriers inside the film leading to an increment of the current leakage. The volatility of lightweight elements such as potassium and sodium is enhanced by the high temperature of the PLD process; in particular the one during the deposition of the material. From this, the idea to deposit at a lower temperature has been exploited, this new parameter for the PLD process however has a substantial drawback: the loss of crystalline properties of the grown film. Due to this, after deposition, a thermal annealing of the film has to be performed in order to promote crystallization. Rapid thermal annealing has been employed to do so and the small amount of exposure time (60s) linked to the step gradient of the temperature, has shown to be a proper method to let the KNN become crystalline. Threshold temperature for this process parameter has also been found, demonstrating that, at least for the considered exposure time a certain energy is required to produce crystal ordering in KNN. The current leakage characterization of RTA processed samples reflect the substantial reduction of alkali loss, which was found to be less than the classic PLD process with in-situ annealing for 30min in oxygen atmosphere. However, this new process promotes a preferential orientation in KNN(001) and KNN(100) directions and not only in KNN(001) as PLD, which could be in detriment of piezoelectric properties. The former is probably due to the less energetic deposition process. Anyway preferential orientation in (001) can in principle, be improved by redefining some steps of the process.

To research how to improve the film quality of deposited KNN films (even employing different techniques) is a crucial step to be done before using it as an appropriate and feasible material for MEMS applications. Only after this, the possibility to take advantage of this promising lead free piezoelectric can be considered. For sure, an important reference to be taken as a starting point to initialize this study has been set by this thesis' work but still without the previous effort of past works even this research would not have been possible [20], [21].

Bibliography

[1] Hitoshi Ohsato. Origin of piezoelectricity on langasite. In *Materials Science and Technology*. InTech, March 2012. doi: 10.5772/18077. URL https://doi.org/10.5772/18077.

[2] Gustav Gautschi. *Piezoelectric Sensorics*. Springer Berlin Heidelberg, 2002. doi: 10.1007/978-3-662-04732-3. URL https://doi.org/10.1007/978-3-662-04732-3.

[3] M. Kimura, A. Ando, D. Maurya, and S. Priya. Lead zirconate titanate-based piezoceramics. In *Advanced Piezoelectric Materials*, pages 95–126. Elsevier, 2017. doi: 10.1016/b978-0-08-102135-4.00002-3. URL https://doi.org/10.1016/b978-0-08-102135-4.00002-3.

[4] Hassan Elahi, Khushboo Munir, Marco Eugeni, Muneeb Abrar, Asif Khan, Adeel Arshad, and Paolo Gaudenzi. A review on applications of piezoelectric materials in aerospace industry. *Integrated Ferroelectrics*, 211(1):25–44, October 2020. doi: 10.1080/10584587.2020.1803672. URL https://doi.org/10.1080/10584587.2020.1803672.

[5] Geeta Bhatt, Kapil Manoharan, Pankaj Singh Chauhan, and Shantanu Bhattacharya. *MEMS Sensors for Automotive Applications: A Review*, pages 223–239. Springer Singapore, Singapore, 2019. ISBN 978-981-13-3290-6. doi: 10.1007/978-981-13-3290-6_12. URL https://doi.org/10.1007/978-981-13-3290-6_12.

[6] Hrishikesh Kulkarni, Khaja Zohaib, A. Khusru, and K. Shravan Aiyappa. Application of piezoelectric technology in automotive systems. *Materials Today: Proceedings*, 5(10):21299–21304, 2018. doi: 10.1016/j.matpr.2018.06.532. URL https://doi.org/10.1016/j.matpr.2018.06.532.

[7] Riaz Ahmed, Fariha Mir, and Sourav Banerjee. A review on energy harvesting approaches for renewable energies from ambient vibrations and acoustic waves using piezoelectricity. *Smart Materials and Structures*, 26(8):085031, July 2017. doi: 10.1088/1361-665x/aa7bfb. URL https://doi.org/10.1088/1361-665x/aa7bfb.

[8] B. Jaffe, R. S. Roth, and S. Marzullo. Piezoelectric properties of lead zirconate-lead

titanate solid-solution ceramics. *Journal of Applied Physics*, 25(6):809–810, June 1954. doi: 10.1063/1.1721741. URL https://doi.org/10.1063/1.1721741.

[9] Indrani Coondoo, Neeraj Panwar, and Andrei Kholkin. Lead-free piezoelectrics: Current status and perspectives. *Journal of Advanced Dielectrics*, 03(02):1330002, April 2013. doi: 10.1142/s2010135x13300028. URL https://doi.org/10.1142/s2010135x13300028.

[10] Ltd Apc International. *Piezoelectric ceramics*. Apc International, December 2011.

[11] URL http://www.morganelectroceramics.co.

[12] July 2011. ISSN 17252555. URL https://data.europa.eu/doi/10.3000/17252555.L_2011.174.eng.

[13] Andrew J. Bell and Otmar Deubzer. Lead-free piezoelectrics—the environmental and regulatory issues. *MRS Bulletin*, 43(8):581–587, 2018. doi: 10.1557/mrs.2018.154.

[14] Home - STMicroelectronics. URL https://www.st.com/content/st_com/en.html.

[15] Yang Zhang, Lingyu Li, Bo Shen, and Jiwei Zhai. Effect of orthorhombic–tetragonal phase transition on structure and piezoelectric properties of KNN-based lead-free ceramics. *Dalton Transactions*, 44(17):7797–7802, 2015. doi: 10.1039/c5dt00593k. URL https://doi.org/10.1039/c5dt00593k.

[16] Yasuyoshi Saito, Hisaaki Takao, Toshihiko Tani, Tatsuhiko Nonoyama, Kazumasa Takatori, Takahiko Homma, Toshiatsu Nagaya, and Masaya Nakamura. Lead-free piezoceramics. *Nature*, 432(7013):84–87, October 2004. doi: 10.1038/nature03028. URL https://doi.org/10.1038/nature03028.

[17] Xiaopeng Wang, Jiagang Wu, Dingquan Xiao, Jianguo Zhu, Xiaojing Cheng, Ting Zheng, Binyu Zhang, Xiaojie Lou, and Xiangjian Wang. Giant piezoelectricity in potassium–sodium niobate lead-free ceramics. *Journal of the American Chemical Society*, 136(7):2905–2910, February 2014. doi: 10.1021/ja500076h. URL https://doi.org/10.1021/ja500076h.

[18] Laiming Jiang, Haoyue Xue, Ruichen Li, and Jiagang Wu. A KNN composite-based piezoelectric helix for ultrasonic transcutaneous energy harvesting. *Applied Physics Letters*, 120(23):233504, June 2022. doi: 10.1063/5.0099060. URL https://doi.org/10.1063/5.0099060.

[19] B. Tah, S. Goswami, T. Dasgupta, J. Bera, P. Sinha, D. Kundu, S. Sen, and A. Sen.

Ferroelectric fatigue of KNN ceramics. *Ferroelectrics*, 481(1):119–125, June 2015. doi: 10.1080/00150193.2015.1051446. URL https://doi.org/10.1080/00150193.2015.1051446.

[20] C. Groppi, L. Mondonico, F. Maspero, C. Rinaldi, M. Asa, and R. Bertacco. Effect of substrate preparation on the growth of lead-free piezoelectric $(K_{0.5}Na_{0.5})NbO_3$ on Pt(111). *Journal of Applied Physics*, 129(19):194102, May 2021. ISSN 0021-8979, 1089-7550. doi: 10.1063/5.0050038. URL https://aip.scitation.org/doi/10.1063/5.0050038.

[21] Mondonico L. Influence of top electrodes on leakage current in $K_{0.5}Na_{0.5})NbO_3$ thin films. URL https://www.politesi.polimi.it/handle/10589/179724.

[22] LASSE (LAyered Structures for Spin Electronics) | PoliFAB. URL https://www.polifab.polimi.it/equipments/lasse/.

[23] Mihai Stafe, C Negutu, Niculae N Puscas, and IM Popescu. Pulsed laser ablation of solids. *Rom. Rep. Phys*, 62(4):758–770, 2010.

[24] Douglas B. Chrisey and G. K. Hubler, editors. *Pulsed laser deposition of thin films*. J. Wiley, New York, 1994. ISBN 9780471592181.

[25] M. Abazari and A. Safari. Effects of doping on ferroelectric properties and leakage current behavior of KNN-LT-LS thin films on SrTiO3 substrate. *Journal of Applied Physics*, 105(9):094101, May 2009. doi: 10.1063/1.3120922. URL https://doi.org/10.1063/1.3120922.

[26] Laser yag - Powerlite DLS 8000. URL https://amplitude-laser.com/products/nanosecond-lasers/standard-nanosecond-lasers/powerlite-dls-8000/.

[27] Shanti Deemyad and Isaac F Silvera. Temperature dependence of the emissivity of platinum in the ir. *Review of scientific instruments*, 79(8):086105, 2008.

[28] Sushmita Dwivedi, Manish Badole, Hari Narayanan Vasavan, and Sunil Kumar. Influence of annealing environments on the conduction behaviour of KNN-based ceramics. *Ceramics International*, 48(13):18057–18066, July 2022. doi: 10.1016/j.ceramint.2022.02.235. URL https://doi.org/10.1016/j.ceramint.2022.02.235.

[29] UniTemp - your partner for all kind of thermal processes. URL https://unitemp.de/EN/rtprta-ovens/rtp-series-and--vpo/rtp-150/.

[30] Rapid Thermal Annealer – UniTemp RTP-150-HV | PoliFAB. URL https://www.polifab.polimi.it/equipments/rapid-thermal-annealer-unitemp-rtp-150-hv/.

[31] OpenStax. 10.6 Lattice Structures in Crystalline Solids. 2016. URL https://iu.pressbooks.pub/openstaxchemistry/chapter/10-6-lattice-structures-in-crystalline-solids/.

[32] Die Technologie hinter ZEISS Crossbeam. URL https://www.zeiss.ch/mikroskopie/produkte/fib-sem-instruments/crossbeam/crossbeam-technology.html.

[33] Felix Utama Kosasih, Stefania Cacovich, Giorgio Divitini, and Caterina Ducati. Nanometric chemical analysis of beam-sensitive materials: A case study of STEM-EDX on perovskite solar cells. *Small Methods*, 5(2):2000835, November 2020. doi: 10.1002/smtd.202000835. URL https://doi.org/10.1002/smtd.202000835.

[34] Joseph I. Goldstein, Dale E. Newbury, Joseph R. Michael, Nicholas W.M. Ritchie, John Henry J. Scott, and David C. Joy. *Scanning Electron Microscopy and X-Ray Microanalysis*. Springer New York, 2018. doi: 10.1007/978-1-4939-6676-9. URL https://doi.org/10.1007/978-1-4939-6676-9.

[35] *Principles of X-ray Diffraction*, chapter 1, pages 1–40. John Wiley Sons, Ltd, 2005. ISBN 9783527607594. doi: https://doi.org/10.1002/3527607595.ch1. URL https://onlinelibrary.wiley.com/doi/abs/10.1002/3527607595.ch1.

[36] X-ray diffraction (XRD) basics and application, April 2019. URL https://chem.libretexts.org/@go/page/148442.

[37] XRD products from Rigaku | Rigaku Global Website. URL https://www.rigaku.com/products/xrd.

[38] X-Ray Diffractometer Rigaku SmartLab XE | PoliFAB. URL https://www.polifab.polimi.it/equipments/smartlab-xrd/.

[39] Worku Wubet. Green synthesis of cuo nanoparticles for the application of dye sensitized solar cell. 07 2019.

[40] Shahin A. Mojarad, Jonathan P. Goss, Kelvin S. K. Kwa, Zhiyong Zhou, Raied A. S. Al-Hamadany, Daniel J. R. Appleby, Nikhil K. Ponon, and Anthony O'Neill. Leakage current asymmetry and resistive switching behavior of SrTiOsub3/sub. *Applied Physics Letters*, 101(17):173507, October 2012. doi: 10.1063/1.4764544. URL https://doi.org/10.1063/1.4764544.

[41] Thin Film Deposition Sputtering Manufacturer. URL https://www.ajaint.com/.

[42] Metal deposition: Plasma-based processes. In *Encyclopedia of Plasma Technology*,

pages 722–740. CRC Press, December 2016. doi: 10.1081/e-eplt-120053919. URL https://doi.org/10.1081/e-eplt-120053919.

[43] Attrezzature Sputtering per deposizione film sottili - KENOSISTEC, . URL https://www.kenosistec.com/it.

[44] Padraic O'Reilly. *Development of a Nanoplasmonic Ruler: Biosensing at the Subnanoscale*. PhD thesis, 06 2017.

[45] +IBE | PoliFAB, . URL https://www.polifab.polimi.it/ibe/.

[46] SUSS MicroTec - Semiconductor Equipment Manufacturer, . URL https://www.suss.com/en.

[47] Keithley Instruments & Products | Tektronix. URL https://www.tek.com/en/products/keithley.

[48] Satoshi Takeshita. MODELING OF SPACE-CHARGE-LIMITED CURRENT INJECTION INCORPORATING AN ADVANCED MODEL OF THE POOLE-FRENKEL EFFECT. *All Theses*, September 2008. URL https://tigerprints.clemson.edu/all_theses/473.

[49] Manual Electric Probe System – SÜSS MicroTec PM5 | PoliFAB, . URL https://www.polifab.polimi.it/equipments/pm5/.

[50] Mario Lanza, editor. *Conductive atomic force microscopy*. Wiley-VCH Verlag, Weinheim, Germany, October 2017.

[51] Park NX10 - Overview | Park Atomic Force Microscope. URL https://www.parksystems.com/products/small-sample-afm/park-nx10/overview.

[52] Conductive AFM. URL https://www.parksystems.com/index.php/park-spm-modes/94-electrical-properties/233-conductive-afm.

[53] Maskless Aligner – Heidelberg MLA100 | PoliFAB. URL https://www.polifab.polimi.it/equipments/heidelberg-mla100-maskless-aligner/.

[54] Björn Stuhrmann. *Self-Organized Active Biopolymer Networks in Migrating Living Cells*. PhD thesis, 08 2009.

[55] The Power of Direct Writing Heidelberg Instruments. URL https://heidelberg-instruments.com/.

[56] James J Licari and Leonard R Enlow. *Hybrid microcircuit technology handbook*. William Andrew Publishing, Norwich, CT, 2 edition, December 1998.

[57] Photoresist AZ 5214E Photoresists MicroChemicals GmbH. URL https://www.microchemicals.com/products/photoresists/az_5214_e.html.

[58] MicroChemicals. Basics of microstructuring, 2013. https://www.microchemicals.com/technical_information/image_reversal_resists.pdf.

[59] JACEK BABOROWSKI. Microfabrication of piezoelectric MEMS. *Integrated Ferroelectrics*, 66(1):3–17, January 2004. doi: 10.1080/10584580490894302. URL https://doi.org/10.1080/10584580490894302.

[60] S Tadigadapa and K Mateti. Piezoelectric MEMS sensors: state-of-the-art and perspectives. *Measurement Science and Technology*, 20(9):092001, July 2009. doi: 10.1088/0957-0233/20/9/092001. URL https://doi.org/10.1088/0957-0233/20/9/092001.

[61] Fumio Narita, Zhenjin Wang, Hiroki Kurita, Zhen Li, Yu Shi, Yu Jia, and Constantinos Soutis. A review of piezoelectric and magnetostrictive biosensor materials for detection of COVID-19 and other viruses. *Advanced Materials*, 33(1):2005448, November 2020. doi: 10.1002/adma.202005448. URL https://doi.org/10.1002/adma.202005448.

[62] Lokesh Singh Panwar, Sachin Kala, Varij Panwar, Shailesh Singh Panwar, and Sushant Sharma. Design of mems piezoelectric blood pressure sensor. In *2017 3rd International Conference on Advances in Computing,Communication Automation (ICACCA) (Fall)*, pages 1–7, 2017. doi: 10.1109/ICACCAF.2017.8344698.

[63] Fundamentals of piezoelectricity. In *Advances in Industrial Control*, pages 9–35. Springer-Verlag. doi: 10.1007/1-84628-332-9_2. URL https://doi.org/10.1007/1-84628-332-9_2.

[64] Andrea Mazzalai, Davide Balma, Nachiappan Chidambaram, Ramin Matloub, and Paul Muralt. Characterization and fatigue of the converse piezoelectric effect in PZT films for MEMS applications. *Journal of Microelectromechanical Systems*, 24(4):831–838, August 2015. doi: 10.1109/jmems.2014.2353855. URL https://doi.org/10.1109/jmems.2014.2353855.

[65] July A. Galeano, Patrick Sandoz, Artur Zarzycki, Laurent Robert, and Juan M. Jaramillo. Microfabrication of position reference patterns onto glass microscope slides for high-accurate analysis of dynamic cellular events. *TecnoLógicas*, 20(39), 2017. ISSN 0123-7799/2256-5337. URL http://www.scielo.org.co/pdf/teclo/v20n39/v20n39a08.pdf.

[66] Raymond A. Serway. *Principles of Physics (2nd ed.)*. Saunders College Pub., 1998. ISBN 978-0-03-020457-9.

[67] Minh D. Nguyen, Matthijn Dekkers, Evert P. Houwman, Hien T. Vu, Hung N. Vu, and Guus Rijnders. Lead-free (k 0.5 na 0.5)NbO 3 thin films by pulsed laser deposition driving MEMS-based piezoelectric cantilevers. *Materials Letters*, 164: 413–416, February 2016. doi: 10.1016/j.matlet.2015.11.044. URL https://doi.org/10.1016/j.matlet.2015.11.044.

[68] Takahiro Namazu, Tatsuya Fujii, Motohiro Takahashi, Mitsuhiro Tanaka, and Shozo Inoue. A simple experimental technique for measuring the poisson's ratio of microstructures. *Journal of Microelectromechanical Systems*, 22(3):625–636, June 2013. doi: 10.1109/jmems.2012.2237383. URL https://doi.org/10.1109/jmems.2012.2237383.

[69] COMSOL: Multiphysics Software for Optimizing Designs. URL https://www.comsol.com/.

[70] Keysight. B1500A Semiconductor Device Parameter Analyzer. URL https://www.keysight.com/it/en/products/parameter-device-analyzers-curve-tracer/precision-current-voltage-analyzers/b1500a-semiconductor-device-parameter-analyzer.html.

[71] S. Fujisaki, Y. Fujisaki, and H. Ishiwara. Excellent ferroelectricity of thin poly(vinylidene fluoride-trifluoroethylene) copolymer films and low voltage operation of capacitors and diodes. *IEEE Transactions on Ultrasonics, Ferroelectrics and Frequency Control*, 54(12):2592–2594, December 2007. doi: 10.1109/tuffc.2007.583. URL https://doi.org/10.1109/tuffc.2007.583.

[72] Polytec laser vibration sensors. URL https://www.polytec.com/int/vibrometry/products.

[73] S. Trolier-McKinstry and P. Muralt. Thin film piezoelectrics for MEMS. *Journal of Electroceramics*, 12(1/2):7–17, January 2004. doi: 10.1023/b:jecr.0000033998.72845.51. URL https://doi.org/10.1023/b:jecr.0000033998.72845.51.

[74] A. Reichmann, A. Zankel, H. Reingruber, P. Pölt, and K. Reichmann. Direct observation of ferroelectric domain formation by environmental scanning electron microscopy. *Journal of the European Ceramic Society*, 31(15):2939–2942, December 2011. doi: 10.1016/j.jeurceramsoc.2011.05.043. URL https://doi.org/10.1016/j.jeurceramsoc.2011.05.043.

[75] Mingmin Zhu, Xunzhong Shang, Gang Chang, Mingkai Li, Xiong Liu, Taosheng Zhou, and Yunbin He. Pulsed laser deposition of single-phase lead-free NKLNST thin films with k- and na-excess targets. *Journal of Alloys and Compounds*, 567: 97–101, August 2013. doi: 10.1016/j.jallcom.2013.03.049. URL https://doi.org/10.1016/j.jallcom.2013.03.049.

[76] Elisabeth Soergel. Piezoresponse force microscopy (PFM). *Journal of Physics D: Applied Physics*, 44(46):464003, November 2011. doi: 10.1088/0022-3727/44/46/464003. URL https://doi.org/10.1088/0022-3727/44/46/464003.

[77] Jin Luo, Deyang Chen, Hao Qian, Yunfei Liu, and Yinong Lyu. Orientation dependent intrinsic and extrinsic contributions to the piezoelectric response in lead-free (na0.5k0.5)NbO3 based films. *Journal of Alloys and Compounds*, 906:164346, June 2022. doi: 10.1016/j.jallcom.2022.164346. URL https://doi.org/10.1016/j.jallcom.2022.164346.

[78] Masato Matsubara, Toshiaki Yamaguchi, Koichi Kikuta, and Shin ichi Hirano. Synthesis and characterization of (ksub0.5/subnasub0.5/sub)(nbsub0.7/subtasub0.3/sub)osub3/subpiezoelectric ceramics sintered with sintering aid ksub5.4/subcusub1.3/subtasub10/subosub29/sub. *Japanese Journal of Applied Physics*, 44(9A):6618–6623, September 2005. doi: 10.1143/jjap.44.6618. URL https://doi.org/10.1143/jjap.44.6618.

[79] Chung-Ming Weng, Cheng-Che Tsai, Cheng-Shong Hong, Chun-Cheng Lin, Chan-Ching Chen, Sheng-Yuan Chu, Jyh Sheen, Zong-You Chen, and Hsiu-Hsien Su. Effects of non-stoichiometry on the microstructure, oxygen vacancies, and electrical properties of KNN-based thin films. *ECS Journal of Solid State Science and Technology*, 5(9):N49–N56, 2016. doi: 10.1149/2.0291609jss. URL https://doi.org/10.1149/2.0291609jss.

[80] Savita Sharma, Monika Tomar, and Vinay Gupta. Effect of top metal contact on the ferroelectric photovoltaic response of BFO thin film capacitors. *Vacuum*, 158: 117–120, December 2018. doi: 10.1016/j.vacuum.2018.09.032. URL https://doi.org/10.1016/j.vacuum.2018.09.032.

[81] Shweta Sharma, Ashok Kumar, Vinay Gupta, and Monika Tomar. Dielectric and ferroelectric studies of KNN thin film grown by pulsed laser deposition technique. *Vacuum*, 160:233–237, February 2019. doi: 10.1016/j.vacuum.2018.11.036. URL https://doi.org/10.1016/j.vacuum.2018.11.036.

[82] Lucian Pintilie, Ionela Vrejoiu, Dietrich Hesse, and Marin Alexe. The influence

of the top-contact metal on the ferroelectric properties of epitaxial ferroelectric pb(zr0.2ti0.8)o3 thin films. *Journal of Applied Physics*, 104(11):114101, December 2008. doi: 10.1063/1.3021293. URL https://doi.org/10.1063/1.3021293.

[83] J. Hölzl and F. K. Schulte. *Work function of metals*, pages 1–150. Springer Berlin Heidelberg, Berlin, Heidelberg, 1979. ISBN 978-3-540-35253-2. doi: 10.1007/BFb0048919. URL https://doi.org/10.1007/BFb0048919.

[84] L Michalas, A Khiat, S Stathopoulos, and T Prodromakis. Electrical characteristics of interfacial barriers at metal—TiOsub2/sub contacts. *Journal of Physics D: Applied Physics*, 51(42):425101, September 2018. doi: 10.1088/1361-6463/aadbd2. URL https://doi.org/10.1088/1361-6463/aadbd2.

[85] Longxing Su, Zhaoyun Guan, Qiushi Liu, and Yuan Zhu. Ohmic-schottky conversion of zno/metal contact modulated by a plasma surface treatment method. *Results in Materials*, 15:100290, 2022. ISSN 2590-048X. doi: https://doi.org/10.1016/j.rinma.2022.100290. URL https://www.sciencedirect.com/science/article/pii/S2590048X22000383.

[86] H.N. Al-Shareef, A.I. Kingon, X. Chen, K.R. Bellur, and O. Auciello. Contribution of electrodes and microstructures to the electrical properties of pb(zrsub0.53/subtisub0.47/sub)osub3/sub thin film capacitors. *Journal of Materials Research*, 9(11):2968–2975, November 1994. doi: 10.1557/jmr.1994.2968. URL https://doi.org/10.1557/jmr.1994.2968.

[87] Ali Madani, Ridha Ben Mrad, and Tony Sinclair. Characterization of rf sputtered thin film potassium sodium niobate (knn) with silicon and nickel electrodes. *Microsystem Technologies*, 23, 06 2017. doi: 10.1007/s00542-016-3106-x.

[88] Tao Li, Genshui Wang, Kui Li, Nossikpendou Sama, Denis Remiens, and Xianlin Dong. Influence of LNO top electrodes on electrical properties of KNN/LNO thin films prepared by RF magnetron sputtering. *Journal of the American Ceramic Society*, 96(3):787–790, October 2012. doi: 10.1111/jace.12047. URL https://doi.org/10.1111/jace.12047.

[89] Fadhel El Kamel, Patrice Gonon, and Christophe Vallée. Experimental evidence for the role of electrodes and oxygen vacancies in voltage nonlinearities observed in hig k metal-insulator-metal capacitors. *Applied Physics Letters*, 91:172909–172909, 10 2007. doi: 10.1063/1.2803221.

[90] Chiara Groppi, Federico Maspero, Andrea Rovelli, Edoardo Albisetti, Miguel Badillo, Riccardo Bertacco, Gerardo Malavena, and Christian Compagnoni.

Electrode-dependent asymmetric conduction mechanisms in $Ka_{0.5}Na_{0.5}NbO_3$ micro capacitors. unpublished.

[91] Xiaozhi Wang, Yu Huan, Zhenxing Wang, Xiujuan Lin, Shifeng Huang, Tao Wei, Longtu Li, and Xiaohui Wang. Electrical conduction and dielectric relaxation mechanisms in the KNN-based ceramics. *Journal of Applied Physics*, 126(10):104101, September 2019. doi: 10.1063/1.5110582. URL https://doi.org/10.1063/1.5110582.

[92] Tao Li, Genshui Wang, Kui Li, Gang Du, Ying Chen, Zhiyong Zhou, Denis Rémiens, and Xianlin Dong. Electrical properties of lead-free knn films on sro/sto by rf magnetron sputtering. *Ceramics International*, 40(1, Part A):1195–1198, 2014. ISSN 0272-8842. doi: https://doi.org/10.1016/j.ceramint.2013.07.005. URL https://www.sciencedirect.com/science/article/pii/S0272884213007992.

[93] C. Borderon, A. E. Brunier, K. Nadaud, R. Renoud, M. Alexe, and H. W. Gundel. Domain wall motion in pb(zr0.20ti0.80)o3 epitaxial thin films. *Scientific Reports*, 7(1), June 2017. doi: 10.1038/s41598-017-03757-y. URL https://doi.org/10.1038/s41598-017-03757-y.

[94] Jozef Osvald. Back-to-back connected asymmetric schottky diodes with series resistance as a single diode. *physica status solidi (a)*, 212(12):2754–2758, July 2015. doi: 10.1002/pssa.201532374. URL https://doi.org/10.1002/pssa.201532374.

[95] Neal D. Reynolds, Cristian D. Panda, and John M. Essick. Capacitance-voltage profiling: Research-grade approach versus low-cost alternatives. *American Journal of Physics*, 82(3):196–205, 2014. doi: 10.1119/1.4864162. URL https://doi.org/10.1119/1.4864162.

[96] Gh. H. Khorrami, Ahmad Kompany, and Ali Khorsand Zak. Structural and optical properties of (k,na)nbo3 nanoparticles synthesized by a modified sol–gel method using starch media. *Advanced Powder Technology*, 26:113–118, 2015.

[97] Fayaz Hussain, Iasmi Sterianou, Amir Khesro, Derek C. Sinclair, and Ian M. Reaney. p-type/n-type behaviour and functional properties of kxna(1-x)nbo3 (0.49x0.51) sintered in air and n2. *Journal of the European Ceramic Society*, 38(9):3118–3126, 2018. ISSN 0955-2219. doi: https://doi.org/10.1016/j.jeurceramsoc.2018.03.013. URL https://www.sciencedirect.com/science/article/pii/S0955221918301389.

[98] Phoi Chin Goh, Kui Yao, and Zhong Chen. Titanium diffusion into (k0.5na0.5)nbo3 thin films deposited on pt/ti/sio2/si substrates and corresponding effects. *Journal of the American Ceramic Society*, 92(6):1322–1327, 2009. doi: https://doi.org/10.

1111/j.1551-2916.2009.03058.x. URL https://ceramics.onlinelibrary.wiley.com/doi/abs/10.1111/j.1551-2916.2009.03058.x.

[99] S. Brivio, C. Magen, A. A. Sidorenko, D. Petti, M. Cantoni, M. Finazzi, F. Ciccacci, R. De Renzi, M. Varela, S. Picozzi, and R. Bertacco. Effects of au nanoparticles on the magnetic and transport properties of $la_{0.67}sr_{0.33}mno_3$ ultrathin layers. *Phys. Rev. B*, 81:094410, Mar 2010. doi: 10.1103/PhysRevB.81.094410. URL https://link.aps.org/doi/10.1103/PhysRevB.81.094410.

[100] Abdulmecit TÜRÜT. Oncurrent-voltage and capacitance-voltage characteristics of metal-semiconductor contacts. *TURKISH JOURNAL OF PHYSICS*, 44(4): 302–347, August 2020. doi: 10.3906/fiz-2007-11. URL https://doi.org/10.3906/fiz-2007-11.

[101] Fu-Chien Chiu. A review on conduction mechanisms in dielectric films. *Advances in Materials Science and Engineering*, 2014:1–18, 2014. doi: 10.1155/2014/578168. URL https://doi.org/10.1155/2014/578168.

[102] Teng Li, Song Dai, Liqiang Xu, Yiwen Liu, Hao Zhuo, Ke Wang, Haifeng Wang, and Feng Chen. Electrical property and phase transition analysis of KNN-based lead-free ferroelectric films. *Materials Research Express*, 9(5):056403, May 2022. doi: 10.1088/2053-1591/ac6b8c. URL https://doi.org/10.1088/2053-1591/ac6b8c.

[103] J. Joshua Yang, Matthew D. Pickett, Xuema Li, Douglas A. A. Ohlberg, Duncan R. Stewart, and R. Stanley Williams. Memristive switching mechanism for metal/oxide/metal nanodevices. *Nature Nanotechnology*, 3(7):429–433, June 2008. doi: 10.1038/nnano.2008.160. URL https://doi.org/10.1038/nnano.2008.160.

[104] Kenji Shibata, Kazutoshi Watanabe, Toshiaki Kuroda, and Takenori Osada. KNN lead-free piezoelectric films grown by sputtering. *Applied Physics Letters*, 121(9): 092901, August 2022. doi: 10.1063/5.0104583. URL https://doi.org/10.1063/5.0104583.

[105] Sung Sik Won, Joonhee Lee, Vineeth Venugopal, Dong-Joo Kim, Jinkee Lee, Ill Won Kim, Angus I. Kingon, and Seung-Hyun Kim. Lead-free mn-doped (ksub0.5/sub, nasub0.5/sub)NbOsub3/sub piezoelectric thin films for MEMS-based vibrational energy harvester applications. *Applied Physics Letters*, 108(23):232908, June 2016. doi: 10.1063/1.4953623. URL https://doi.org/10.1063/1.4953623.

[106] Lingyan Wang, Wei Ren, Wenhui Ma, Ming Liu, Peng Shi, and Xiaoqing Wu. Improved electrical properties for mn-doped lead-free piezoelectric potassium sodium

niobate ceramics. *AIP Advances*, 5(9):097120, September 2015. doi: 10.1063/1.4930820. URL https://doi.org/10.1063/1.4930820.

[107] Keith G. Brooks, Ian M. Reaney, Radosveta Klissurska, Y. Huang, L. Bursill, and N. Setter. Orientation of rapid thermally annealed lead zirconate titanate thin films on (111) pt substrates. *Journal of Materials Research*, 9(10):2540–2553, October 1994. doi: 10.1557/jmr.1994.2540. URL https://doi.org/10.1557/jmr.1994.2540.

[108] Jian Lu, Yi Zhang, Tsuyoshi Ikehara, Takashi Mihara, and Ryutaro Maeda. Effects of rapid thermal annealing on nucleation, growth, and properties of lead zirconate titanate films. *IEEE Transactions on Ultrasonics, Ferroelectrics and Frequency Control*, 54(12):2548–2554, December 2007. doi: 10.1109/tuffc.2007.575. URL https://doi.org/10.1109/tuffc.2007.575.

[109] CLUSTERLINE® Family. URL https://evatecnet.com/products/clusterline-family/.

[110] Robert Eason, editor. *Pulsed Laser Deposition of Thin Films: Applications-Led Growth of Functional Materials*. John Wiley & Sons, Inc., Hoboken, NJ, USA, November 2006. ISBN 9780470052129 9780471447092. doi: 10.1002/0470052120. URL http://doi.wiley.com/10.1002/0470052120.

[111] G BECK, H FISCHER, E MUTORO, V SROT, K PETRIKOWSKI, E TCHERNYCHOVA, M WUTTIG, M RUHLE, B LUERSEN, and J JANEK. Epitaxial pt(111) thin film electrodes on YSZ(111) and YSZ(100) — preparation and characterisation. *Solid State Ionics*, 178(5-6):327–337, March 2007. doi: 10.1016/j.ssi.2007.01.025. URL https://doi.org/10.1016/j.ssi.2007.01.025.

[112] Jie Yang, Faqiang Zhang, Qunbao Yang, Zhifu Liu, Yongxiang Li, Yun Liu, and Qiming Zhang. Large piezoelectric properties in KNN-based lead-free single crystals grown by a seed-free solid-state crystal growth method. *Applied Physics Letters*, 108(18):182904, May 2016. doi: 10.1063/1.4948642. URL https://doi.org/10.1063/1.4948642.

[113] *Piezoelectric Ceramics*. Elsevier, 1971. doi: 10.1016/b978-0-12-379550-2.x5001-7. URL https://doi.org/10.1016/b978-0-12-379550-2.x5001-7.

[114] D. W. Baker, P. A. Thomas, N. Zhang, and A. M. Glazer. Structural study of ksub ix/i /subnasub1 - ix/i /subNbOsub3/sub (KNN) for compositions in the range ix/i = 0.24–0.36. *Acta Crystallographica Section B Structural Science*, 65(1):22–28, December 2008. doi: 10.1107/s0108768108037361. URL https://doi.org/10.1107/s0108768108037361.

[115] Harry G Brittain. X-ray diffraction iii: pharmaceutical applications. *Spectroscopy*, 16(7):14–18, 2001.

[116] Fytik. URL https://fityk.nieto.pl/.

[117] H Seiler. Secondary electron emission in the scanning electron microscope. *Journal of Applied Physics*, 54(11):R1–R18, November 1983. doi: 10.1063/1.332840. URL https://doi.org/10.1063/1.332840.

[118] Jae-Wung Lee, Jong-Jin Choi, Gun-Tae Park, Chee-Sung Park, and Hyoun-Ee Kim. Thick pb(zr, ti)osub3/sub films fabricated by inducing residual compressive stress during the annealing process. *Journal of Materials Research*, 20(11):2898–2901, November 2005. doi: 10.1557/jmr.2005.0383. URL https://doi.org/10.1557/jmr.2005.0383.

[119] Jian Lu, Yi Zhang, Tsuyoshi Ikehara, Takashi Mihara, and Ryutaro Maeda. Effects of rapid thermal annealing on nucleation, growth, and properties of lead zirconate titanate films. *IEEE Transactions on Ultrasonics, Ferroelectrics, and Frequency Control*, 54(12):2548–2554, 2007. doi: 10.1109/TUFFC.2007.575.

[120] A Safari and M Abazari. Lead-free piezoelectric ceramics and thin films. *IEEE Transactions on Ultrasonics, Ferroelectrics and Frequency Control*, 57(10):2165–2176, October 2010. doi: 10.1109/tuffc.2010.1674. URL https://doi.org/10.1109/tuffc.2010.1674.

[121] Hai Joon Lee, Ill Won Kim, Jin Soo Kim, Chang Won Ahn, and Bae Ho Park. Ferroelectric and piezoelectric properties of na0.52k0.48nbo3 thin films prepared by radio frequency magnetron sputtering. *Applied Physics Letters*, 94(9):092902, March 2009. doi: 10.1063/1.3095500. URL https://doi.org/10.1063/1.3095500.

[122] Xin Wang, Ulf Helmersson, Sveinn Olafsson, Staffan Rudner, Lars-David Wernlund, and Spartak Gevorgian. Growth and field dependent dielectric properties of epitaxial na0.5k0.5nbo3 thin films. *Applied Physics Letters*, 73(7):927–929, August 1998. doi: 10.1063/1.122040. URL https://doi.org/10.1063/1.122040.

[123] Bo-Yun Kim, Tae-Geun Seong, In-Tae Seo, Min-Soo Jang, Sahn Nahm, Jong-Yun Kang, and Seok-Jin Yoon. Effects of annealing atmosphere on the structural and electrical properties of (na0.5k0.5)NbO3 thin films grown by RF magnetron sputtering. *Acta Materialia*, 60(6-7):3107–3112, April 2012. doi: 10.1016/j.actamat.2012.02.015. URL https://doi.org/10.1016/j.actamat.2012.02.015.

[124] Shigang Huang, Qingning Li, Ling Yang, Jiwen Xu, Changrong Zhou, Guohua

Chen, Changlai Yuan, and Guanghui Rao. Enhanced piezoelectric properties by reducing leakage current in co modified 0.7bifeo3-0.3batio3 ceramics. *Ceramics International*, 44(8):8955–8962, June 2018. doi: 10.1016/j.ceramint.2018.02.095. URL https://doi.org/10.1016/j.ceramint.2018.02.095.

[125] Xin Yan, Wei Ren, Xiaoqing Wu, Peng Shi, and Xi Yao. Lead-free (k, na)NbO3 ferroelectric thin films: Preparation, structure and electrical properties. *Journal of Alloys and Compounds*, 508(1):129–132, October 2010. doi: 10.1016/j.jallcom.2010.08.025. URL https://doi.org/10.1016/j.jallcom.2010.08.025.

List of Figures

1.1 Schematic representation of inversion-symmetric and non inversion-symmetric crystals (from [1]). 1
1.2 Perovskite structure of a ferroelectric material. If the temperature is below its critical value T_c the crystal is orthorombic and net polarization is present due to the slightly displacement of the atom in the middle of the structure. PZT and KNN also adopt this structure (from [3]). 2

2.1 Target photos during the process and after the ablation and scheme of the working principle. 8
2.2 LASSE scheme. The red perimeter highlight the PLD experimental apparatus used to deposit KNN. 10
2.3 UniTemp RTP-150-HV [30]. 12
2.4 Raith LEO 1525 in the yellow room and working principle of the SEM. . . 14
2.5 EDX spectra example and spatial information encoding. 15
2.6 X-Ray Diffractometer used and working principle. 18
2.7 AJA magnetron sputtering machine and schematic. 20
2.8 Ion Beam Etching machine and schematic. 21
2.9 IBE schematic to remove the Ni layer after the Ti pads deposition. 21
2.10 23
2.11 C-AFM schematic and a measure example. 24
2.12 Used instrumentation and visualization of the photolitographic process. . . 25

3.1 Laminated Piezoelectric/Si deflecting structures used in piezoelectric MEMS: bridge, cantilever and suspended membrane (from [59]). 28
3.2 Mask used to pattern the platinum top electrodes and sketch of the obtained structure. 30
3.3 Visual inspection and SEM images of the obtained cantilevers. 32
3.4 Caption 34
3.5 Top bottom current measurements of the cantilevers. Mean values of the curves are reported 35

3.6 Numerical simulations results. 37
3.7 Keysight B1500A characterization. Courtesy of STMicroelectronics. 38
3.8 Vibrometric measurements. Courtesy of STMicroelectronics. 39

4.1 Comparison of XRD diffractogram. On the left, the one taken from past works is shown while on the right the acquired diffractogram of films deposited in this work is shown. As it is possible to observe, the two diffractogram show strong preferential growth direction of the KNN out of plane. Other peaks such as KNN(002) and KNN(200) are clearly visible in the diffractogram acquired in this work; this is due to the multiplicity of the Bragg's law (see section 2.3.3). 44
4.2 Comparison between the 270 nm film and the 300 nm one. The films are very similiar and share the same morphological properties. 45
4.3 I-V curves taken at 4V for different Ni pads on the same portion of film. Curves are reported in black to better visualize the dispersion trend of the measurements. 48
4.4 Increasing current density leakage after cycling different measurements on the same metal pad. Blue line is the first measure, red line is the last one and black lines are the ones taken in between. 48
4.5 Burned pt pads after reaching the breakdown voltage, pads are clearly damaged due to the applied voltage. This image can also be taken as a reference to understand how much variability we can have in the same small region. 49
4.6 Mean current density leakage values for different metal pads. Platinum is able to sustain up to 6V while titanium pads were already breaking at 3V. The asymmetry in all of the pads is evident. 49
4.7 Figures taken from [90]. 52
4.8 C-AFM measurements and topography (from [90]). 54
4.9 Graph of the capacitance and $1/C^2$ versus voltage as used in the model of a Schottky-semiconductor diode interface [95]. From [90]. 56
4.10 Qualitative band-structure scheme for the metal-semiconductor-metal stack (platinum-KNN-top metal) at zero bias. From [90]. 57
4.11 Schematic energy band for the Schottky and Poole-Frenkel conduction method (from [101]). 61
4.12 A fitting of $\ln(J/E)$ vs. $\sqrt{E}$ for fitting of Poole-Frenkel emission due to traps in KNN for forward bias (negative applied voltage). 62

5.1 XRD measured diffraction pattern of the KNN film. Peaks indicate the different orientations of the KNN film or the Platinum substrate. The graph is in a semilogarithmic scale. 67
5.2 Fitting of the XRD diffractograms of the classic PLD growth and RTA processed film. The peaks are fitted using a gaussian function through the software Fityk [116]. 68
5.3 SEM images of the two films. 69
5.4 KNN morphology comparison before and after RTA 70
5.5 Signal shape and setup configuration for the current leakage measurements 73
5.6 Top-bottom measurements (mean value) comparison between the classic PLD grown film (blue curve - here labeled as Nominal KNN) and tha RTA processed one (red curve). Both measurements are taken in the range $-3/+3\ V$ and in both case the top contact is made of Ni. The films have different thicknesses, the classic growth KNN is 300 nm, while the RTA one is 220 nm. 74
5.7 XRD diffractogram of a reduced group of sample. A further explanation for the legend is needed as we refer as "RTA thick" a sample with a higher deposition time (leading to a thicker film). Blue curve is the previously discussed RTA film 75
5.8 SEM images of the samples. Pre and post RTA images are presented, is it possible to notice that all the surfaces are pretty similar but most importantly is straightforward to notice that cracks are not a product of the annealing. 78
5.9 Cross section of a RTA film (with higher depositing time) annealed at 700°C; in particular is possible to see the detail of a crack and how this crack can actually lower the thickness of the whole film locally. 79
5.10 Stoichiometry ratios of KNN elements in function of temperature deposition and RTA temperature. 81
5.11 Density of current leakage in the different films annealed RTA processed at different temperature. Red curve is the reference RTA sample. Blue curves are subsequent RTA samples. 82
5.12 Density of current leakage in the different films annealed RTA processed at different temperature for a new batch of samples. Red curve is the reference RTA sample. Blue curves are subsequent RTA samples. 83

List of Tables

4.1 Stoichiometry ratios obtained analyzing the EDX diffractogram. 47
4.2 Electrode materials properties (from [83]). 50
4.3 Estimated dielectric constant using the Poole-Frenkel model and resistivities. For the latter values are extracted near the minimum of the leakage current; due to the huge rectification effect provided by Ni and Pt the estimation of ρ^+ would have lead to a non realistic estimate. (From [90]). 59

5.1 Stoichiometry ratios comparison between the previous works [21], [20] and RTA 71
5.2 Stoichiometric ratios comparison between pre and post RTA process 72
5.3 Stoichiometry ratios comparison between the previous works [21], [20], the RTA reference sample and the new films annealed at different temperature. 80